Messung der Lebensdauer vollständig rekonstruierter B Mesonen mit dem CDF Detektor

Zur Erlangung des akademischen Grades eines

DOKTORS DER NATURWISSENSCHAFTEN

von der Fakultät für Physik der Universität (TH) Karlsruhe

genehmigte

DISSERTATION

von

Dipl.-Phys. Andreas Heiss
aus Schaffhausen/Schweiz

Tag der mündlichen Prüfung : 6. Juli 2001

Referent: Herr Prof. Dr. Th. Müller
Korreferent: Herr Prof. Dr. M. Feindt

Abstract

This dissertation presents a measurement of the lifetime of fully reconstructed $B^{\pm}$ and B^0 mesons produced in $p\bar{p}$ collisions at a center-of-mass energy of 1.8 TeV. The data were collected with the Collider Detector at Fermilab (CDF) during Run I of the Tevatron Collider in the years 1992 – 1996. Measurements of the lifetimes of specific B hadron species provide a test of decay models beyond the simple spectator model which predict the $B^{\pm}$-lifetime to be longer as the B^0-lifetime by 5 – 10 %.
In this analysis, the B mesons are reconstructed in their charmonium decay modes with $J/\psi \to \mu^+ \mu^-$, $J/\psi \to e^+ e^-$, $\psi(2S) \to \mu^+ \mu^-$ and $\psi(2S) \to J/\psi \pi^+\pi^-$ final states. B meson candidates are selected by combining charmonium candidates with various reconstructed kaon species. The individual decay lengths of the B meson candidates are measured in two dimensions using a silicon vertex detector. To extract the $B^{\pm}$ and B^0 lifetimes from the data, simultaneous log-likelihood fits to the mass and decay length distributions of various reconstructed decay channels are performed. The lifetimes of charged and neutral B mesons are thereby measured to be

$$\tau(B^{\pm}) = 1.636 \pm 0.058\ (stat.) \pm 0.025\ (syst.)\ \text{ps}$$
$$\tau(B^0) = 1.497 \pm 0.073\ (stat.) \pm 0.032\ (syst.)\ \text{ps}.$$

Although the title of this dissertation refers to B mesons, a measurement of the lifetime of Λ_B baryons reconstructed in their decay mode $\Lambda_B \to J/\psi\ \Lambda$ is also presented. It is the first measurement of the Λ_B lifetime using this exclusive decay mode.
The CDF detector has been upgraded for Run II of the Tevatron collider in the last years. Due to the improved tracking system and the high integrated luminosity expected for the next two years, the statistical uncertainty of B lifetime measurements will be significantly lower. During the last four years, I spent a large amount of time on developing testing software for silicon sensor devices used for the new tracking system. This software is shortly described in the appendix.

Contents

1 Introduction **1**
1.1 The Standard Model of Particle Physics . . . 1
1.2 The History of the Quark Model . . . 3
1.3 The CKM Matrix . . . 5
1.4 Production and Fragmentation of b-Quarks in Hadronic Collisions . . 6
1.5 The lifetime of B-Mesons . . . 10

2 The Fermilab Accelerator and the CDF Experiment **13**
2.1 The Tevatron . . . 13
2.2 The CDF Experiment . . . 15
2.2.1 The Central Tracking Chamber (CTC) . . . 18
2.2.2 The Silicon Vertex Detector (SVX) . . . 18
2.2.3 Calorimeters . . . 21
2.2.4 Muon detectors . . . 23
2.2.5 The trigger system . . . 25

3 Data Samples **26**
3.1 The Dimuon Dataset . . . 26
3.2 The Inclusive Electron Dataset . . . 27
3.3 Data Storage . . . 28

4 Reconstruction of B Meson Decays and Lifetime Measurement **29**
4.1 Track Quality Cuts . . . 30
4.2 Reconstruction of J/ψ and $\psi(2S)$ Decays . . . 30
4.2.1 The $J/\psi \to \mu^+\mu^-$ and $\psi(2S) \to \mu^+\mu^-$ modes . . . 30
4.2.2 The Decay $J/\psi \to e^+e^-$ . . . 32
4.2.3 The Cascade Decay $\psi(2S) \to J/\psi\ \pi^+\pi^-$ . . . 35
4.3 Reconstruction of Kaon Decays . . . 35
4.3.1 $K^0_S\ (\overline{K^0_S})\ \to \pi^+\pi^-$ . . . 36
4.3.2 $K^*(892)^0\ (\overline{K^*(892)^0})\ \to K^\pm\pi^\mp$ . . . 36
4.4 B Candidate Selection . . . 37
4.5 Multiple B Meson Candidates . . . 39
4.6 Misinterpreted Λ_B Decays . . . 39
4.7 Lifetime Measurement . . . 41
4.7.1 The Primary Interaction Vertex . . . 41

4.7.2 The Proper Decay Length 43
4.7.3 Bremsstrahlung Corrections for $J/\psi \to e^+e^-$ 44

5 The Fitting Technique **46**
5.1 The Maximum Likelihood Method 46
5.2 The Mass Distributions of Signal and Background 47
5.3 The Signal $c\tau$ Distribution 48
5.4 The Background $c\tau$ Distribution 49
5.5 Fitting Procedure 50

6 Results **52**
6.1 Individual Decay Channels 52
6.1.1 Results for the Decay Channel $B^\pm \to J/\psi\ K^\pm$; $J/\psi \to \mu^+\mu^-$ 54
6.1.2 Results for the Decay Channel $B^\pm \to J/\psi\ K^\pm$; $J/\psi \to e^+e^-$ 55
6.1.3 Results for the Decay Channel $B^\pm \to \psi(2S)\ K^\pm$; $\psi(2S) \to \mu^+\mu^-$ 56
6.1.4 Results for the Decay Channel $B^\pm \to \psi(2S)\ K^\pm$; $\psi(2S) \to J/\psi\ \pi^+\pi^-$; $J/\psi \to \mu^+\mu^-$ 57
6.1.5 Results for the Decay Channel $B^\pm \to J/\psi\ K^{*\pm}$; $K^{*\pm} \to K^0_S\ \pi^\pm$; $J/\psi \to \mu^+\mu^-$ 58
6.1.6 Results for the Decay Channel $B^0 \to J/\psi\ K^0_S$; $K^0_S \to \pi^+\ \pi^-$; $J/\psi \to \mu^+\mu^-$ 59
6.1.7 Results for the Decay Channel $B^0 \to J/\psi\ K^{*0}$; $K^{*0} \to K^\pm\pi^\mp$; $J/\psi \to \mu^+\mu^-$ 60
6.2 Results of the Combined Fits 62
6.3 Consistency Checks 66
6.3.1 Size of the Mass Window 66
6.3.2 B^+ vs. B^- and B^0 vs. $\bar{B}^0$ lifetimes 67
6.3.3 Dependence on Momentum Cuts 67

7 Systematic Uncertainties **69**
7.1 Background parameterizations 69
7.2 Non-Gaussian tails of the resolution function 70
7.3 Fitting Procedure Bias 70
7.4 Bias due to the beam pointing constraint in the decay channel $B^0 \to J/\psi K^0_S$ 71
7.5 Residual misalignment of the SVX 72
7.6 Trigger Bias 72
7.7 Total Systematic Uncertainty 72

8 Measurement of the Λ_B Lifetime **73**

9 Conclusion and Final Results **75**

10 Future Prospects **78**

A Location of Datasets **82**

B Monte Carlo Programs **83**

C A Hybrid and Ladder test system for SVXII and ISL **84**

Bibliography **91**

List of Figures

1 Spektator-Modell Feynman-Diagramme. II
2 Eines der zwei Barrels des SVX-Detektors. III
3 Die $B^{\pm}$ Massenverteiung. VI
4 Die B^0 Massenverteilung. VI
5 Für die individuellen Zerfallskanäle gemessene Lebensdauern mit den statistische Unsicherheiten. IX
6 Zerfallslängenverteilung aller $B^{\pm}$-Datensätze. X
7 Zerfallslängenverteilung aller B^0-Datensätze. X

1.1 Examples of quark- and hadron-multiplets in the SU(3) quark model. 4
1.2 Lowest order ($\mathcal{O}(\alpha_s^2)$) Feynman diagrams for $b\bar{b}$ production through quark–antiquark annihilation and gluon–gluon fusion. 7
1.3 Examples of Feynman diagrams for $b\bar{b}$ production at next-to-leading order ($\mathcal{O}(\alpha_s^3)$) 7
1.4 Compilation of the CDF b-quark integral cross-section measurements and comparison with next-to-leading order QCD predictions. 8
1.5 Schematic view of the String-Fragmentation. 9
1.6 Fragmentation functions for light and heavy quarks. 10
1.7 Spectator model Feynman diagrams of B meson decays. 11
1.8 W exchange and weak annihilation diagrams. 12
1.9 Illustration of internal and external W emission for the decay $B^+ \rightarrow \bar{D}^0\,\pi^+$. 12

2.1 An overview over the Fermilab accelerator complex during Run I. . . 14
2.2 Time profile of the luminosity delivered by the Tevatron Collider and accumulated by the CDF experiment throughout Run I. 16
2.3 Isometric view of the CDF detector during Run I. 16
2.4 One quadrant of the CDF detector during Run I. 17
2.5 A CTC endplate, showing the wire feed-through slots for the cells in the nine superlayers. 19
2.6 One of the two SVX barrels. 20
2.7 A SVX layer 2 ladder with 4 SVX readout chips. 20
2.8 A wedge of the central calorimeter showing the ten towers in η. . . . 22
2.9 The $\eta - \phi$ coverage of the CDF central muon systems. 24

4.1 The J/ψ mass distribution. 31

4.2 The $\psi(2S) \to \mu^+\mu^-$ mass distribution. 32
4.3 The dielectron mass spectrum after a vertex constrained fit and electron P_T distributions. 33
4.4 The ELES efficiency as a function of the electron P_T. 34
4.5 The shape of the background in the dielectron mass spectrum 4.3 (a) caused by $B^+ \to \bar{D}^0 e^+ \nu_e$, $\bar{D}^0 \to K^+ e^- \bar{\nu}_e$ decays (Monte Carlo generated). 34
4.6 The $\psi(2S) \to J/\psi\ \pi^+\pi^-$ mass distribution. 35
4.7 The K^0_S mass distribution. 36
4.8 The first basic B decay topology relevant to this measurement. 38
4.9 The second basic B decay topology relevant to this measurement. . . 38
4.10 The $B^\pm$ mass distribution. 40
4.11 The B^0 mass distribution. 40
4.12 The invariant mass spectrum of MC generated $\Lambda_B \to J/\psi\ \Lambda$ decays reconstructed as $B^0 \to J/\psi K^0_S$. 41
4.13 The Tevatron beamspot measured with the SVX detector. 42
4.14 The distribution of primary vertices in the z direction for a typical store (collider fill). 43
4.15 Measured path and momentum of a B meson projected onto the plane transverse to the beam. 44
4.16 The relative correction factor of the B meson transverse momentum as a function of the dielectron invariant mass. 45

5.1 The mass distribution of $B^\pm \to J/\psi\ K^\pm$ events. 50

6.1 Mass distribution, background $c\tau$ and $c\tau$ distributions of reconstructed $B^\pm \to J/\psi\ K^\pm$; $J/\psi \to \mu^+\mu^-$ decays. 54
6.2 Mass distribution, background $c\tau$ and $c\tau$ distributions of reconstructed $B^\pm \to J/\psi\ K^\pm$; $J/\psi \to e^+e^-$ decays. 55
6.3 Mass distribution, background $c\tau$ and $c\tau$ distributions of reconstructed $B^\pm \to \psi(2S)\ K^\pm$; $\psi(2S) \to \mu^+\mu^-$ decays. 56
6.4 Mass distribution, background $c\tau$ and $c\tau$ distributions of reconstructed $B^\pm \to \psi(2S)\ K^\pm$; $\psi(2S) \to J/\psi\ \pi^+\pi^-$ decays. 57
6.5 Mass distribution, background $c\tau$ and $c\tau$ distributions of reconstructed $B^\pm \to J/\psi\ K^{*\pm}$; $K^{*\pm} \to K^0_S\ \pi^\pm$; $J/\psi \to \mu^+\mu^-$ decays. . . 58
6.6 Mass distribution, background $c\tau$ and $c\tau$ distributions of reconstructed $B^0 \to J/\psi\ K^0_S$; $K^0_S \to \pi^+\pi^-$; $J/\psi \to \mu^+\mu^-$ decays. 59
6.7 Mass distribution, background $c\tau$ and $c\tau$ distributions of reconstructed $B^0 \to J/\psi\ K^{*0}$; $K^{*0} \to K^\pm\pi^\mp$; $J/\psi \to \mu^+\mu^-$ decays. . . 60
6.8 The measured lifetimes and corresponding statistical uncertainties for the individual 5 $B^\pm$ and 2 B^0 decay channels. 61
6.9 $c\tau$ distribution of all $B^\pm$ decay channels combined with the fitted function superimposed. The hatched area is the signal contribution. . 62

6.10 $c\tau$ distribution of all B^0 decay channels combined with the fitted function superimposed. The hatched area is the signal contribution. . 63
6.11 The log-likelihood value as a function of the decay length $c\tau$ for the $B^\pm$ combined fit. 64
6.12 The log-likelihood value as a function of the decay length $c\tau$ for the B^0 combined fit. 64
6.13 A 1 σ contour plot of the fitted decay length $c\tau$ versus the fitted mass M (m_B) for the $B^\pm$ combined fit. 65
6.14 A 1 σ contour plot of the fitted decay length $c\tau$ versus the fitted mass M (m_B) for the B^0 combined fit. 65
6.15 The dependence of the best fit decay length on P_T thresholds. Decay channel $B^\pm \rightarrow J/\psi\ K^\pm;\ \ J/\psi \rightarrow \mu^+\mu^-$. 68
6.16 The dependence of the best fit decay length on P_T. Decay channel $B^\pm \rightarrow \psi(2S)\ K^\pm;\ \ \psi(2S) \rightarrow \mu^+\mu^-$. 68
6.17 The dependence of the best fit decay length on P_T thresholds. Decay channel $B^0 \rightarrow J/\psi\ K^{*0};\ \ K^{*0} \rightarrow K^\pm\pi^\mp;\ \ J/\psi \rightarrow \mu^+\mu^-$. 68

7.1 Background subtracted $c\tau$ distribution of $B^\pm$ candidates with the fitted signal contribution superimposed. 71
7.2 Background subtracted $c\tau$ distribution of B^0 candidates with the fitted signal contribution superimposed. 71

8.1 Mass distribution, background $c\tau$ and $c\tau$ distributions of reconstructed $\Lambda_B \rightarrow J/\psi\ \Lambda$ decays. 74

9.1 Comparison of the measured $B^\pm$ lifetime with other measurements and the world average value. 76
9.2 Comparison of the measured B^0 lifetime with other measurements and the world average value. 76
9.3 Comparison of the measured lifetime ratio with other measurements and the world average value. 77

10.1 Elevation view of one half of the CDF II detector. 79
10.2 SVXII and ISL. 80

C.1 An overview over the electrical components of the SVXII/ISL burnin test system. 85
C.2 The XTL main window. 86
C.3 The XTL chip parameter editor. 87
C.4 The control window for automatic gain scans. 88
C.5 Gain scan results for one whole chip. 89
C.6 The control window for signal to noise measurements. 90
C.7 S/N averaged over all channels of one particular SVX3 chip as a function of the preamplifier bandwidth. 90

List of Tables

1 Ergebnisse der kombinierten Fits aller Datensätze mit statistischen Unsicherheiten. IX

1.1 The three fermion generations of the Standard Model. 1
1.2 The four known fundamental interactions. 2
1.3 Different accelerators producing b quarks compared with respect to energy, $b\bar{b}$ cross sections, the produced hadrons and kinematics. . . . 6

2.1 Properties of the various calorimeters. 23

6.1 Fit results of the decay channel $B^{\pm} \to J/\psi\ K^{\pm}$ 54
6.2 Fit results of the decay channel $B^{\pm} \to J/\psi\ K^{\pm}$; $J/\psi \to e^+e^-$. 55
6.3 Fit results of the decay channel $B^{\pm} \to \psi(2S)\ K^{\pm}$; $\psi(2S) \to \mu^+\mu^-$. . . 56
6.4 Fit results of the decay channel $B^{\pm} \to \psi(2S)\ K^{\pm}$; $\psi(2S) \to J/\psi\ \pi^+\pi^-$. 57
6.5 Fit results of the decay channel $B^{\pm} \to J/\psi\ K^{*\pm}$. 58
6.6 Fit results of the decay channel $B^0 \to J/\psi\ K^0_S$. 59
6.7 Fit results of the decay channel $B^0 \to J/\psi\ K^{*0}$. 60
6.8 Best fit values and corresponding uncertainties of the common parameters in the fit to the combined $B^{\pm}$ decay channels. 62
6.9 Best fit values and corresponding uncertainties of the common parameters in the fit to the combined B^0 decay channels. 63
6.10 Fitted decay length and number of signal candidates for different mass windows. Decay channel $B^{\pm} \to J/\psi\ K^{\pm}$; $J/\psi \to \mu^+\mu^-$. 66
6.11 Fitted decay length and number of signal candidates for different mass windows. Decay channel $B^{\pm} \to \psi(2S)\ K^{\pm}$; $\psi(2S) \to \mu^+\mu^-$. 66
6.12 Fitted decay length and number of signal candidates for different mass windows. Decay channel $B^0 \to J/\psi\ K^{*0}$; $K^{*0} \to K^{\pm}\pi^{\mp}$; $J/\psi \to \mu^+\mu^-$. 67
6.13 B versus $\bar{B}$ comparison of best fit decay lengths and number of signal candidates. The errors are statistical. 67

7.1 Results of the combined lifetime fits without and with a second Gaussian function describing tails of the resolution function. 70
7.2 Summary of the systematic uncertainties. 72

8.1 Fit results of the decay channel $\Lambda_B \to J/\psi\ \Lambda$; $J/\psi \to \mu^+\mu^-$, $\Lambda \to p\ \pi^-$ 74

Zusammenfassung

Diese Dissertation präsentiert eine Messung der Lebensdauer vollständig rekonstruierter B-Mesonen mit dem CDF-Detektor[1]. Die Daten wurden während des Run I des Tevatron-Colliders in den Jahren 1992 bis 1996 aufgenommen. Die integrierte Luminosität des Datensatzes beträgt ≈ 113.8 pb^{-1}.
B-Mesonen sind farbneutrale, gebundene Zustände aus einen Quark und einem Antiquark. Eines dieser Quarks ist dabei ein *Bottom*-Quark (b) bzw. -Antiquark ($\bar{b}$). b-Quarks[2] gehören zur dritten Generation der Fermionen im Standardmodell der Teilchenphysik und wurden 1977 am Fermilab[3] als sogenannte Υ-Resonanz im Di-Myon-Massenspektrum entdeckt. Sie werden am $p\bar{p}$-Collider Tevatron mit einem im Vergleich zu e^+e^--Collidern sehr hohen Wirkungsquerschnitt von $\sigma_{b\bar{b}} \approx 50$ μb erzeugt. Das Verhältnis zum totalen Wirkungsquerschnitt ist mit $\sigma_{b\bar{b}}/\sigma_{tot} \approx 8 \cdot 10^{-4}$ jedoch klein. Es ist daher eine große Herausforderung, Ereignisse zu selektieren, die ein b-Quark enthalten. Dazu werden z.B. Ereignisse mit Di-Myon-Paaren mit einer invarianten Masse im Bereich der J/ψ Masse oder einzelne Leptonen mit relativ hohem Transversalimpuls extrahiert. Die b-Quarks werden in hadronischen Kollisionen paarweise erzeugt. Dabei tragen hauptsächlich die Gluon-Fusions- ($gg \to b\bar{b}$) und Quark-Antiquark-Annihilations-Prozesse ($q\bar{q} \to b\bar{b}$) aber auch Prozesse höherer Ordnung wie z.B. Gluon-Splitting bei. Die b-Quarks fragmentieren, d.h. es bilden sich Hadronen, gebundene Zustände aus zwei oder drei Quarks. Dieser Prozess wird durch phänomenologische Modelle beschrieben, z.B. dem String-Fragmentations-Modell. Man stellt sich vor, daß sich zwischen den auseinanderlaufenden Quarks ein 'Feldschlauch' (String) aus Gluonen bildet, aus dem neue Quark-Antiquark-Paare hervorgehen, sobald die Energie im String dazu ausreicht. b-Quarks fragmentieren 'hart', d.h. die entstehenden b-Hadronen erhalten im Mittel einen Großteil des Impulses des Quarks.
Eine Messung der Lebensdauer von b-Hadronen ermöglicht die Bestimmung von Standard-Modell-Parametern, wie z.B. V_{cb}, einem Element der Cabibbo-Kobayashi-Maskawa-Matrix, welche die Mischung zwischen Quarks der einzelnen Generationen beschreibt. Erste Messungen der b-Hadron-Lebensdauer der MARK II und MAC Kollaborationen im Jahr 1983 ergaben eine unerwartet lange Lebensdauer von et-

[1] Collider Detector at Fermilab
[2] Im Folgenden wird der Begriff 'Quark' sowohl für Quarks als auch für Antiquarks verwendet.
[3] Fermi National Accelerator Laboratory, Batavia, Illinois, U.S.A.

wa 1.2 ps und damit den ersten Hinweis darauf, dass die Mischung zwischen den Quarks der 3. Generation und denen der 2. Generation viel schwächer ist als die Mischung zwischen den Quarks der 2. und der 1. Generation. Die Lebensdauer von b-Hadronen kann innerhalb des sogenannten Spektator-Modells berechnet werden. In diesem stark vereinfachten Modell betrachtet man den Zerfall des b-Quarks unabhängig von den anderen Quarks bzw. dem anderen Quark ("Spektator") im Hadron. Daher ist in diesem Ansatz die Lebensdauer der verschiedenen b-Hadronen gleich.

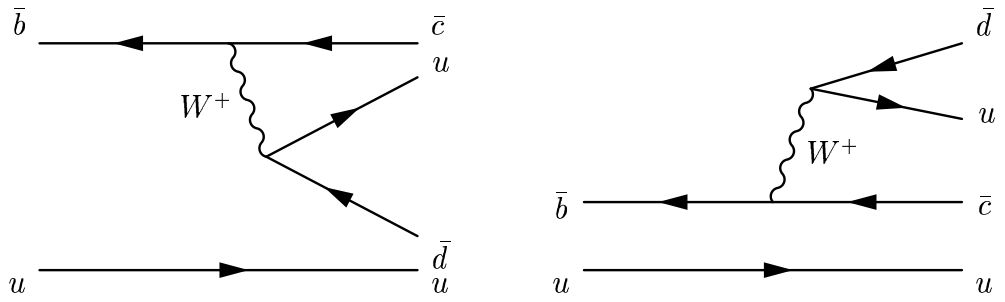

Abbildung 1: Spektator-Modell Feynman-Diagramme. Die Diagramme zeigen interne (links) und externe (rechts) W-Abstrahlung.

Ein realistischeres Modell erhält man, wenn man auch andere Prozesse wie z.B. die Annihilation zweier Quarks oder den direkten Austausch eines W-Bosons zwischen zwei Quarks im Hadron berücksichtigt. Solche Prozesse sowie Interferenzen zwischen Feynman-Diagrammen mit gleichen Anfangs- und Endzuständen (z.B. der in Abbildung 1 gezeigten Diagramme), sogenannte Pauli-Interferenzen, führen zu unterschiedlichen Lebensdauern der verschiedenen b-Hadronen. QCD-Korrekturen liefern einen weiteren Beitrag. Aufgrund dieser Effekte erwartet man folgende Lebensdauer-Hierarchie:

$$\tau_{\Lambda_b} \; < \; \tau_{B^0} \; < \; \tau_{B^\pm} \tag{1}$$

Die Messungen der Lebensdauern der verschiedenen b-Hadronen, $B^\pm$ und B^0 Mesonen sowie Λ_b Baryonen, ermöglichen somit einen Test von Zerfalls-Mechanismen außerhalb des Spektator-Modells.

Das Tevatron ist der zur Zeit höchstenergetischte Proton-Antiproton-Beschleuniger. Bis zur (vorübergehenden) Abschaltung im Jahr 1996 betrug die Schwerpunktsenergie 1.8 TeV. Protonen und Antiprotonen werden durch einen mehrstufigen Beschleuniger-Komplex beschleunigt und danach zur Kollision gebracht. H^- Ionen werden mit Hilfe eines Linearbeschleunigers auf eine Energie von 400 MeV gebracht bevor die Elektronen durch 'Stripping' in einer Kohlenstoff-Folie entfernt werden. Die übrig bleibenden Protonen werden in einem Synchrotron, dem 'Booster', bis zu einer Energie von 8 GeV weiter beschleunigt. Im 'Main Ring', dem ehemaligen Hauptbeschleuinger am Fermilab, werden die Protonen auf eine Energie von 120 GeV gebracht und danach in den Tevatron-Beschleuniger geleitet. Ein kleiner Teil der 120 GeV Protonen wird jedoch auf ein Target geleitet um Antiprotonen zu

erzeugen, die nach einer Zwischenspeicherung in entgegengesetzter Richtung in das Tevatron eingespeist werden. Protonen und Antiprotonen werden dann gleichzeitig auf 900 GeV beschleunigt. Jeweils sechs Pakete (Bunches) aus Protonen bzw. Antiprotonen laufen nun in entgegengesetzter Richtung im Tevatron um und werden an zwei definierten Wechselwirkungszonen zur Kollision gebracht. An den beiden Wechselwirkungszonen befinden sich die Teilchendetektoren CDF und D0[4], welche die entstehenden Teilchen nachweisen. CDF ist ein zylindersymmetrisch aufgebauter Universaldetektor, 27 m lang und 10 m hoch, mit dem Impuls, Energie und die Art von Teilchen bestimmt werden können. Die innerste Lage bilden ein Silizium-Vertex-Detektor (SVX) und eine Driftkammer (CTC) die sich innerhalb eines 1.4 T starken, solenoiden Magnetfeldes befinden. Das Magnetfeld wird durch eine supraleitende Magnetspule erzeugt, die sich außerhalb der CTC befindet. Die CTC misst Teilchen-Spuren im Radius-Bereich von etwa 30 cm bis 140 cm um den Wechselwirkungspunkt und liefert sowohl $r-\phi$- als auch z-Informationen. Das für diese Analyse wichtigste Instrument ist der SVX Detektor. Er besteht aus zwei jeweils ca. 26 cm langen "Barrels", die jeweils aus vier Lagen einseitiger Silizium-Streifen-Detektoren bestehen, welche lediglich $r-\phi$-Koordinaten liefern. Ein solches Barrel ist in Abbildung 2.6 gezeigt. Die einzelnen Lagen befinden sich in radialen Abständen zwischen 3 cm und 7.85 cm zur Strahllinie. Der Abstand (Pitch) der analog ausgelesenen Steifen auf den Silizium-Detektoren beträgt zwischen 55 μm und 60 μm. Bei der

[4]D0 ist nach dem Gebäude benannt, in dem das Experiment untergebracht ist.

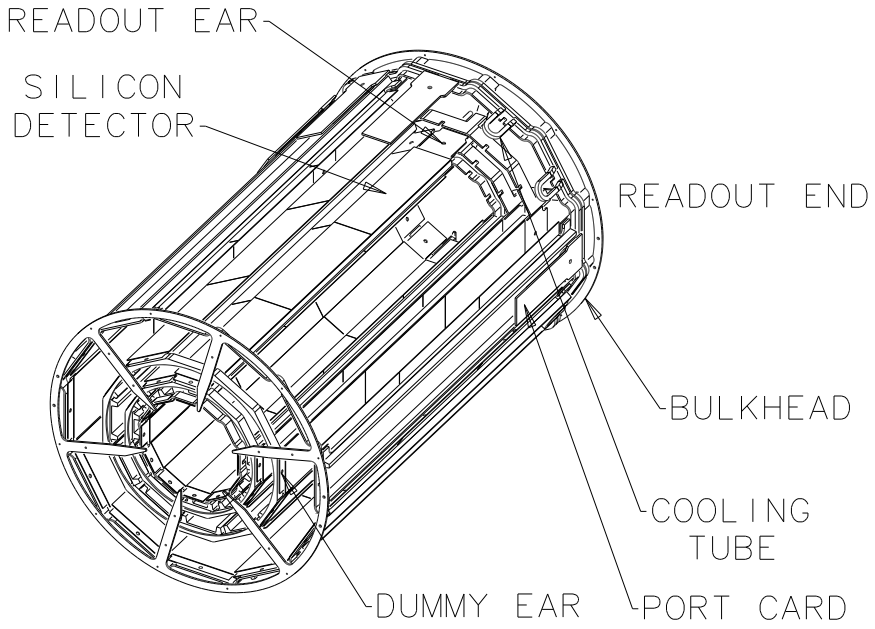

Abbildung 2: Eines der zwei Barrels des SVX-Detektors.

Spurrekonstruktion werden in der CTC gemessene Spuren nach innen extrapoliert und mit im SVX-Detektor gemessenen Koordinaten von Teilchendurchgängen in Verbindung gebracht. Dadurch wird die Genauigkeit der in der CTC rekonstruierten Teilchenspuren drastisch erhöht. Die von SVX und CTC zusammen erreichte Impaktparameterauflösung[5] beträgt $(13+40/P_T)$ μm. Die Transversalimpulsauflösung beträgt $\sigma_{P_T}/P_T \approx \sqrt{(0.9P_T)^2 + (6.6)^2} \cdot 10^{-3}$, wobei der Transversalimpuls P_T in beiden Fällen in GeV/c angegeben wird.
Außerhalb der Magnetspule befinden sich die zentralen elektromagnetischen (CEM) und hadronischen (CHA) Kalorimeter. Die Kalorimeter sind Sampling-Kalorimeter mit Blei bzw. Eisen als Absorbermaterial und Plastik-Szintillator als aktivem Medium[6]. Sechs elektromagnetische Strahlungslängen tief im Kalorimeter befinden sich Proportionalkammern (CES), mit denen die Position elektromagnetischer Schauer genau vermessen werden kann. Weitere Proportionalkammern (CPR) befinden sich vor dem Kalorimeter außerhalb der Magnetspule und helfen die im Kalorimeter gemessenen Teilchen-Schauer zu klassifizieren. Die Myonkammern bilden das äußerste Detektorsystem des CDF-Experiments. Sie weisen die Spuren aller geladenen Teilchen nach, welche die Kalorimeter und gegebenenfalls weitere Stahlabschirmungen noch durchdringen. Spurfragmente in den Myonkammern werden "Stubs" genannt.
CDF verwendet ein 3-stufiges Triggersystem um die interessanten Ereignisse aus den mit 300 kHz auftretenden Proton-Antiproton-Kollisionen herauszufiltern. In der ersten Triggerstufe wird nach Energiedepositionen im Kalorimeter und den Myonkammern gesucht. In der zweiten Stufe werden auf einfache Weise Spuren in der CTC rekonstruiert und in die Kalorimeter und Myonkammern extrapoliert während in der dritten Stufe das gesamte Ereignis unter Einbeziehung aller Detektorsysteme (außer dem SVX-Detektor) rekonstruiert wird.
Für diese Messung wurden verschiedene Datensätze analysiert: Die Di-Myon-Datensätze bestehen aus Ereignissen, die 2 Myonen mit einer invarianten Masse im Bereich der J/ψ- oder $\psi(2S)$-Masse enthalten. Die beiden Myonen haben dabei einen Transversalimpuls größer $\approx$ 2 GeV/c. Der inklusive Elektron-Datensatz enthält Ereignisse mit im Trigger identifizierten Elektron-Kandidaten deren Transversalimpuls typischerweise über 5 GeV/c ist. Einen Di-Elektron-Trigger gab es während des Tevatron Run I nicht.
Zur Rekonstruktion von B-Meson-Zerfällen wurden verschiedene Programm-Module entwickelt, welche in das offizielle CDF Offline-Softwarepaket "Analysis Control" eingebunden werden können. Die Rekonstruktion erfolgt in mehreren Schritten:

Suche nach $J/\psi \to \mu^+ \mu^-$ und $\psi(2S) \to \mu^+ \mu^-$ Zerfällen

Eine in den Spurdetektoren nachgewiesene Teilchen-Spur wird als Myon-Kandidat akzeptiert, wenn sie mit hinreichender Genauigkeit auf einen "Stub" im Myon-Detektor-System zeigt. Die Spur muss in der CTC und in mindestens 3 der 4 Lagen im SVX-Detektor nachgewiesen worden sein. Ein weiteres Kriterium ist eine der

[5] Der Impaktparameter einer Spur ist der Abstand der Spur zum Strahl am Ort der nächsten Annäherung.

[6] Im Vorwärtsbereich werden Ionisationskammern als aktives Medium verwendet.

Spur zugeordnete Energiedeposition im hadronischen Kalorimeter von mindestens 0.1 GeV. Aus jeweils zwei entgegengesetzt geladenen Myon-Kandidaten werden Paare gebildet und ein gemeinsamer Vertex wird durch Minimierung einer χ^2-Funktion bestimmt. Dabei werden die Spurparameter innerhalb ihrer Fehler so variiert, dass die beiden Spuren vom gleichen Vertex ausgehen (Vertex Constraint Fit). Vertices mit einer invarianten Masse von $\pm$ 80 MeV/c^2 um die J/ψ- oder $\psi(2S)$-Masse werden als Kandidaten akzeptiert. Es werden ca. 280000 J/ψ- und 7800 $\psi(2S)$-Kandidaten gefunden.

Suche nach $J/\psi \to e^+\ e^-$

Die CDF Elektron-Identifikations-Algorithmen sowie der Elektron-Trigger sind für Elektronen mit einem relativ hohen Transversalimpuls von ca. 10 GeV/c ausgelegt und daher ineffizient für niederenergetische Elektronen wie man sie aus B-Meson-Zerfällen erwartet. Trigger-Elektronen werden daher mit entgegengesetzt geladenen Spuren kombiniert, die andere Elektron-Identifikations-Kriterien erfüllen und einen Transversalimpuls von mindestens 1 GeV/c besitzen. Diese Kriterien umfassen Tests des spezifischen Energieverlustes in der CTC, der Energiedeposition im elektromagnetischen und hadronischen Kalorimeter sowie Vergleiche von CES Detektorsignalen mit Elektron-Teststrahl-Daten. Beide Elektron-Kandidaten, das Trigger-Elektron sowie die zweite Spur, müssen in mindestens 3 Lagen des SVX-Detektors nachgewiesen worden sein. Wie oben beschrieben, wird dann ein gemeinsamer Vertex bestimmt.

Suche nach $\psi(2S) \to J/\psi\ \pi^+\ \pi^-$

Wurde in einem Event ein $J/\psi \to \mu^+\ \mu^-$ Kandidat gefunden, wird nach entgegengesetzt geladenen Spurpaaren mit einer invarianten Masse < 610 MeV/c^2 gesucht, die mit den beiden Myonen einen gemeinsamen Vertex besitzen. Dabei wird den beiden Spuren des zusätzlichen Spurpaars jeweils die Pion-Masse zugeordnet. 4-Spur-Vertices mit einer invarianten Masse im Bereich $\pm$ 24 MeV/c^2 um die $\psi(2S)$-Masse sind $\psi(2S)$ Kandidaten. Etwa 3500 solcher Kandidaten werden gefunden.

Suche nach den Kaon-Zerfällen $K^{*0} \to K^\pm\ \pi^\mp$ und $K^0_S \to \pi^+\ \pi^-$

Zur Rekonstruktion von K^{*0}-Zerfällen werden Paare von entgegengesetzt geladenen Spuren gesucht, denen die $K^\pm$ bzw. $\pi^\pm$ Massen zugeordnet werden. Die invariante Masse der beiden Spuren muss nach einem Vertex-Constraint-Fit im Bereich $\pm$ 120 MeV/c^2 um die K^{*0}-Masse liegen.

$K^0_S \to \pi^+\ \pi^-$ Zerfälle werden in ähnlicher Weise rekonstruiert. Den beiden entgegengesetzt geladenen Spuren wird hier jedoch die $\pi^\pm$-Masse zugeordet. Nach dem Vertex-Fit muss die invariante Masse des Vertex im Bereich $\pm$ 25 MeV/c^2 um die K^0_S-Masse liegen. Die K^0_S-Kandidaten müssen ausserdem eine signifikante Entfernung in transversaler Richtung zum Strahl zurücklegen.

Selektion von B-Meson-Kandidaten

B-Meson-Kandidaten werden durch Kombination eines J/ψ- bzw. $\psi(2S)$-Kandidaten mit einem Kaon gebildet. In den Fällen $B^\pm \to \psi K^\pm$ ($\psi = J/\psi$ oder $\psi(2S)$) werden Spuren gesucht, die vom gleichen Vertex ausgehen wie die beiden Leptonen aus dem ψ-Zerfall. Im Fall $B^0 \to \psi K^{*0}$ wird geprüft, ob die beiden Spu-

ren aus dem K^{*0}-Zerfall vom gleichen Vertex stammen wie die Leptonen aus dem ψ-Zerfall. In den Fällen $B^0 \to \psi K_S^0$ und $B^\pm \to \psi K^{*\pm}$ wird verlangt, daß der Impulsvektor des K_S^0 auf den ψ-Vertex zurück zeigt. In allen Fällen wird der B-Vertex unter Einbeziehung aller Spuren bestimmt. Die invariante Masse der B-Vertices muss im Bereich $\pm$ 150 MeV/c^2 um den Weltmittelwert liegen.
Sollten im selben Ereignis mehrere gleichartige B-Meson-Kandidaten rekonstruiert worden sein, wird nur ein Kandidat für die weitere Analyse selektiert. Die Abbildungen 3 und 4 zeigen die Massenverteilungen der rekonstruierten $B^\pm$- und B^0-Kandidaten. Für das jeweils rechte Histogramm wurde ein Schnitt auf die Zerfallslänge gemacht, der den Untergrund stark reduziert und ca. 85% effizient ist.

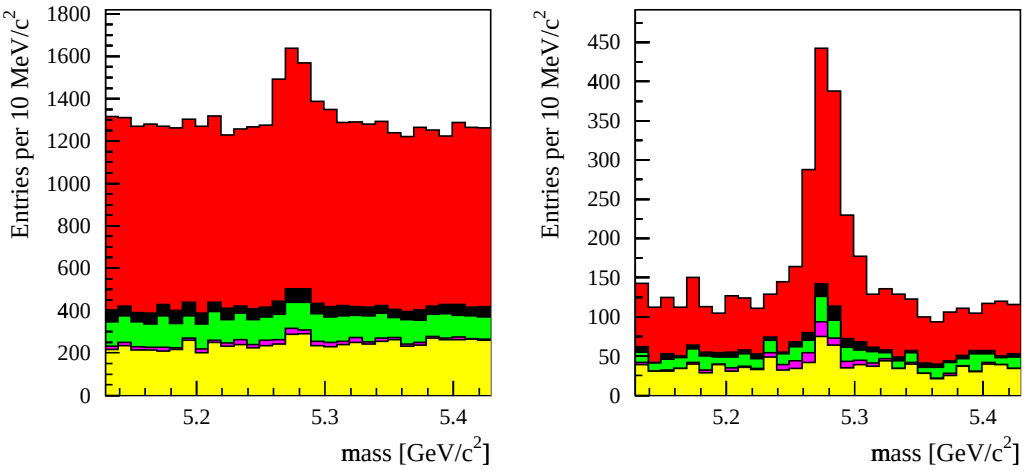

Abbildung 3: Die $B^\pm$ Massenverteilung ohne (links) und mit Schnitt $c\tau > 100\ \mu$m (rechts). Die Signale sind (von unten nach oben): $B^\pm \to J/\psi\ K^{*\pm},\ J/\psi \to \mu^+\mu^-$; $B^\pm \to J/\psi\ K^\pm,\ J/\psi \to e^+e^-$; $B^\pm \to \psi(2S)\ K^\pm, \psi(2S) \to \mu^+\mu^-$; $B^\pm \to \psi(2S)\ K^\pm, \psi(2S) \to J/\psi\ \pi^+\pi^-$; $B^\pm \to J/\psi\ K^\pm,\ J/\psi \to \mu^+\mu^-$.

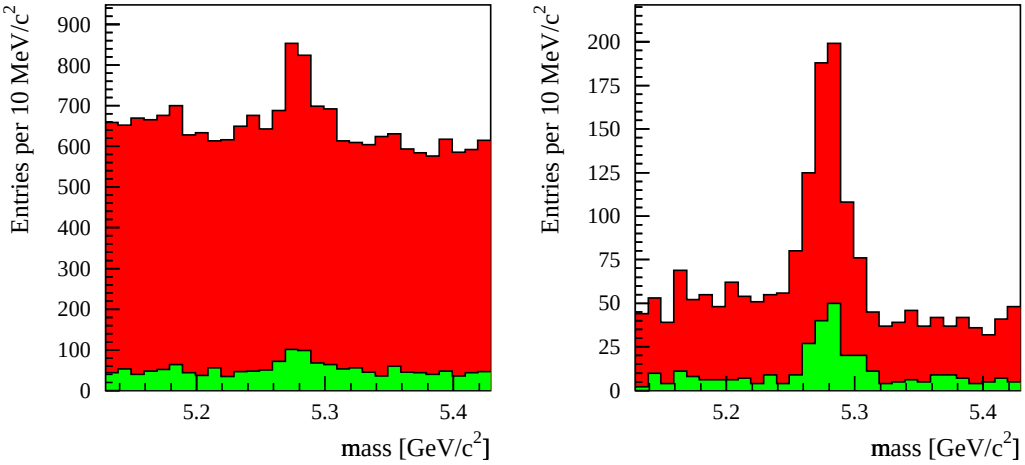

Abbildung 4: Die B^0 Massenverteilung ohne (links) und mit Schnitt $c\tau > 100\ \mu$m (rechts). Die Signale sind (von unten nach oben): $B^0 \to J/\psi\ K_S^0,\ J/\psi \to \mu^+\mu^-$; $B^0 \to J/\psi\ K^{*0},\ J/\psi \to \mu^+\mu^-$

Aufgrund der langen Lebensdauer des Λ-Baryons ist die Ereignistopologie des Zerfalls $\Lambda_B \to J/\psi\ \Lambda;\ \Lambda \to p\ \pi^-$ derer des Zerfalls $B^0 \to J/\psi\ K_S^0;\ K_S^0 \to \pi^+\ \pi^-$ sehr ähnlich. Λ_B-Zerfälle könnten deshalb durch Zuordnung der Pion-Massen zu den Spuren aus dem Λ-Zerfall fälschlicherweise als B^0-Zerfälle rekonstruiert werden. Eine Monte Carlo Studie ergab jedoch eine zu vernachlässigende "Verunreinigung" des $B^0 \to J/\psi\ K_S^0$ Datensatzes durch Λ_B-Zerfälle von 0.40 ± 0.25 %.

Die Bestimmung der individuellen Zerfallslänge der rekonstruieren B-Meson-Kandidaten erfolgt durch Messung des Abstandes zwischen dem Primärvertex und dem B-Zerfalls-Vertex in der Ebene senkrecht zur Strahlachse. Die Position des Primärvertex wird dabei durch die mittlere Strahlposition angenähert, die für jeden Store[7] neu bestimmt wird. Der Tevatron-Strahl hat ein rundes Profil das durch eine Gaußverteilung mit $\sigma \approx 23\ \mu$m beschreiben werden kann. Die Strahlposition ist während eines Collider-Stores äußerst stabil, jedoch ist der Strahl nicht notwendigerweise parallel zur z-Achse des Detektors. Die Neigung und ein möglicher Versatz des Strahls wird bei der Berechnung der mittleren Strahlposition am Ort des B-Zerfalls berücksichtigt. Die transversale Zerfallslänge L_{xy} ergibt sich als Projektion des Verbindungsvektors $\vec{X}$ zwischen Primärvertex und B-Zerfalls-Vertex auf den Transversalimpuls-Vektor des B-Mesons:

$$L_{xy} = \frac{\vec{X} \cdot \vec{P_T^B}}{|\vec{P_T^B}|} \tag{2}$$

Die Zerfallslänge im Ruhesystem des B-Mesons ergibt sich zu

$$c\tau = L_{xy} \cdot \frac{1}{(\beta\gamma)_T^B} = L_{xy} \cdot \frac{m_B}{P_T^B} \tag{3}$$

Im Fall des Zerfalls $J/\psi \to e^+\ e^-$ sind Bremsstrahlungsverluste des Elektrons und des Positrons aufgrund ihrer geringen Masse nicht zu vernachlässigen. Der Transversalimpuls des B-Mesons wird daher in Abhängigkeit der gemessenen invarianten Masse des Elektron-Positron-Paares korrigiert. Diese Korrektur wurde mit Hilfe von Monte Carlo Simulationen bestimmt und ist für die zur B-Meson-Rekonstruktion verwendeten J/ψ-Kandidaten kleiner als 4 %.

Die Bestimmung der mittleren Lebensdauer der $B^\pm$- und B^0-Mesonen erfolgt mit der Maximum-Likelihood-Methode zuerst separat für jeden Zerfallskanal (Datensatz) und danach unter Einbezieheung aller Kanäle. Dabei wird jeweils eine Log-Likelihood-Funktion der Form

$$\mathcal{L} = -2 \sum_{i=1}^{N} log\ f(\vec{x_i}, \vec{p}) \tag{4}$$

[7] Eine ununterbrochener Zeitraum, in dem die selben Proton- und Antiproton-Bunches im Collider umlaufen.

minimiert. N ist hierbei die Anzahl der B-Meson-Kandidaten im jeweiligen Datensatz. f ist eine Wahrscheinlichkeitsdichtefunktion, die von gemessenen Größen $\vec{x_i}$ und zu variierenden Parametern $\vec{p}$ abhängt. Die $\vec{x_i}$ sind in diesem Fall die Zerfallslänge $\lambda^{(i)} = c\tau^{(i)}$, der Fehler der Zerfallslänge $\sigma_\lambda^{(i)}$, die invariante Masse $m^{(i)}$ und deren Fehler $\sigma_m^{(i)}$ der einzelnen B-Meson-Kandidaten. Freie Parameter sind neben der mittleren Zerfallsänge $c\tau$ Parameter zur Beschreibung der Massen- und Zerfallslängen-Verteilungen des Untergrundes, Parameter der Massenverteilung des Signals und Fehler-Skalierungsfaktoren[8]. f hat die Form

$$f \;=\; (1 - f_B) \cdot F_{sig} \cdot H_{sig} + f_B \cdot F_{bgr} \cdot H_{bgr} \tag{5}$$

wobei f_B der Untergrundanteil ist. F_{sig} und H_{sig} bzw. F_{bgr} und H_{bgr} sind die Parameterisierungen der Zerfallslängen- und Massenverteilungen von Signal und Untergrund. Die Massenverteilung des Signals wird durch eine Gauß-Funktion beschrieben, die des Untergrundes durch eine Gerade. Um dem Umstand Rechnung zu tragen, dass jede Messung der individuellen Zerfallslänge mit einem Fehler behaftet ist, wird die Zerfallslängenverteilung des Signals durch eine Faltung einer Exponentialfunktion mit einer Gauß-Funktion beschrieben. Die Zerfallslängenverteilung des Untergrundes wird durch eine Summe aus drei Exponentialfunktionen und einer Gauß-Funktion parameterisiert. Zwei der Exponentialfunktionen beschreiben die Verteilung für positive Zerfallslängen, eine Exponentialfunktion die Verteilung für Zerfallslängen < 0. Die Gauß-Funktion beschreibt die Verteilung des Untergrundes durch 'prompte' J/ψ bzw. $\psi(2S)$, welche direkt in den $p\bar{p}$-Kollisionen entstehen. Ein C++ Programm berechnet die Wahrscheinlichkeitsdichte f und minimiert die Log-Likelihoodfunktion $\mathcal{L}$. Dieser Vorgang wird im Fortlaufenden als 'Fit' bezeichnet, da hierbei die Wahrscheinlichkeitsdichtefunktion an die Daten 'angepasst' wird. Die Fit-Prozedur läuft zunächst für jeden einzelnen Datensatz in mehreren Schritten ab: Zuerst wird lediglich ein Fit an die Massenverteilung durchgeführt. Dabei wird der Untergrund in den Daten durch einen Schnitt auf die Zerfallslänge reduziert. Im zweiten Schritt wird der Fit an die Zerfallslängenverteilung des Untergrundes in den Seitenbändern der Massenverteilung durchgeführt. Diese beiden Schritte dienen lediglich dazu, Startwerte für den simultanen Fit an Masse- und Zerfallslängenverteilungen zu gewinnen, bei dem alle Parameter wieder frei variiert werden. Ein stabiler Fit konnte für 2 B^0- und 7 $B^\pm$-Datensätze (Zerfallskanäle) erreicht werden. Die Ergebnisse sind in Abblidung 5 zusammengefasst.
Zur Bestimmung der mittleren $B^\pm$- und B^0-Lebensdauern werden jeweils alle Datensätze gleichzeitig in den Fit einbezogen. Um die unterschiedlichen Formen der Zerfallslängen- und Massenverteilungen des Untergrundes in den verschiedenen Datensätzen zu berücksichtigen, werden für jeden Datensatz individuelle Parameter verwendet. Gemeinsame Parameter sind die zu bestimmende mittlere Zerfallslänge $c\tau$, die Masse M und die zugehörigen Fehler-Skalierungsfaktoren. Die Werte dieser Parameter nach den Fits sind in Tabelle 1 aufgelistet. Die Abbildungen 6 und 7 zei-

[8]Diese Parameter sind eingeführt worden, um einer möglichen Unter- oder Überschätzung der Fehler der gemessenen Zerfallslängen und Massen Rechnung zu tragen.

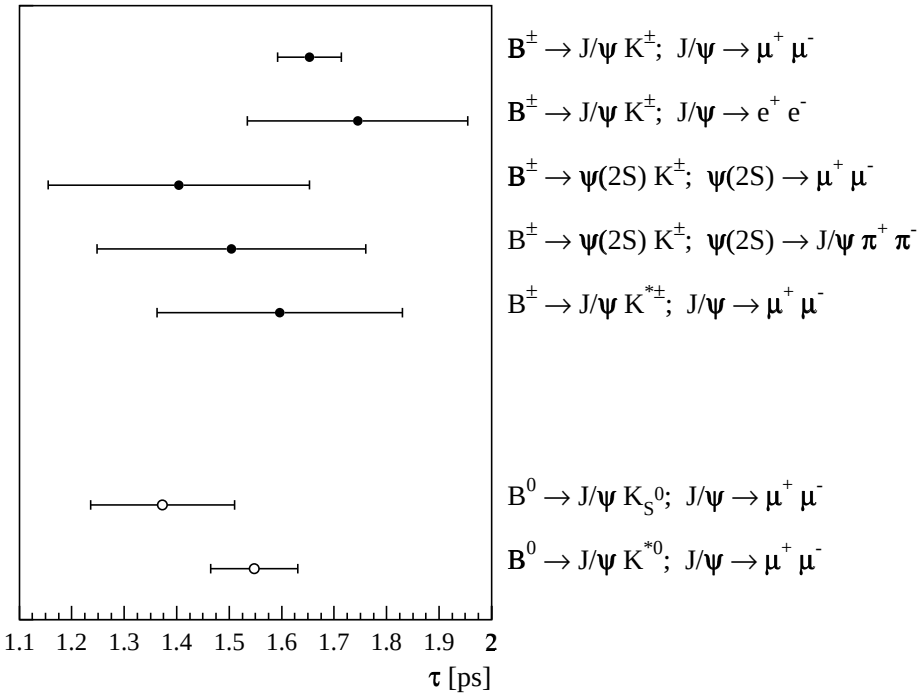

Abbildung 5: Für die individuellen Zerfallskanäle gemessene Lebensdauern mit den statistische Unsicherheiten.

Parameter	$B^{\pm}$	B^0
Mittlere Zerfallslänge $c\tau$ [μm]	490.41 ± 17.53	448.80 ± 21.84
Fehler-Skalierungsfaktor s_λ	1.1702 ± 0.0058	1.1526 ± 0.0086
Mittlere Masse M	5.2770 ± 0.0005	5.2778 ± 0.0006
Fehler-Skalierungsfaktor s_m	1.1875 ± 0.0408	1.3316 ± 0.0688
Mittlere Lebensdauer τ [ps]	**1.636 ± 0.058**	**1.497 ± 0.073**
N_{Signal}	1182 ± 43	565 ± 29

Tabelle 1: Ergebnisse der kombinierten Fits aller Datensätze mit statistischen Unsicherheiten.

gen die Zerfallslängenverteilungen der kombinierten $B^{\pm}$- bzw. B^0-Datensätze und die angepassten Funktionen.
Verschiedene Quellen systematischer Unsicherheiten werden in Betracht gezogen:

- Eine Unsicherheit der Positionen der einzelnen Lagen des SVX-Detektors.
- Nicht-Gauß'sche Anteile der Auflösungsfunktion der gemessenen Zerfallslängen.
- Eine mögliche schlechte Parametrisierung der Zerfallslängen-Verteilung des Untergrundes.
- Systematische Fehler durch die Fit-Prozedur selbst.

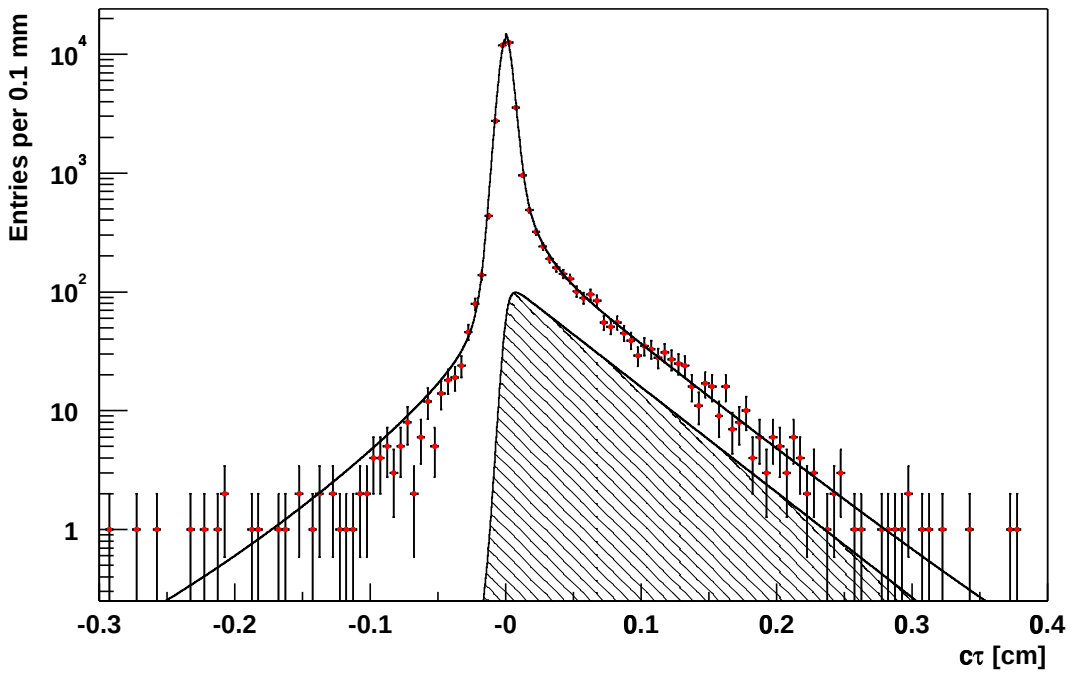

Abbildung 6: Zerfallslängenverteilung aller $B^{\pm}$-Datensätze mit der angepassten Funktion. Der schraffierte Bereich ist der Signalanteil.

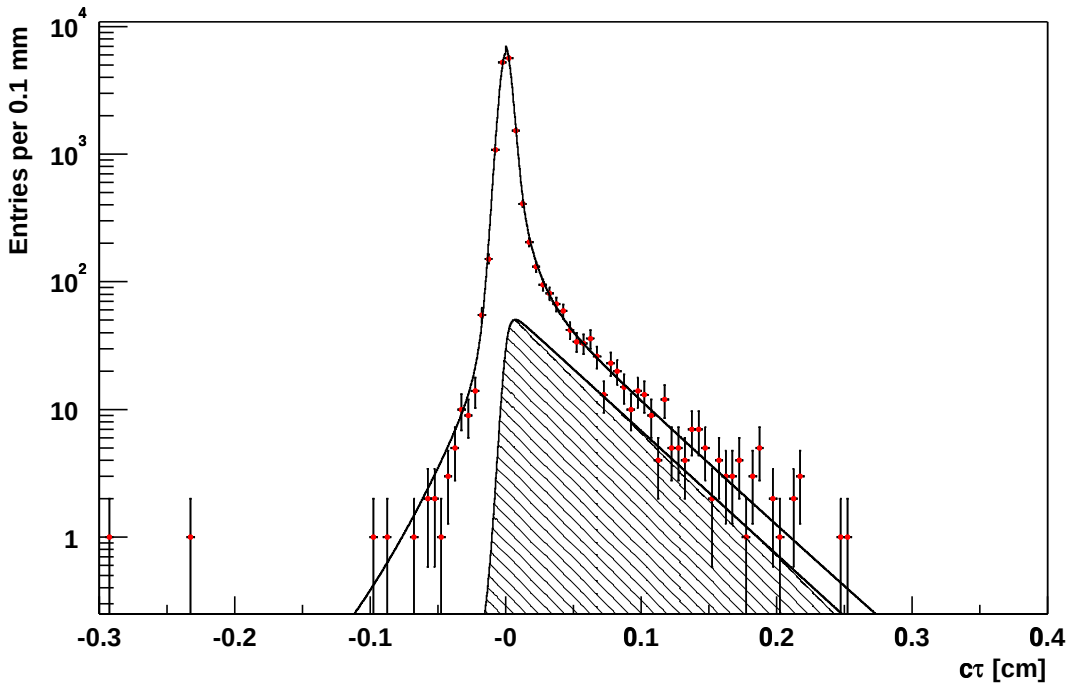

Abbildung 7: Zerfallslängenverteilung aller B^0-Datensätze mit der angepassten Funktion. Der schraffierte Bereich ist der Signalanteil.

Die gesamten systematischen Unsicherheiten der mittleren Zerfallslängen ergeben ± 7.4 μm für $B^{\pm}$-Mesonen und ± 9.6 μm für B^0-Mesonen.

Die Gesamtergebnisse dieser Messung sind damit:

$$\tau(B^{\pm}) = 1.636 \ \pm \ 0.058 \ (stat.) \ \pm \ 0.025 \ (syst.) \text{ ps}$$
$$\tau(B^0) \ = 1.497 \ \pm \ 0.073 \ (stat.) \ \pm \ 0.032 \ (syst.) \text{ ps}$$

Für das Verhältnis der $B^{\pm}$- und B^0-Lebensdauern ergibt sich:

$$\frac{\tau(B^{\pm})}{\tau(B^0)} \ = 1.093 \ \pm \ 0.066 \ (stat.) \ \pm \ 0.029 \ (syst.) \text{ ps}$$

Der systematische Fehler des Verhältnisses enthält hierbei alle Anteile der systematischen Unsicherheiten der $B^{\pm}$- und B^0-Ergebnisse und ist daher eine konservative Abschätzung.

Die B-Meson-Rekonstruktionssoftware kann auch verwendet werden, um Λ_B-Baryon-Zerfälle in J/ψ Λ zu rekonstruieren. Durch die lange Lebensdauer des Λ ist die Ereignistopologie hier ähnlich wie im Fall $B^0 \to J/\psi \ K^0_S$. Zur Bestimmung der mittleren Λ_B-Lebensdauer wird die gleiche Fit-Prozedur verwendet wie für die einzelnen B-Meson-Kanäle. Mit einem Signal von 38 ± 11 Λ_B ergibt sich als mittlere Lebensdauer

$$\tau_{\Lambda_B} \ = \ 1.22 \ \pm \ 0.36 \ (stat.) \text{ ps.}$$

Dies ist die erste Messung der Λ_B-Lebensdauer in diesem Zerfallskanal an einem Hadron-Kollider.
Die theoretische Vorhersage $\tau_{B^{\pm}} > \tau_{B^0} > \tau_{\Lambda_B}$ wird durch diese Analyse bestätigt. Der Gesamtfehler der Messungen wird durch die statistischen Unsicherheiten dominiert, jedoch wird diese exklusive Methode eine sehr präzise Messung der B-Meson Lebensdauern mit den zu erwartenden Daten des Tevatron Run II möglich machen. Der Run II des Tevatron-Colliders hat gerade begonnen, nachdem der Beschleuniger-Komplex und die Experimente D0 und CDF umgebaut wurden. Ziel des Umbaus war es, eine erheblich höhere Luminosität bei einer höheren Schwerpunktsenergie von 2 TeV zu erreichen.
Die CDF Spurdetektoren wurden gegenüber Run I drastisch verbessert und decken die gesamte Wechselwirkungszone ab. Innerhalb einer neuen Driftkammer befindet sich der SVXII-Detektor mit 5 Lagen doppelseitiger Silizium-Streifen-Detektoren in radialen Abständen zwischen 2.7 cm und 10.7 cm vom Strahl. Zwei weitere Lagen in Abständen von ca. 20 cm und ca. 28 cm bilden die sogenannten Intermediate Silicon Layers (ISL). Eine zusätzliche Lage einseitiger Silizium-Streifen-Detektoren ist im Abstand von nur 1.6 cm zum Strahl direkt auf das Strahlrohr montiert. Damit haben sich die B-Physik-Fähigkeiten von CDF drastisch verbessert. Mit einer innerhalb von zwei Jahren erwarteten integrierten Luminosität von 2 fb^{-1} wird

der statistische Fehler einer Lebensdauermessung vollständig rekonstruierter B-Mesonen im Bereich von 0.5 % liegen. Der statistische Fehler der Λ_B-Lebensdauer, gemessen im exklusiven Kanal $\Lambda_B \to J/\psi\ \Lambda$, kann gegenüber dieser Messung um einen Faktor 8 verkleinert werden. In diesen Zahlen ist die verbesserte Detektorauflösung noch nicht berücksichtigt worden. Sie sind deshalb eine konservative Schätzung.

Das Institut für Experimentelle Kernphysik der Universität Karlsruhe war maßgeblich am Bau des ISL beteiligt. Neben der Entwicklung und Produktion von Präzisionsklebevorrichtungen und dem Test von Silizium-Detektoren wurde im Rahmen dieser Arbeit Software für ein Teststandsystem entwickelt, das sowohl während der Prototyp-Phase der SVXII- und ISL-Auslese-Elektronik als auch während der Produktion von SVXII-Leitern und ISL-Modulen[9] zum Einsatz kam. Das kostengünstige, PC-basierte System ermöglicht einfache Funktionstests sowie Langzeit-Tests ("Burnin") der SVXII- und ISL-Bauelemente.

[9]Eine SVXII-"Leiter" bzw. ein ISL-Modul sind Bauelemente, bestehend aus mehreren Silizium-Streifen-Detektoren und einem Auslesehybrid, aufgeklebt auf eine Karbonfaser-Struktur und verbunden durch Microbonds.

Chapter 1

Introduction

This section gives an overview of particle physics with emphasis on the topics relevant for the measurement described in this dissertation. After a brief introduction into the basic concepts of the "Standard Model", the production, hadronization and decay of b quarks is discussed.

1.1 The Standard Model of Particle Physics

The Standard Model (SM) describes the fundamental particles and the interactions between them. It is built from many theoretical and experimental studies during the last decades and is in excellent accord with almost all current data. The fundamental particles are classified according to their intrinsic angular momentum, the spin. Particles with half-integer spin are called fermions and particles with integer spin are bosons. The fermions are divided into quarks and leptons which are arranged in three generations that are similar in every attribute except their masses (Table 1.1). Leptons are directly observable in nature. Free quarks however are not observed, a fact which is attributed to the nature of the strong interaction binding them to multiplets.

Generation:	1	2	3	I_3	Y	Q
Leptons	$\begin{pmatrix} \nu_e \\ e \end{pmatrix}_L$	$\begin{pmatrix} \nu_\mu \\ \mu \end{pmatrix}_L$	$\begin{pmatrix} \nu_\tau \\ \tau \end{pmatrix}_L$	$1/2$ $-1/2$	-1 -1	0 -1
Quarks	$\begin{pmatrix} u \\ d \end{pmatrix}_L$	$\begin{pmatrix} c \\ s \end{pmatrix}_L$	$\begin{pmatrix} t \\ b \end{pmatrix}_L$	$1/2$ $-1/2$	$1/3$ $1/3$	$2/3$ $-1/3$

Table 1.1: The three fermion generations of the Standard Model. The quantum numbers of the third component I_3 of weak isospin, weak hypercharge Y and the charge Q are given. They are related by $Q = I_3 + \frac{1}{2}Y$.

Macroscopic matter consists of the fermions of the first generation. The first generation includes the up (u) and down (d) quarks that are the constituents of the protons and neutrons in the nucleus and the electron and its neutrino. The quarks of the second generation are the charm (c) and the strange (s) quarks, the leptons are the muon and its neutrino. The particles of the second generation decay via the weak force to the quarks and leptons of the first generation. In nature, muons and bound states of s quarks, the kaons, can be observed in cosmic ray air showers which are induced by high energy cosmic particles hitting the atmosphere. The third generation consists of the bottom (b) and the top (t) quarks as well as the τ lepton and its neutrino. These particles can be produced at particle accelerators. For every charged particle there is an associated particle which is in all respects, except for the opposite signed charge, identical to the particle itself. These associated particles are called antiparticles. The antiparticles of the negative charged leptons are the positive charged antileptons, e.g. the positron e^+ which is the antiparticle of the electron e^-.
Interactions between fermions can be described by the exchange of bosons which are therefore also called "force carriers", e.g. is the electromagnetic force between charged particles mediated by photons which have spin 1 and thus are bosons. The four known fundamental interactions are listed in Table 1.2 together with their corresponding bosons.

Interaction	Bosons	Symmetry group	interaction couples to
strong	8 gluons g	SU(3)	quarks
weak	Z^0, $W^\pm$	SU(2)	quarks, leptons
electromagnetic	γ	U(1)	quarks, leptons
Gravitation	Graviton ?	SO(3,1)	quarks, leptons

Table 1.2: The four known fundamental interactions with the bosons mediating the interactions. Gravitation is not included in the SM but is listed for the sake of completeness. The Graviton is the (hypothetical) boson transmitting the interaction.

For a theoretical description it has proven reasonable to construct a Lagrange density similar to the Lagrange function in classical physics. One starts with a density for fermions without the interactions between them. The interactions and corresponding bosons are then introduced by requiring the Lagrange density to be invariant with respect to certain groups of gauge transformations. All known interactions of the SM can be deducted by requiring local gauge-invariance with respect to to the symmetry groups U(1), SU(2) and SU(3). The strong interaction is described by the Quantum Chromodynamics (QCD) using the property of colour $\mathrm{SU}(3)_C$ group symmetry. Quarks and gluons carry this colour property. The weak and electromagnetic interaction are unified to the electroweak interaction transmitted by the exchange of the $W^\pm$, Z^0 and γ bosons. The electroweak theory involves the $\mathrm{SU}(2)_L \times \mathrm{U}(1)_Y$ group. Fermions can exist in a state of being "left-handed" or "right-handed" (ex-

cept for neutrinos which are only left-handed in the SM). The L in the SU(2) group means, that the interaction affects only left-handed fermions. Y is the weak hypercharge, a quantum number similar to the electric charge. It is related to the electric charge Q and the third component of the weak isospin I_3 which is a quantum number similar to the spin. The strong interaction, carried by the gluons, is described adequately by the QCD. The properties of the $W^{\pm}$ and Z^0 bosons however are not described correctly by the electroweak theory since they have rather high masses and the introduction of mass terms into the electroweak Lagrange density leads to non-renormalizable divergences. Therefore a new formalism was introduced in which these divergences do not appear. In this formalism it is assumed that the various particles interact with a new type of scalar field, called the Higgs field, which has a non-zero vacuum expectation value ϕ_0. A consequence of the Higgs field is that there is an electrically neutral spin-0 particle, the Higgs boson H^0. The Higgs boson has not yet been observed in experiments but searches for it are a high priority for the upcoming collider experiments.
Even though the Standard Model describes the fundamental particles and their interactions very well, it has many free parameters which have to be determined by experiment.

1.2 THE HISTORY OF THE QUARK MODEL

During the 1950's and 60's, a variety of unstable particles was discovered in cosmic rays and later on in accelerator experiments which could be distinguished from the leptons in that they take part in strong interactions. These particles were called hadrons. The hadrons are subdivided into two types based on their spin. Baryons are fermions while mesons are bosons. In 1961 Gell-Mann showed that hadrons could be classified into groups of baryons or mesons with the same spin and parity and similar masses [1]. Each group – also called "supermultiplet" – contains several isospin multiplets. The arrangement of hadrons within these supermultiplets displayed patterns of charge, isospin and strangeness[1] based on the symmetry group SU(3).
This was the start of the quark model in which hadrons are described as bound states of fundamental spin-$\frac{1}{2}$-particles, the quarks. Mesons are quark-antiquark pairs and baryons are states of three quarks. At the time, all known hadrons could be classified using three quarks known as "up", "down" and "strange". A series of deep-inelastic electron-proton scattering experiments at SLAC[2] in the late 1960's and early 1970's provided evidence for a sub-structure of the protons [2]. The results indicated that the electrons were scattering off point-like, charged objects within the proton. This was the first evidence for the physical existence of quarks. In November 1974, a "revolution" took place in particle physics when experiments at two different

[1] A property of matter, expressed as a quantum number s, postulated to account for the unusually long lifetime of some hadrons.
[2] Stanford Linear Accelerator Center, Stanford, California, U.S.A.

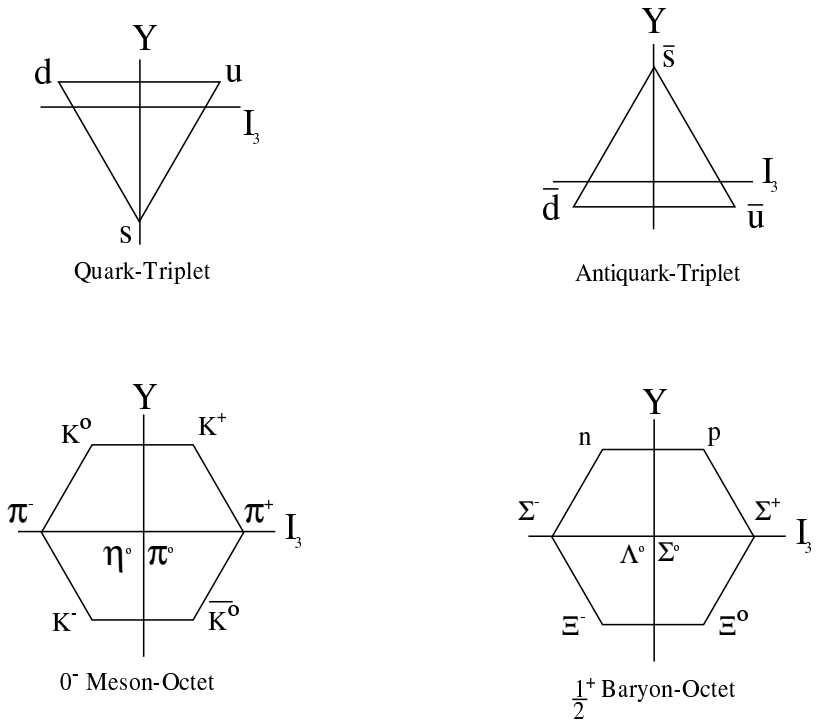

Figure 1.1: Examples of quark- and hadron-multiplets in the SU(3) quark model. The particles are arranged according to their weak hypercharge Y and the third component of the weak isospin I_3.

laboratories discovered a narrow resonance at 3.1 GeV/c^2. The new particle was observed at BNL[3] [3] where it was named J and SLAC [4] where the particle was named ψ. The new particle, now called J/ψ, could be explained as a bound state of a new quark type, the charm quark. The other hadrons known until 1974 fit into a theoretical model with only the three quarks mentioned above. At the time theorists already suggested a third generation of fermions. The discovery of the τ lepton in 1975 [5] supported the existence of a third family and a fifth and sixth quark. In 1977 the bottom (or "beauty") quark was discovered at Fermilab[4] as a resonance in the dimuon invariant mass spectrum in 400 GeV proton-nucleus collisions [6]. Soon after the discovery of this new $b\bar{b}$ bound state, the so-called Υ resonance was confirmed in e^+e^- collisions at the DORIS storage ring at DESY[5] [7]. Subsequently, a variety of bound states of the new quark were discovered. In the year 1995, the observation of the sixth quark called "top" was finally reported by the CDF[6] [8] and D0 [9] collaborations at Fermilab.

[3]Brookhaven National Laboratory
[4]The Fermi National Accelerator Laboratory, Batavia, Illinois, U.S.A.
[5]Deutsches Elektronen SYnchrotron.
[6]The Collider Detector at Fermilab

1.3 THE CKM MATRIX

In the Standard Model with SU(2) × U(1) as the gauge group of electroweak interactions, the left-handed quarks are arranged in doublets (Table 1.1). An important factor concerning electroweak interactions is the fact that the quark mass eigenstates are not identical to the weak eigenstates. The matrix relating these bases was defined for six quarks by Kobayashi, Maskawa in 1973 [10]. The matrix is known as Cabibbo-Kobayashi-Maskawa Matrix (V_{CKM}) since it generalises the four-quark case where the matrix is parameterised by a single angle, the Cabibbo angle θ_c [11]. By convention, V_{CKM} operates on the charge -1/3 quark mass eigenstates while the u, c and t quarks are unmixed.

$$\begin{pmatrix} d' \\ s' \\ b' \end{pmatrix} = \begin{pmatrix} V_{ud} & V_{us} & V_{ub} \\ V_{cd} & V_{cs} & V_{cb} \\ V_{td} & V_{ts} & V_{tb} \end{pmatrix} \begin{pmatrix} d \\ s \\ b \end{pmatrix} \tag{1.1}$$

d', s' and b' are the weak eigenstates. The coupling of two quarks q_1, q_2 to a W-boson is proportional to the matrix element $V_{q_1 q_2}$.
The Wolfenstein parameterisation [12] emphasises the relative size of the matrix elements by expressing them in powers of $\lambda = sin(\theta_c) \approx 0.22$. V_{CKM} is approximated in terms of the real variables λ, A, ρ and a the phase η.

$$V \sim \begin{pmatrix} 1-\lambda^2/2 & \lambda & A\lambda^3(\rho - i\eta) \\ -\lambda & 1-\lambda^2/2 & A\lambda^2 \\ A\lambda^3(1-\rho-i\eta) & -A\lambda^2 & 1 \end{pmatrix} \tag{1.2}$$

Note that the Wolfenstein parameterisation is only correct to order λ^3 in the matrix elements.
The study of B decay properties can give information on certain V_{CKM} matrix elements involving b quarks. $|V_{cb}|$ can be determined by measuring the inclusive b-hadron lifetime when the semileptonic branching ratio and the ratio $|V_{ub}|/|V_{cb}|$ are known [13]. $|V_{ub}|/|V_{cb}|$ is determined by measuring the relative strength of $b \to u$ and $b \to c$ transitions in semileptonic B decays. The study of $B_d^0 - \bar{B}_d^0$ and $B_s^0 - \bar{B}_s^0$ flavour oscillations that occur at one-loop level gives information on V_{CKM} matrix elements involving the top quark. The ratio $|V_{td}|/|V_{ts}|$ can be determined by measuring the mass differences of the B_d^0 and B_s^0 mass eigenstates.
The current 90% confidence limits on the magnitude of the elements of the matrix are [14]:

$$\begin{pmatrix} 0.9742 - 0.9757 & 0.219 - 0.226 & 0.002 - 0.005 \\ 0.219 - 0.225 & 0.9734 - 0.9749 & 0.037 - 0.043 \\ 0.004 - 0.014 & 0.035 - 0.043 & 0.9990 - 0.9993 \end{pmatrix}$$

1.4 Production and Fragmentation of b-Quarks in Hadronic Collisions

The most appealing feature of hadron colliders like the Tevatron as tools to study B physics is their very high cross section for $b\bar{b}$ production. On the other hand, events containing b quarks are a very small fraction of the total event rate (Table 1.3). Therefore the challenge of doing B physics at a hadron collider is to efficiently trigger on events where b quarks were produced. Until now, this was only possible by triggering on high-P_T leptons or dimuons consistent with $J/\psi \rightarrow \mu^+\mu^-$.

	CESR,DORIS KEK,SLAC e^+e^- at $\Upsilon(4S)$ $\sqrt{s}$=10.5 GeV	SLAC (BaBar) KEK (Belle) e^+e^- at $\Upsilon(4S)$ asymmetric $\sqrt{s}$=10.5 GeV	LEP,SLC e^+e^- at Z^0 $\sqrt{s}$=91. GeV	TEVATRON (CDF) $p\bar{p}$ $\sqrt{s}$=1.8 TeV
$\sigma_{b\bar{b}}$	$\approx$ 1 nb	$\approx$ 1 nb	$\approx$ 7 nb	$\approx$ 50 μb
$\sigma_{b\bar{b}}/\sigma_{tot}$	0.28	0.28	0.22	$\approx 8 \times 10^{-4}$
B^0, B^+	yes	yes	yes	yes
$B_s^0, B_c^+, \Lambda_b^0$	no	no	yes	yes
Boost $< \beta\gamma >$	0.06	0.54	6	2-4

Table 1.3: Different accelerators producing b quarks compared with respect to energy, $b\bar{b}$ cross sections, the produced hadrons and kinematics.

In high energy collisions, the proton and antiproton can be characterised as bunch of free partons: the three valence quarks, virtual gluons and the sea quarks (quark-antiquark pairs). The problem of b quark formation in $p\bar{p}$ collisions can thus be thought of a series of interactions in which partons of the proton react with the partons of the antiproton. The different partons do not necessarily divide up the proton energy equally. The distribution of partons within the proton and antiproton is described by a parton distribution function (PDF) $F_i^a(x, q^2)$ which is the number density of parton i (quark or gluon) carrying the momentum fraction x of the hadron a (proton or antiproton) when probed at momentum transfer q^2. The partonic cross section can be calculated as a perturbative series in α_s, the QCD coupling parameter. The cross section for b quark production in $p\bar{p}$ collisions is then obtained by convoluting the partonic cross section with the PDF. Important contributions to the cross section are $\mathcal{O}(\alpha_s^2)$ quark–antiquark annihilation or gluon–gluon fusion processes like $q\bar{q} \rightarrow b\bar{b}$ and $gg \rightarrow b\bar{b}$. Figure 1.2 depicts Feynman diagrams of these lowest order $b\bar{b}$ production processes.
However, next-to-leading order calculations [15] show that the $\mathcal{O}(\alpha_s^3)$ terms can contribute to the cross section by amounts comparable to the $\mathcal{O}(\alpha_s^2)$ contributions, if

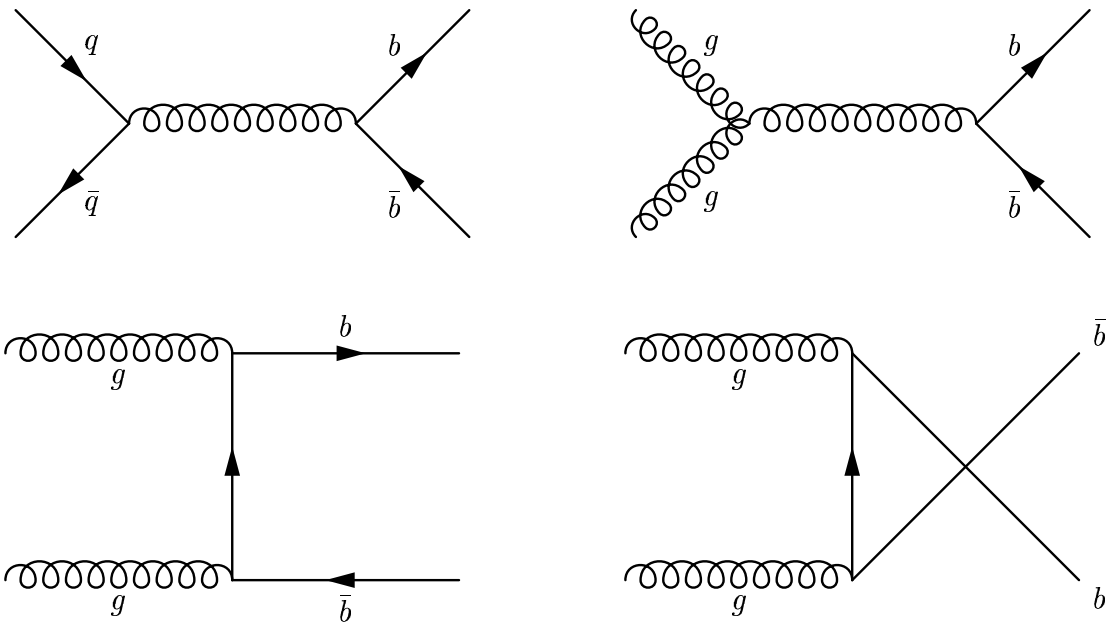

Figure 1.2: Lowest order ($\mathcal{O}(\alpha_s^2)$) Feynman diagrams for $b\bar{b}$ production through quark–antiquark annihilation and gluon–gluon fusion.

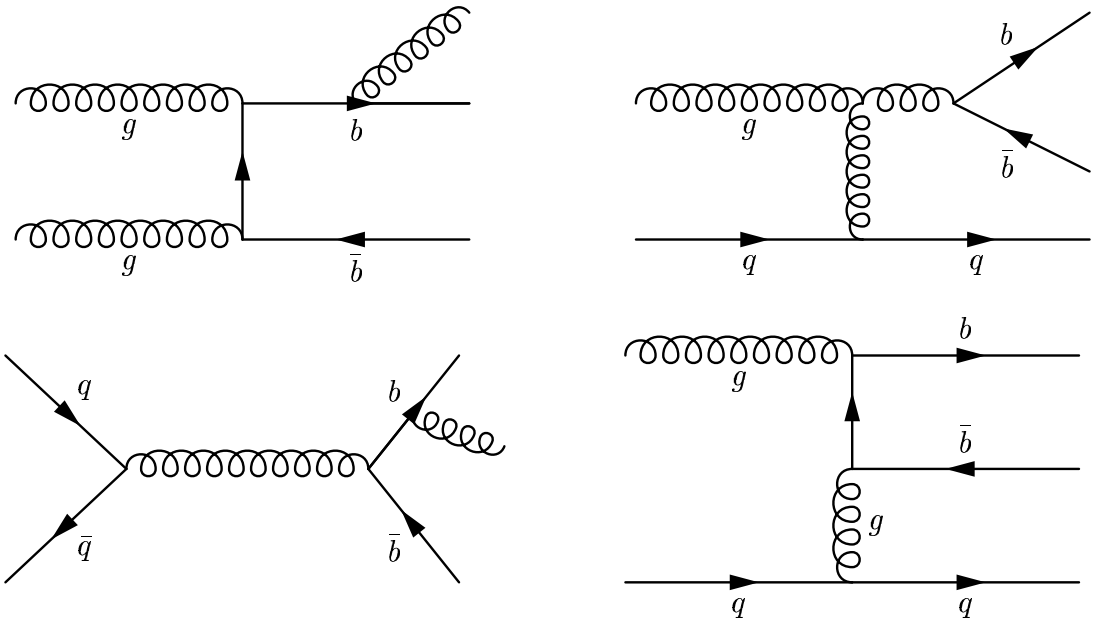

Figure 1.3: Examples of Feynman diagrams for $b\bar{b}$ production at next-to-leading order ($\mathcal{O}(\alpha_s^3)$)

.

the hadron-hadron center-of-mass energy is much larger than the b quark mass. This is the case for the Tevatron. Some $\mathcal{O}(\alpha_s^3)$ processes are illustrated with Feynman diagrams in Figure 1.3. These processes are the source of $b\bar{b}$ pairs that are close together and do not necessarily appear in the central detector region as compared to the $\mathcal{O}(\alpha_s^2)$ processes which result in back-to-back quark pairs.
CDF has measured the b-quark production cross section in $p\bar{p}$ collisions at $\sqrt{s} = 1.8$ TeV using different data samples. The results are shown compared to next-to-leading order QCD calculation in Figure 1.4 (taken from [16]). The distribution is a b-quark differential spectrum integrated above a given threshold $p_{T,min}$. The cross section falls steeply with increasing $p_{T,min}$. As a consequence, P_T-thresholds in b-triggers should be as low as possible.

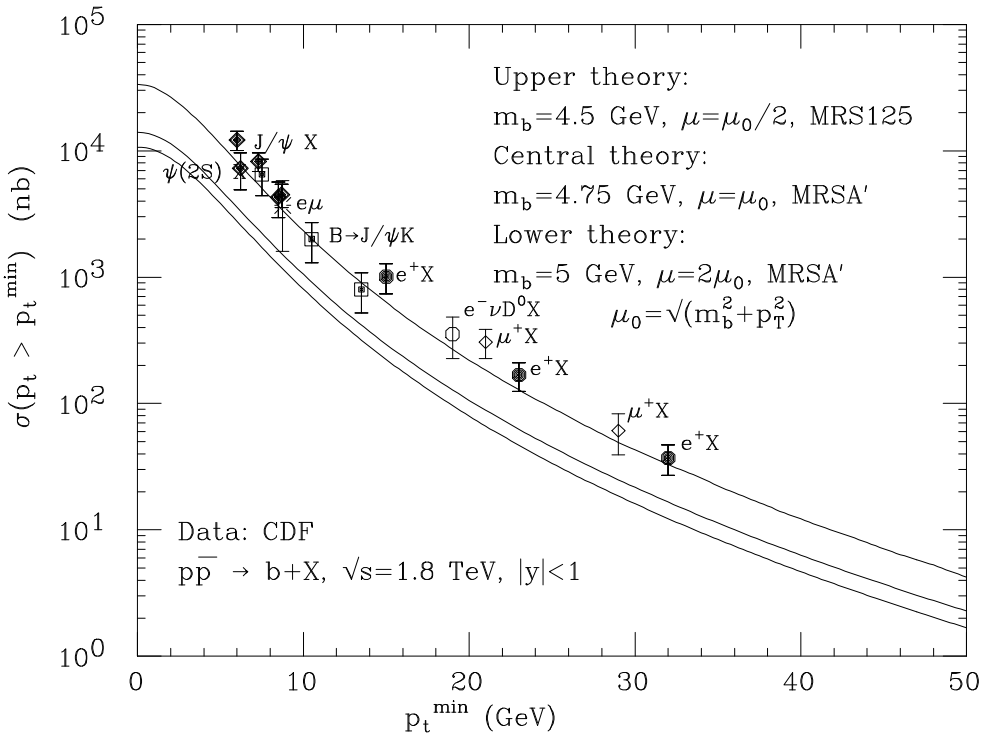

Figure 1.4: Compilation of the CDF b-quark integral cross-section measurements and comparison with next-to-leading order QCD predictions.

The process of forming B-hadrons from the b-quarks produced in the initial hard scattering process is called hadronization or fragmentation. This is a long-distance, non-perturbative QCD process which can only be described by phenomenological models. A commonly used approach is the string fragmentation model [17] which is very successful in describing experimental data. In this model, the quark-antiquark pair separates with $v \approx c$. Between the colour-charged partons a field of gluons is formed, the "string". The energy density within the string has a constant value of ≈ 1 GeV/fm. As the quark and antiquark, or more generally the two colour-charged objects, separate more and more, the energy in the string raises until it is large enough to create a new quark-antiquark pair out of the vacuum. This is

schematically shown in Figure 1.5. The new quarks form the new ends of the string. These new strings also stretch and break, producing more quark-antiquark pairs until there is no longer sufficient energy available.

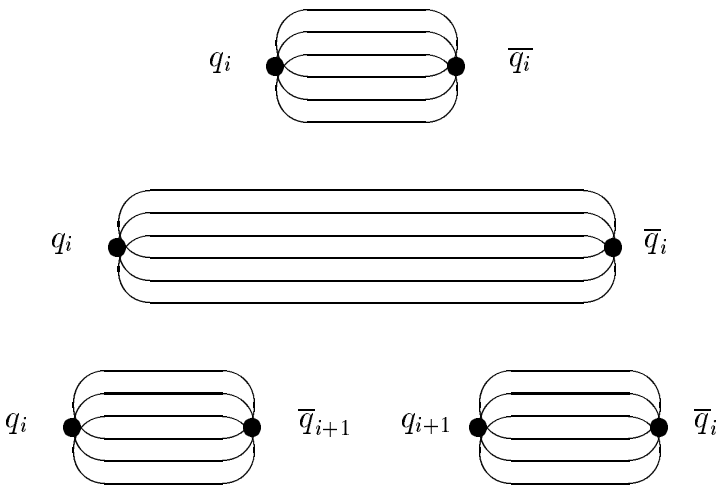

Figure 1.5: Schematic view of the String-Fragmentation.

The fraction of the initial b quark energy transfered to the B hadron is described by a fragmentation function. The fragmentation of light quarks (u, d, s) is often described by the "symmetric LUND function" [18]:

$$f(z) = \frac{(1-z)^a}{z} \cdot e^{-bm_T^2/z} \tag{1.3}$$

where a and b are free parameters and $m_T^2 = m^2 + p_T^2$ with the transverse momentum of the quark p_T. The variable z is defined as

$$z = \frac{E_B + p_{||}(B)}{E_b + p_q} \tag{1.4}$$

where $p_{||}(B)$ is the projection of the momentum of the hadron onto the direction of the quark before the fragmentation. Heavy quark fragmentation is commonly described by the Peterson model [19]:

$$f(z) = \frac{1}{z} \cdot \left(1 - \frac{1}{z} - \frac{\epsilon_b}{1-z}\right)^{-2} \tag{1.5}$$

ϵ_b, the Peterson parameter, was measured to have a value of $\epsilon_b = 0.006 \pm 0.002$ [20]. Figure 1.6 shows the fragmentation function of b-quarks compared to that of lighter quarks. Heavy quark fragmentation is "hard", that is the b and c hadrons carry in average a large fraction of the quark momentum. It should be emphasized that these fragmentation functions are highly scheme dependent at next-to-leading order QCD.

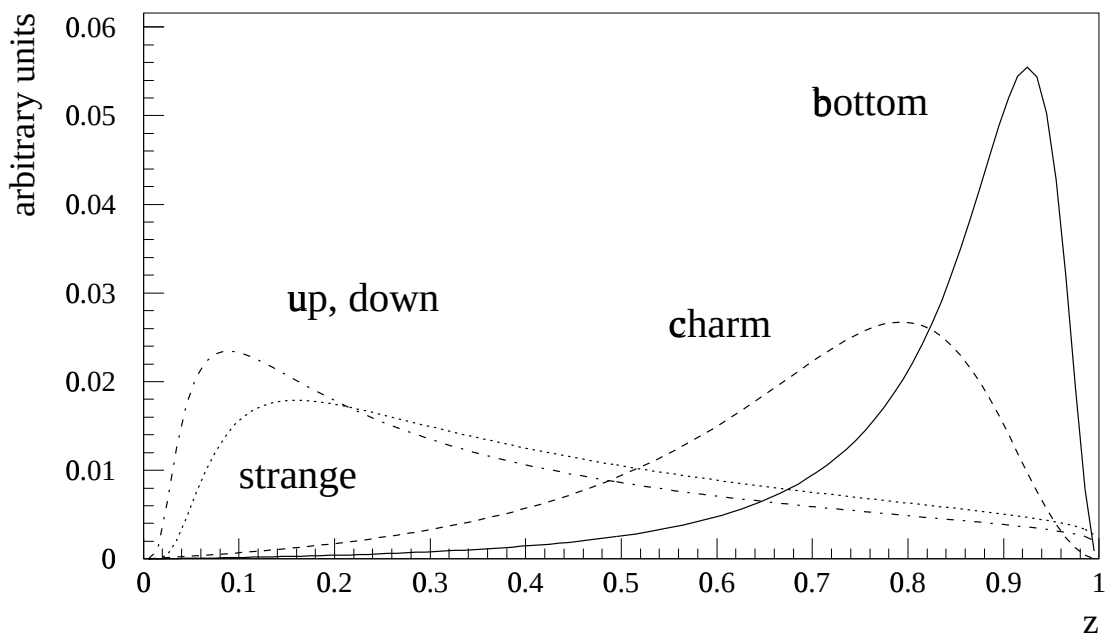

Figure 1.6: Fragmentation functions for light and heavy quarks.

1.5 The lifetime of B-Mesons

In 1983 the MARK II [21] and MAC [22] collaborations measured a B-hadron mean lifetime of $\approx$1.2 ps. This result was an order of magnitude higher than expected for the case that the strength of the mixing between the 2nd and 3rd quark generations is the same as for the mixing between the 1st and 2nd generations. The long b-lifetime was the first indication that the coupling between the 2nd and 3rd generations is much weaker than that between the 1st and the 2nd generations.
In the Standard Model, b-quarks can decay into a u-quark or a c-quark by coupling to a virtual W boson which decays into a quark-antiquark pair or a lepton-neutrino pair. The total width for the decay of b-quarks can therefore be broken into two terms, one for semileptonic and one for hadronic decays:

$$\Gamma_{tot} = \Gamma_{sl} + \Gamma_{had} \tag{1.6}$$

The lifetime is then given as

$$\tau_b = \frac{1}{\Gamma_{tot}} = \frac{Br_{sl}}{\Gamma_{sl}} = \frac{Br_{had}}{\Gamma_{had}} \tag{1.7}$$

with the semileptonic and hadronic branching ratios Br_{sl} and Br_{had}. From a theoretical point of view, the semileptonic decay channels have the advantage of fewer uncertainties. Furthermore, the semileptonic branching ratio Br_{sl} is the best measured. The lifetime equation (1.7) is given in terms of the b-quark but must be related to B-mesons. A first order approximation is the "spectator model" in which the b quark inside the B meson is assumed to be free. The other (light) quark in

the meson only acts as a spectator and is assumed to have a negligible effect on the b-quark decay.
Figure 1.7 shows Feynman diagrams of spectator model B meson decays. In the "colour-suppressed" diagram on the left, the B meson decays into a charmonium state (e.q. J/ψ) and a kaon. The decay only occurs, when the $\bar{c}s$ pair, itself a colour singlet, matches the colour of the c quark and the spectator-antiquark to form colour-singlet mesons. Within the spectator model, all B mesons and baryons will have the same lifetime. The semileptonic width Γ_{sl} is calculable from known properties of electroweak interaction and the couplings between the quark generations. The matrix element for b-quarks decaying to lighter quarks q can be written as the product of a leptonic and a hadronic current:

$$M_{sl} \;=\; -\frac{G_F}{\sqrt{2}}\, V_{qb}\, [\bar{q}\gamma^{\mu}(1-\gamma_5)b]\, [\bar{l}\gamma_{\mu}(1-\gamma_5)\nu_l] \tag{1.8}$$

where G_F is the Fermi coupling constant and V_{qb} is the appropriate CKM matrix element. By squaring M_{sl} and integrating over phase space, one obtains the decay width:

$$\Gamma_{sl}(b \to q) \;=\; \frac{G_F^2 m_b^5}{192\ \pi^3}|V_{qb}|^2 F(\epsilon) \tag{1.9}$$

where $F(\epsilon)$ is the phase space factor which is given by [23]:

$$F(\epsilon) \;=\; 1 - 8\epsilon^2 + \epsilon^6 - \epsilon^8 - 24\epsilon^4\ ln\ \epsilon \tag{1.10}$$

with $\epsilon = m_q/m_b$. In the Standard Model, a b-quark can only decay into a c- or a u-quark. τ_B measures therefore a combination of $|V_{ub}|^2$ and $|V_{cb}|^2$:

$$\tau_B \;=\; \frac{Br_{sl}}{\Gamma_{sl}} \;=\; \frac{Br_{sl}}{\frac{G_F^2 m_b^5}{192\ \pi^3}\cdot[F(\epsilon_u)|V_{ub}|^2 + F(\epsilon_c)|V_{cb}|^2]} \tag{1.11}$$

Since $|V_{ub}|^2 << |V_{cb}|^2$, the lifetime scale of B mesons is set by V_{cb}.
In the hadronic case, (1.9) has to be multiplied with 3 (for the number of possible

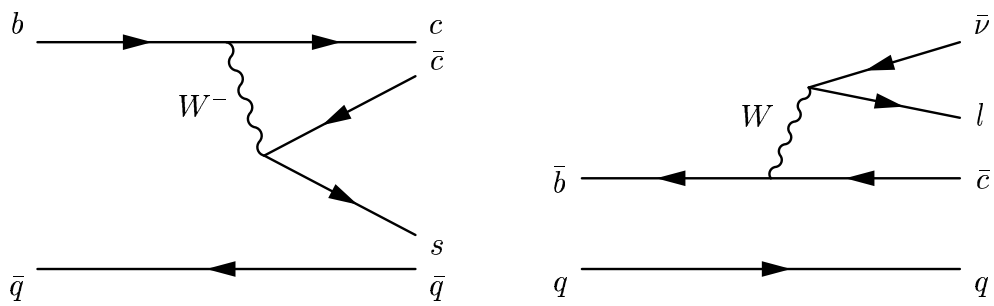

Figure 1.7: Spectator model Feynman diagrams of B meson decays with internal (left) and external (right) W emission. The diagram on the left describes the decay into charmonium modes: $B \to \psi K$. The diagram on the right shows a semileptonic decay $B \to Dl\bar{\nu}$.

quark colours) and $|V_{q_1 q_2}|^2$, the CKM matrix element of the two quarks resulting of the decay $W \to q_1 \bar{q}_2$. The quarks involved in the decay of the B meson may radiate gluons. Including this gluon radiation in (1.9) results in a correction factor of $[1 - (2\alpha_s/3\pi)g(\epsilon)]$ where $g(\epsilon) = (\pi^2 - \frac{31}{4})(1-\epsilon)^2 + \frac{3}{2}$.

To get a more accurate value for the lifetime of B mesons, corrections from various other sources have to be considered. Non-spectator decays include contributions like W exchange processes for neutral B mesons or weak annihilation of charge B mesons as shown in Figure 1.8. Other non-spectator mechanisms are caused by final state Pauli interference effects. As an example, Figure 1.9 shows two interfering diagrams for the decay $B^+ \to \bar{D}^0\ \pi^+$ with the same final state particles. In the past few years, calculations in the framework of the Heavy Quark Effective Theory (HQET) provided quantitative predictions for the lifetimes of the different B meson species (see e.g. [24]). In the HQET model, the configuration of the light quarks in the hadron becomes independent of spin and flavour of the heavy quark Q in the limit $m_Q \to \infty$. The expectation for the lifetime hierarchy of the different B hadrons is

$$\tau_{\Lambda_B} \ < \ \tau_{B^0} \ < \ \tau_{B^+} \tag{1.12}$$

with a difference of $\approx 5\%$ between the lifetimes of the different B hadron species. Measurements of the lifetime of individual B hadron species can therefore probe B decay mechanisms beyond the simple spectator model.

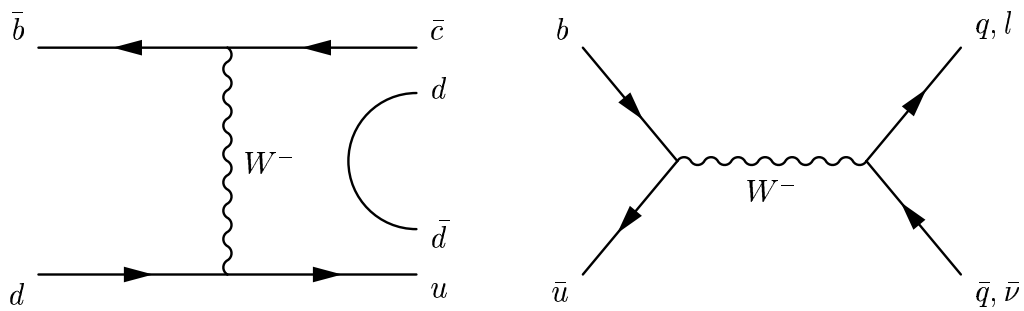

Figure 1.8: A B^0 decays into $D^-\pi^+$ via W exchange (left). A B^- decaying via weak annihilation is shown on the right.

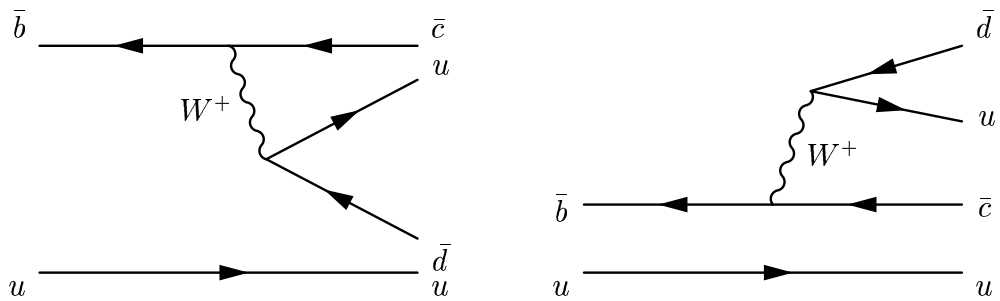

Figure 1.9: Illustration of internal (left) and external (right) W emission for the decay $B^+ \to \bar{D}^0\ \pi^+$.

Chapter 2

The Fermilab Accelerator and the CDF Experiment

In this chapter, the Fermilab accelerator complex and the CDF detector are described in their Run I configuration. In the 1970's, both CERN[1] and Fermilab started to develop proton–antiproton colliders. In the collisions, the p and $\bar{p}$ can be regarded as a package of partons – quarks and gluons – with a broad spectrum of energies, thus only a fraction of the $p\bar{p}$ center-of-mass energy is available for each parton–parton interaction.

2.1 The Tevatron

The world's highest energy particle collider, the Tevatron at Fermilab, was developed in the 1970's and completed in 1985 when the first $p\bar{p}$ collisions were produced. The first data taking run took place in the years 1988/89. The two main run periods were Run Ia (1992–1993) and Run Ib (1994–1996). It is a synchrotron type machine in which counter-rotating p and $\bar{p}$ beams are accelerated in the same beampipe to a center-of-mass energy of 1.8 TeV. The two beams collide head on in the center of the two large particle detectors, D0[2] and CDF. To achieve this high energy, several stages of acceleration are necessary which are described in the following. The Fermilab accelerator complex is shown schematically in Figure 2.1. The acceleration process begins with the production of H^- ions by adding an electron to hydrogen atoms in an ion source. A Cockroft-Walton accelerator [26] with a potential difference of 750 kV accelerates the hydrogen ions into a linear accelerator (LINAC) which is approximately 150 m long. The LINAC consists of a series of copper drift tubes spaced further and further apart. A radio frequency (RF) potential difference is applied to alternating tubes, such that the ions are accelerated each time they traverse a gap between tubes. The final energy of the ion beam leaving the LINAC is 400 MeV[3]. At this point, prior to entering the next machine, the ions pass through

[1] Conseil Européenne pour la Recherche Nucléaire, Geneva, Switzerland

[2] D0 is named after the building where the detector is located at the Tevatron ring.

[3] Prior to an upgrade in 1993 the energy was 200 MeV

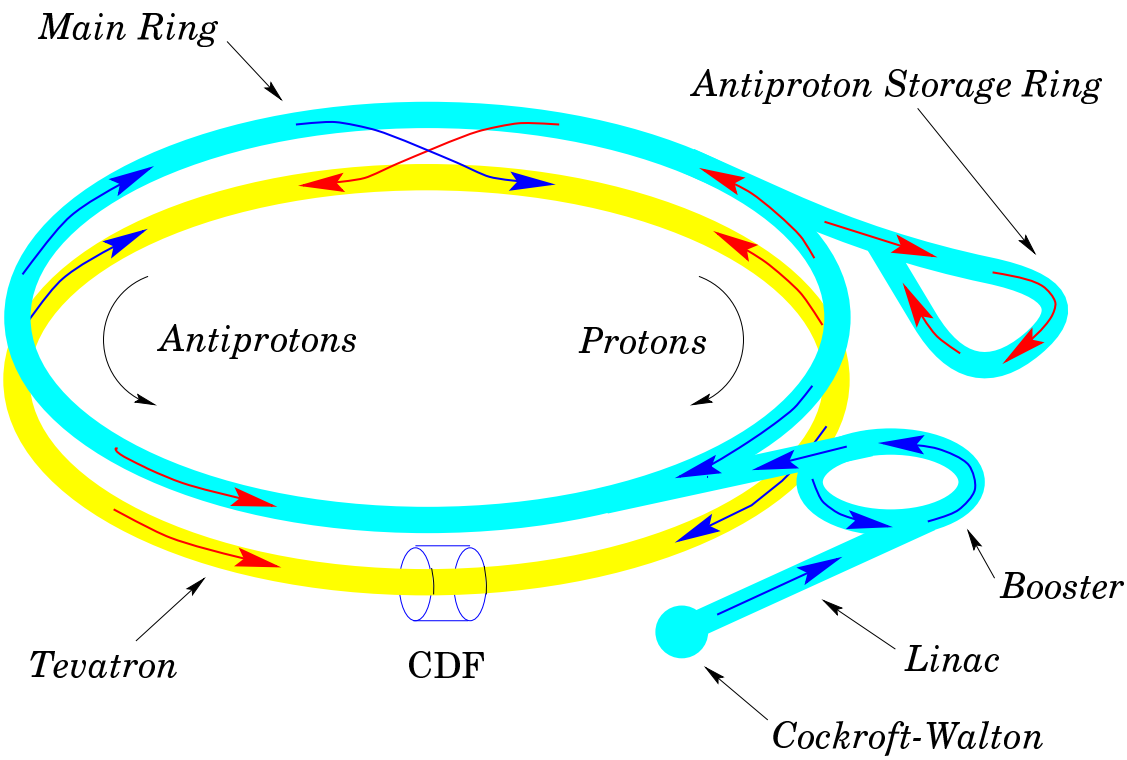

Figure 2.1: An overview over the Fermilab accelerator complex during Run I.

a carbon foil to strip off the two electrons from the proton.
The next stage of acceleration is performed by a rapid cycling synchrotron called the 'Booster' with a radius of 75 m. The protons travel around the Booster about 20000 times and their energy is raised to 8 GeV. The Booster completes acceleration cycles with a rate of 15 Hz and loads 12 proton bunches at a time into the Main Ring.
The Main Ring, the former major accelerator at Fermilab, is a synchrotron with a circumference of 6300 m. It shares the tunnel 6 m underground with the Tevatron. The Main Ring keeps the particles in orbit with conventional copper–coiled magnets and accelerates them to 150 GeV. The protons are then transferred into the Tevatron in six bunches of typically 2.5×10^{11} protons each[4].
Antiproton production [27] is accomplished by extracting 120 GeV protons from the Main Ring and directing them onto a copper target[5]. Antiprotons are produced in the resulting proton–nucleus collisions among many other secondary particles. They are extracted and focused using a cylindrical lithium magnetic lens carrying a pulsed 0.4 MA axial current and sent into the Debuncher [28], a storage ring similar in size to the Booster. Here, the momentum spread of the antiprotons and the beam emittance[6] are reduced by the process of stochastic cooling [29]. The antiprotons are transferred to the Accumulator Ring which is concentric with the Debuncher.

[4] 12×10^{10} protons during Run Ia
[5] Other materials have also been used.
[6] The beam emittance is the phase space volume of the beam.

Here successive injections are stacked together and cooled further. The Accumulator collects antiprotons at a rate of typically 7×10^{10} per hour. The kinetic energy of the antiprotons in both rings is 8 GeV. When a sufficient number of antiprotons has been produced, they are transferred into the Main Ring, accelerated to 150 GeV and injected into the Tevatron in six bunches of typically 7.5×10^{10} antiprotons[7] circulating counterclockwise.
The Tevatron [30] is the last stage of the accelerator complex. Over 1000 superconducting NbTi dipole magnets [31] cooled to 4.6 K using liquid helium are used to bend the beams. They achieve a bending field of 4.4 Tesla. The superconducting technology allows smaller magnets with less energy consumption than normal magnets. In the Tevatron protons and antiprotons are simultaneously accelerated up to 900 GeV. The acceleration is performed by 8 RF cavities operating at 53 MHz. Four of them add approx. 1/3 MeV each to the proton energy per pass and four do the same for the antiprotons. The most important parameter of a particle collider, besides the maximum center-of-mass energy, is the luminosity $\mathcal{L}$. The luminosity is defined by the relation

$$\frac{dN}{dt} = \mathcal{L}\sigma$$

where $\frac{dN}{dt}$ is the rate at which interactions occur and σ is the total cross section (in cm^2). At the Tevatron, the luminosity is controlled by several parameters:

$$\mathcal{L} = \frac{N_p N_{\bar{p}} B f_0}{4\pi\sigma_x\sigma_y}$$

N_p and $N_{\bar{p}}$ are the number of protons and antiprotons per bunch, B is the number of bunches (6) and f_0 is the revolution frequency ($\approx$ 50 kHz). σ_x and σ_y characterize the Gaussian beam profile in x and y ($\approx 2.5 \times 10^{-3}$ cm). The peak instantaneous luminosity during Run Ib exceeded $\mathcal{L} = 2 \times 10^{31}\ \mathrm{cm}^{-2}\mathrm{s}^{-1}$. The integrated luminosity collected by CDF during Run I of the Tevatron is shown in Figure 2.2.

2.2 THE CDF EXPERIMENT

The CDF Detector [32][33] is a multi purpose particle detector to measure momentum, energy and type of particles produced in $p\bar{p}$ collisions at $\sqrt{s} = 1.8$ TeV. It is approximately 27 m long, 10 m high and weighs about 5000 tons. A collider detector cannot provide complete (4π steradian) solid angular coverage around the interaction point. The emphasis of CDF is on central coverage, extending forward as far as is practical. The term "central" refers to the direction orthogonal to the beamline, whereas "forward" implies small angles with respect to the beamline.
CDF has a cylindrical geometry and is therefore both axially and forward–backward symmetric (see Figure 2.3). Detection systems are arranged concentrically around the beamline. Figure 2.4 shows a cross section of the CDF detector. The innermost detector component is the Silicon Vertex Detector (SVX) surrounded by a

[7] 4×10^{10} antiprotons during Run Ia

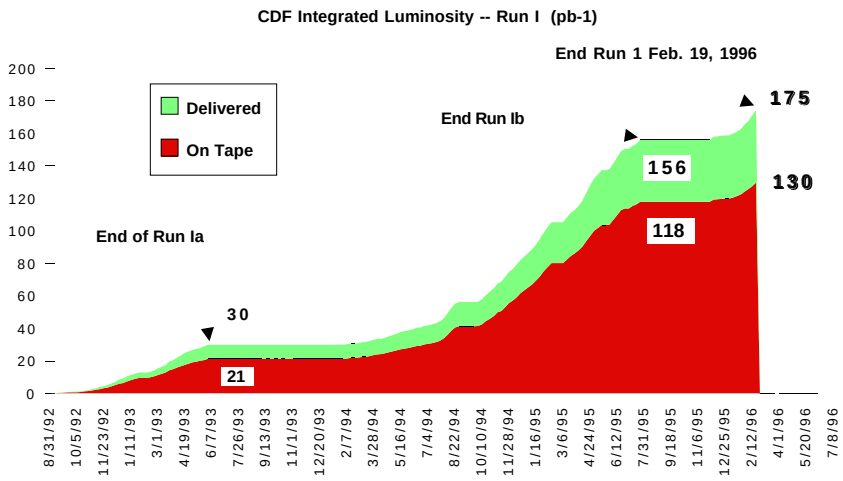

Figure 2.2: Time profile of the luminosity delivered by the Tevatron Collider and accumulated by the CDF experiment throughout Run I.

vertex time projection chamber (VTX) and the Central Tracking Chamber (CTC), a large drift chamber, 3.2 m long, with an inner radius of 0.3 m and an outer radius of 1.3 m. SVX and CTC will be described in more detail later. The VTX has good reconstruction capabilities in the r–z plane and can be used to reconstruct the z–position of interaction vertices with an accuracy of about 1 mm. The tracking

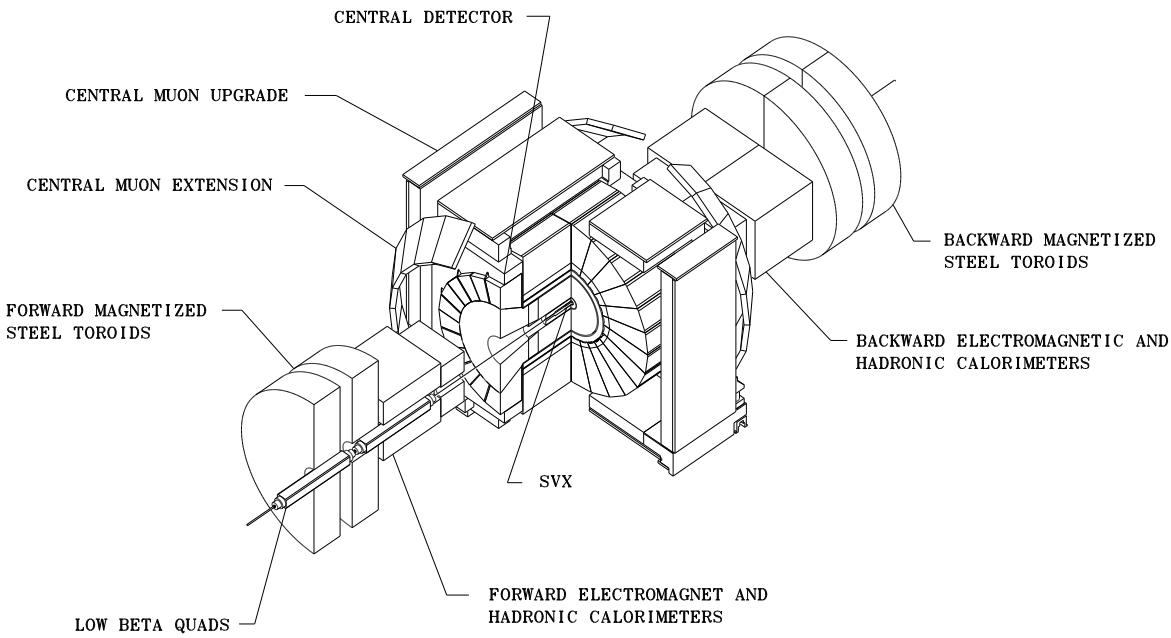

Figure 2.3: Isometric view of the CDF detector during Run I.

system, consisting of SVX, VTX and CTC is located interior of a solenoid magnet [34]. The superconduction coil is designed to produce a 1.5 Tesla magnetic field at 5000 Amperes but was operated at 1.4 Tesla during Run I. The coil consists of niobium titanium wires embedded in copper and cooled by two phase helium to the operation temperature of 4.5 K. The magnetic flux return is provided by an iron yoke. Surrounding the solenoid are calorimeter systems used to measure the energy of electrons, photons and hadronic jets.
The coordinate system of CDF is a right–handed system with the origin at the center of the detector. The z direction points along the proton beam, West to East, the y axis points vertically upward and the x axis points radially outward from the Tevatron ring. The azimuthal angle ϕ is measured with respect to the positive x–axis and increasing towards the positive y–axis. θ is the polar angle with respect to the proton beam direction. The *pseudorapidity*, which is defined as $\eta = -ln\,(tan\,\theta/2)$, is more commonly used than the polar angle. It is a good approximation of the true lorentz invariant rapidity velocity variable when the particle is relativistic.

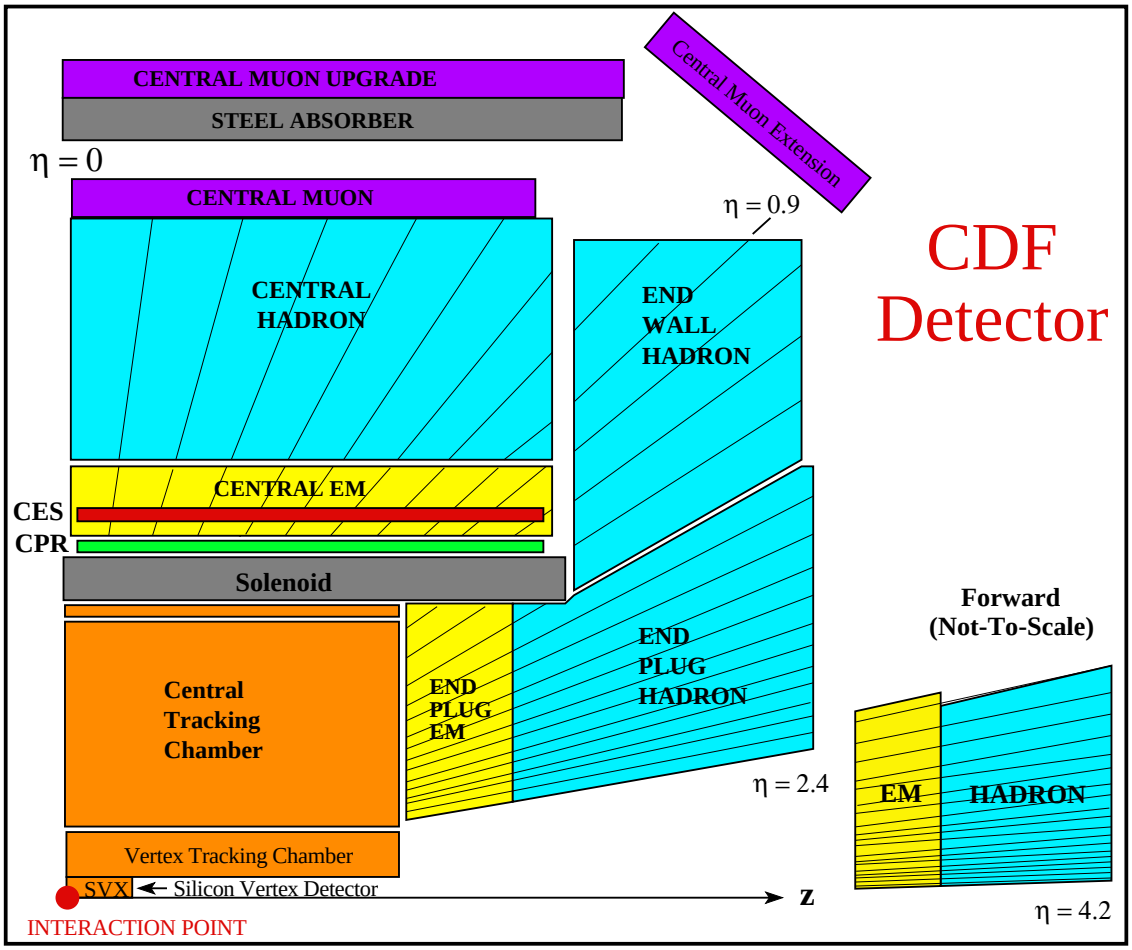

Figure 2.4: One quadrant of the CDF detector during Run I.

2.2.1 THE CENTRAL TRACKING CHAMBER (CTC)

The Central Tracking Chamber is a cylindrical wire drift chamber, 3.2 m in length [39]. It covers the radii between 277 mm and 1380 mm from the beamline. The 84 radial layers of sense wires are grouped in nine superlayers. 5 of the superlayers contain 12 layers of sense wires each, arranged parallel to the beamline and thus providing r–ϕ information. Between the five axial superlayers there are 4 stereo superlayers consisting of 6 sense wire layers each. The stereo angle alternates between +3° and -3° in successive stereo superlayers. The stereo layers add z–information to the particle tracks. The gas gain on the sense wires is controlled by potential wires alternating with the sense wires within the superlayers. Tracks with $|\eta| < 1.0$ pass through all nine superlayers.
The superlayers are divided azimuthally into drift cells so that the maximum drift distance is less than 40 mm, corresponding to a drift time of less than 800 ns. The voltage on the field wires is set to give a drift field of 1350 V/cm. Within the drift cells, the wires lie in a plane at an angle of 45° to the radial direction to compensate for the Lorentz angle due to the magnetic field. This arrangement also ensures that any radial track will pass close to at least one sense wire per superlayer. This is used by the Central Fast Tracker (CFT) which reconstructs high momentum tracks at trigger level. The arrangement of the superlayers and their drift cells can be seen in Figure 2.5. Each sense wire is attached to a preamplifier mounted on the CTC endplate. A amplifier–shaper–discriminator circuit produces a differential ECL pulse with a width equal to the signal's time over threshold. The pulse is then transmitted to time–to–digital converters (TDCs) which are able to read at least 8 hits per wire per event. The design drift distance resolution on each wire is 200 μm resulting in a momentum resolution of $\sigma_{P_T}/P_T \approx 2 \cdot 10^{-3} \cdot P_T$ [GeV/c]. The track reconstruction efficiency for tracks with transverse momenta above 0.6 GeV/c is better than 95% [40]. The resolution for discerning two tracks close together is approximately 5 mm.

2.2.2 THE SILICON VERTEX DETECTOR (SVX)

The silicon vertex detector (SVX) [35] is the detector system closest to the $p\bar{p}$ interaction point. It was the first silicon vertex detector to be operated at a hadron collider. The original device used during the 1992–93 running period was replaced by the SVX′ [36] for Run Ib.
Both devices use single-sided silicon sensors, 85 mm long and 300 μm thick, of n–type bulk with p^+ implants. The SVX silicon sensor strips were DC coupled to the readout electronics whereas SVX′ used AC coupled sensor technology for improved radiation hardness. SVX′ and SVX are basically similar in design. Unless specified, the term SVX will be used to refer to both devices.
The SVX consists of two identical, cylindrical units (barrels), each 25.5 cm long, with a 2.2 cm gap in between. Figure 2.6 shows one of the barrels. Each barrel

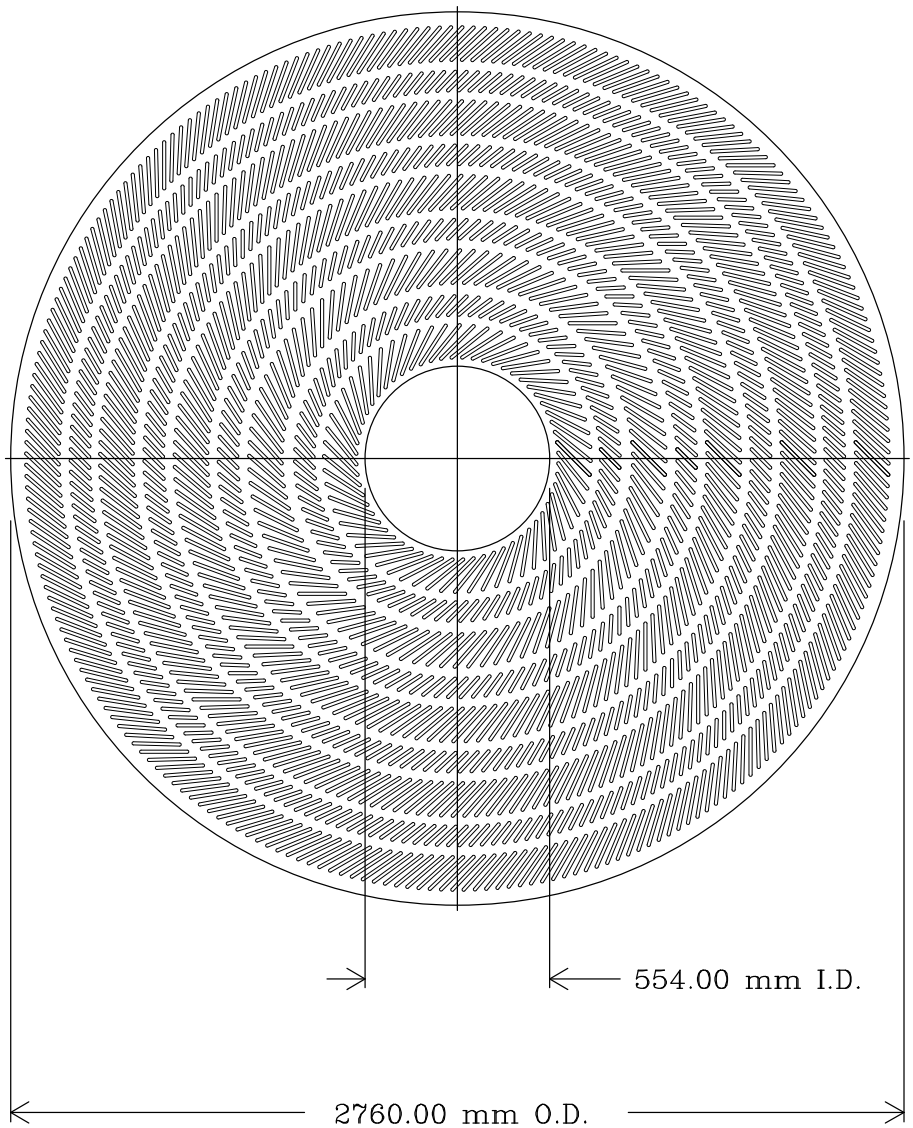

Figure 2.5: A CTC endplate, showing the wire feed-through slots for the cells in the nine superlayers [39].

consists of four concentric layers of silicon sensors with the strips parallel to the z-axis, thus providing only r-ϕ information. The four layers are located at distances between about 3 cm and 7.85 cm from the beamline. The strip pitch is 60 μm for the first three layers and 55 μm for layer 3. Each SVX layer consists of 12 ladders arranged in a 12–sided geometry. A 30° section in ϕ, consisting of four ladders in a radial line, is called a 'wedge'. A ladder is the basic mechanical and electrical unit of the SVX. It is composed of three silicon sensors wire-bonded end to end and supported by a Rohacell foam backing reinforced with carbon fiber strips. The aluminum readout strips of the sensors are bonded to readout chips located at the end of the ladder. These readout chips are mounted on an aluminum-nitride-substrate

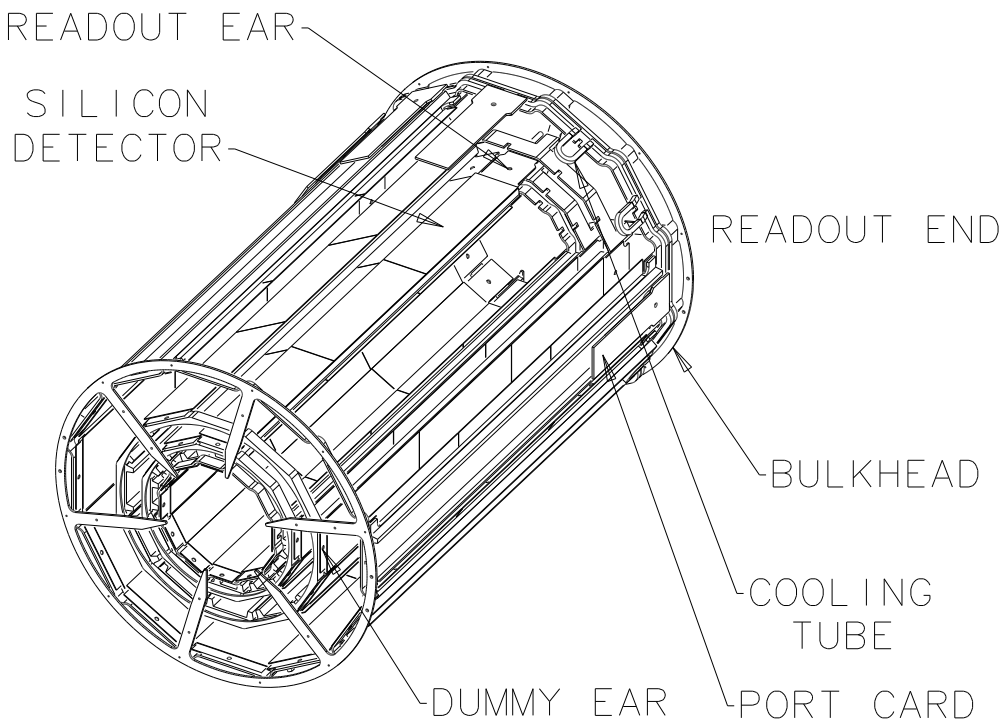

Figure 2.6: One of the two SVX barrels.

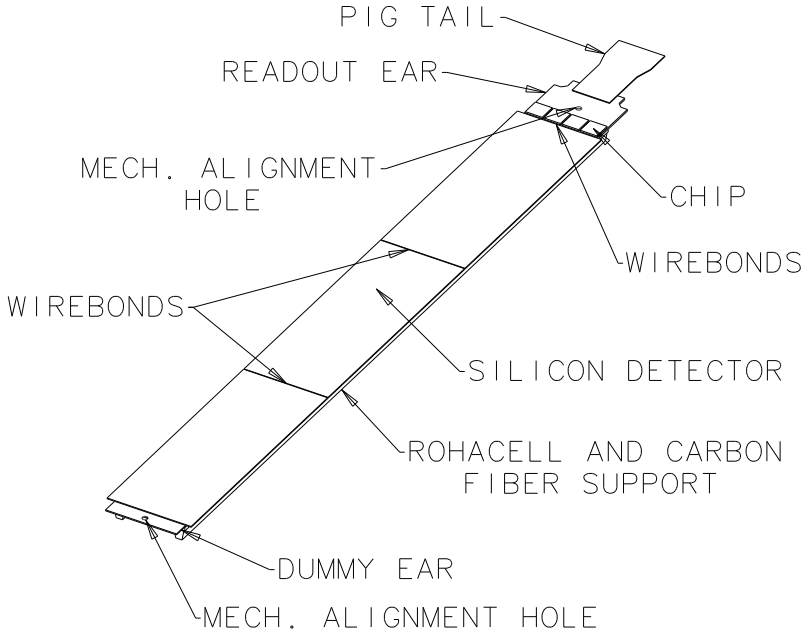

Figure 2.7: A SVX layer 2 ladder with 4 SVX readout chips.

hybrid circuit called the ear board. There are four sizes of ladders corresponding to the four radial layers. Layers 0–3 have 2, 3, 4 and 6 readout chips respectively. Each ladder is tilted at 3° to provide some overlap between adjacent wedges. However, on the innermost layer of the SVX no such overlap existed, causing a small ϕ gap in coverage. This was corrected in the SVX′ by moving the layer in to r = 2.86 cm and tilting it an extra 1.5°. A ladder for layer 2 is shown in figure 2.7.
The readout chip is a custom designed 128-channel CMOS device called the SVX IC [38]. Each channel consists of a charge integrating amplifier followed by a sample-and-hold and a threshold storage section. The chip supports data sparsification[8] which is needed to reduce the readout time and the amount of data to an acceptable level. The analog data is read out through a serial bus. The SVX ICs are connected to port cards mounted on the outer rim of the bulkheads. The port cards supply the operating voltage to the SVX chips and provide amplifiers and drivers for the analog serial bus. Each port card reads out one wedge and is connected to a digitizer module located in a FASTBUS[9] crate outside the CDF detector. The strip signals are digitized by 12 bit ADCs. There are a total of 46080 readout channels in the SVX. The total heat generated by the chips is approximately 100 W. This excessive heat is removed using chilled–water tubes which are in thermal contact with the beryllium bulkheads at the readout end.
Since the SVX is used as a high precision tracking device, its alignment is crucial. During assembly and mounting in the CDF detector, optical surveys were performed. Further alignment corrections are made to the SVX data offline using measured tracks. The SVX detector is not a standalone tracking system. SVX data is used to improve the impact parameter and momentum resolution of tracks reconstructed in the CTC. Individual SVX strips with charge signals are grouped to clusters of one or more strips. The cluster position resolution depends on the number of strips and averages 13 μm over all clusters [37]. Clusters in the SVX are matched to CTC tracks which are extrapolated into the region of the SVX. The combined CTC+SVX tracks have an impact parameter resolution of $(13 + 40/P_T)$ μm and a P_T resolution $\sigma_{P_T}/P_T \approx \sqrt{(0.9P_T)^2 + (6.6)^2} \cdot 10^{-3}$ where P_T is measured in units of GeV/c.

2.2.3 CALORIMETERS

The calorimeters of CDF are designed to measure the energy of particles and jets by fully absorbing all particles except muons and neutrinos. Electromagnetic and hadronic calorimeters are arranged in a tower geometry surrounding the tracking system. The central and endwall calorimeters cover a pseudorapidity range of $|\eta| < 1.3$ and the plug and forward calorimeters provide coverage in the pseudorapidity ranges $1.1 \leq |\eta| \leq 2.4$ and $2.4 \leq |\eta| \leq 4.2$, respectively (see Figure 2.4).
The central and endwall calorimeters have two halves, referred to as east and west arcs. Each half consists of 24 wedges covering 15° in ϕ and each wedge is subdivided

[8] Only channels above a programmed charge threshold and their nearest neighbors are read out.
[9] FASTBUS is a standardized (ANSI/IEEE STD 960-1986), modular data acquisition system. It provides a 32-bit address bus and asynchronous as well as synchronous (high speed) data transfer.

into 10 towers of 0.1 units in η. Figure 2.8 shows one of the wedges.

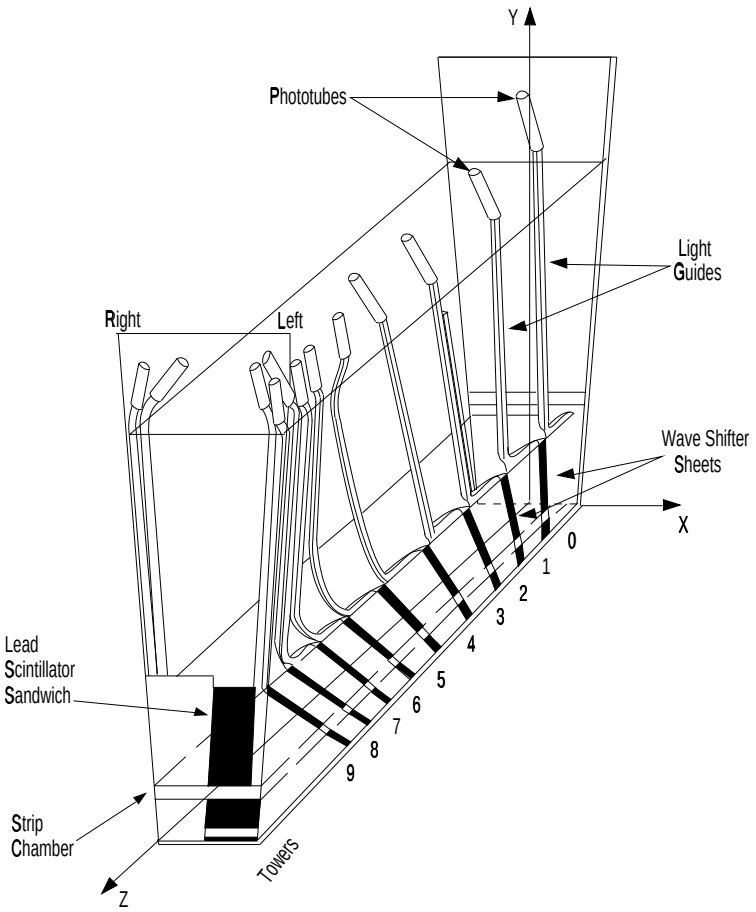

Figure 2.8: A wedge of the central calorimeter showing the ten towers in η. The lower part is the electromagnetic calorimeter and includes a strip chamber, the CES.

The calorimeters are sampling calorimeters. The active medium of the central and endwall calorimeters is scintillator, the absorber is lead in the electromagnetic calorimeter (CEM) and iron in the hadronic compartment (CHA).
Six radiation length (X_0) deep in the CEM is the central electromagnetic shower (CES) chamber, a set of proportional strip and wire chambers. It measures the position of electromagnetic showers at the shower maximum. The central pre-radiator (CPR) is another set of proportional chambers between the solenoid and the CEM. The CPR samples electromagnetic showers that begin in the solenoid material (1.1 X_0) and helps to separate single photons from multiple photons and electrons.
In high $|\eta|$ regions of the detector, radiation exposure becomes an issue. Also a finer transverse segmentation is needed in order to achieve the same position resolution as in the central region. As a result, the plug and forward calorimeters use drift chambers with a 1:1 mixture of argon/ethane as active medium. The absorber material is the same than in the central calorimeter. Table 2.1 summarizes some properties of the calorimeter systems.

Calorimeter:	Central EM	Central Hadron	Endwall Hadron	Plug EM	Plug Hadron	Forward EM	Forward Hadron
$\|\eta\|$ coverage	0 - 1.1	0 - 0.9	0.7 - 1.3	1.1 - 2.4	1.3 - 2.4	2.2 - 4.2	2.3 - 4.2
Tower size $\Delta\eta \times \Delta\phi$	$0.1 \times 15°$	$0.1 \times 15°$	$0.1 \times 15°$	$0.09 \times 5°$	$0.09 \times 5°$	$0.1 \times 5°$	$0.1 \times 5°$
Absorber thickness	Pb 3.2 mm	Fe 25 mm	Fe 51 mm	Pb 2.7 mm	Fe 51 mm	Pb/Sb 4.8 mm	Fe 51 mm
No. of layers	31	32	15	34	20	30	27
Total thickness	18 X_0	4.5 λ_I	4.5 λ_I	19 X_0	5.7 λ_I	25 X_0	7.7 λ_I
σ_E/E at 50 GeV	2%	11%	14%	4%	20%	4%	20%

Table 2.1: Properties of the various calorimeters. The total thickness is quoted in radiation length for EM calorimeters and nuclear interaction length for hadronic calorimeters.

2.2.4 MUON DETECTORS

Muons are detected by drift chambers outside the calorimeters. The calorimeters and the solenoid coil provide the necessary shielding and absorb most of the other charged particles. The coverage of the CDF central muon system is shown in Figure 2.9. It consists of three detectors: the Central Muon Chambers (CMU), the Central Muon Upgrade (CMP) and the Central Muon Extension (CMX). The CMU [41] is located outside the central calorimeter and extends to $|\eta| \simeq 0.6$. CMP and CMX were added in 1992 [42]. The CMP covers the same region as the CMU but is located behind an additional 60 cm steel absorber (see Fig. 2.4). The CMX extends the coverage to $|\eta| \simeq 1.0$ but has two major gaps in ϕ, one of 90° due to the collision hall floor and one of 20° at the top, where the main ring and parts of the solenoid cryostat are located.

All central muon systems consist of several layers of single-wire drift cells with the wires oriented parallel to the beam[10]. CMX and CMP also include scintillator planes which provide precise timing information used in the trigger.

[10]The CMX wires are at an angle to the beamline but are also oriented to measure the $r - \phi$ coordinate.

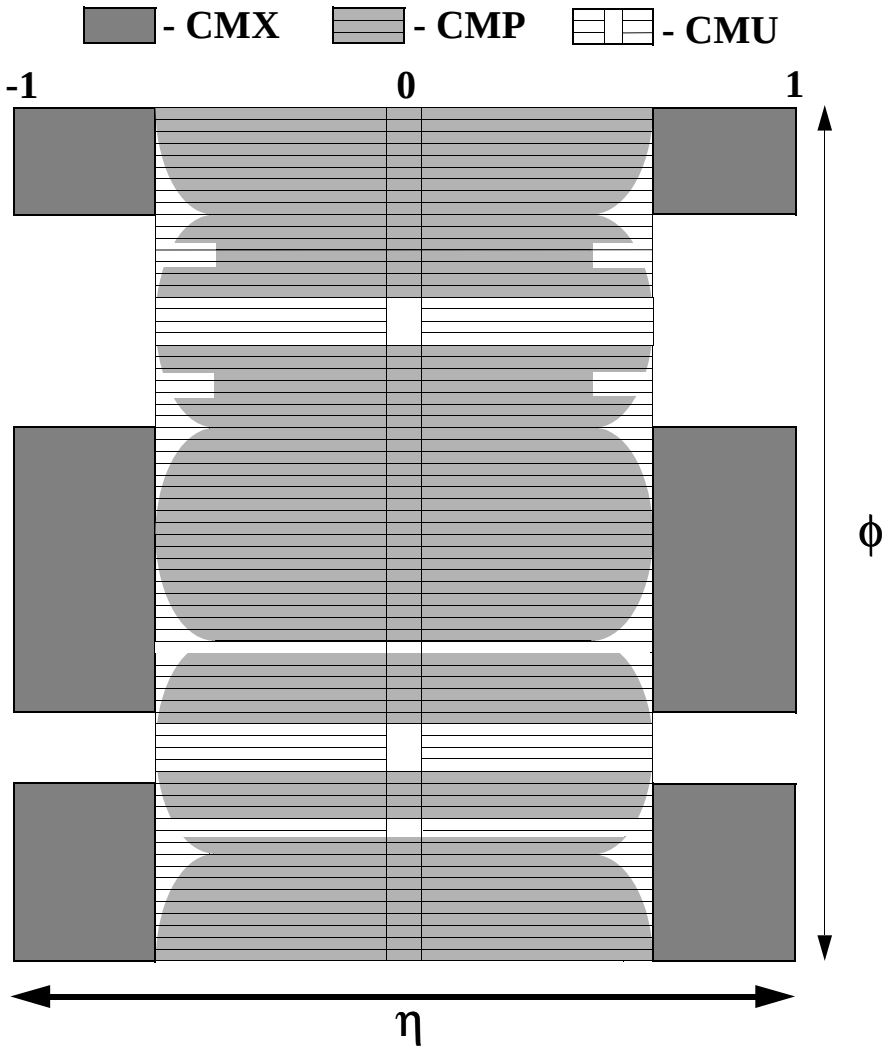

Figure 2.9: The $\eta - \phi$ coverage of the CDF central muon systems, CMU, CMP and CMX. $\phi = 0...2\ \pi$.

All drift cells have 50 μm stainless steel sense wires held at 3150 V. The drift gas is a 1:1 mixture of argon/ethane with $\approx$ 1% ethanol. The maximum drift time is $\approx$ 700 ns. The resolution is 250 μm in azimuth and 1.2 mm in z. The z–coordinate is measured using the charge division method by reading out both sides of the resistive wires.

2.2.5 THE TRIGGER SYSTEM

The beam crossing rate of the Tevatron during Run I was about 300 kHz. Due to the high $p\bar{p}$ cross section, most bunch crossings contained at least one $p\bar{p}$ interaction. The maximum rate at which events can be written to tape is less than 10 Hz. CDF utilizes a three-level trigger system to select data of interest and to reduce the amount of data to a reasonable volume. The 1st, 2nd and 3rd trigger levels typically accept events with a rate of 1 in 600, 1 in 100 and 1 in 4 respectively.
The Level 1 trigger is a hardware trigger which checks for signals in the calorimeter towers or muon chambers. A signal is defined as an energy deposit at or above some threshold. The decision whether or not to accept an event is made within 3.5 μs, the time between successive interactions, thus the Level 1 trigger works deadtime-less. If an event passes Level 1, further data acquisition stops and the event is processed by the Level 2 trigger.
The Level 2 trigger is also implemented in hardware but is much more sophisticated than Level 1. Transverse-energy clusters are formed of adjacent calorimeter towers if the tower energies exceed a certain threshold. The Central Fast Track (CFT) track processor [43] reconstructs tracks with $P_t \gtrsim 2$ GeV/c in the CTC. It uses $r-\phi$ information from the axial superlayers only. Each CFT track to is then extrapolated to the calorimeter and muon chambers and matched to clusters in these detectors. Analyzing an event takes 20 μs. The bunch crossings that occur during this time are lost. When an event passes the Level 2 trigger, the information from the individual detector subsystems is read out and combined together by the Event Builder. Then the data is passed to the Level 3 trigger.
The Level 3 [44] trigger is a software trigger running on Silicon Graphics CPUs[11]. The CPUs run basically the same Fortran code that is used for the offline event reconstruction. However, SVX tracking is not included in the Level 3 trigger software. Physics objects such as tracks, jets and lepton candidates are reconstructed. A wide variety of requirements can be imposed for events passing the Level 3 trigger. If an event passes Level 3, it is written to tape. Once an event is stored on tape, it is later possible to reprocess it to apply corrections and calibrations and analyze it further offline. Events containing certain physics objects such as dimuons in the J/ψ invariant mass region are already separated from the rest of the data. These data streams ("Express stream" or "Stream A") allow an analysis of the data a few hours after the data taking.

[11] CPU is an acronym for 'central processing unit'.

Chapter 3

Data Samples

The data used in this analysis were recorded using the CDF detector during Run I of the Tevatron, in the years 1992 through 1996, at $\sqrt{s}$ =1.8 TeV. Run I comprised three separate data taking periods: Ia, Ib and Ic. During Run Ia, CDF collected an integrated luminosity of $\approx$ 19.5 pb^{-1} [45]. After Run Ia, the detector underwent several improvements. As described in Chapter 2, the SVX was replaced by the SVX$'$. New trigger requirements were implemented and the data acquisition system was significantly improved. Run Ib started January 1994 and lasted until July 1995. CDF recorded an integrated luminosity of $\approx$ 86.5 pb^{-1} during this period. Two more runs, Run Ic and a run at $\sqrt{s}$ =630 GeV lasted until February 1996. During Run Ic, CDF collected additional $\approx$ 7.8 pb^{-1}. The data samples used for this measurement thus correspond to a total integrated luminosity of $\approx$ 113.8 pb^{-1}.

This study is done with fully reconstructed B meson decays with J/ψ and $\psi(2S)$ final states. The charmonium states are identified via the decay into lepton–/anti–lepton pairs. During Run I, CDF had a low P_T dimuon trigger but no low P_T dielectron[1] trigger in the J/ψ and $\psi(2S)$ mass regions. To find $J/\psi \to e^+e^-$ decays, the "inclusive electron" data sample is analyzed.

3.1 The Dimuon Dataset

The dimuon trigger is configured to record pairs of muons in the CMU and CMX detectors. Forward muon triggers also exist but are not used in this analysis. To maximize the acceptance for J/ψ and $\psi(2S)$ decays, the P_T threshold for the muons should be as low as possible but this goal is limited by several factors: Because of ionization energy losses, in the central calorimeter and solenoid coil, only muons with $P_T \gtrsim 1.4$ GeV/c can reach the CMU. The second limiting factor is the DAQ bandwidth. Only a limited fraction of the bandwidth can reasonably be devoted to dimuon events. Muon signals and backgrounds both increase significantly at lower P_T. As a result, the dimuon triggers typically record muons with $P_T > 2$ GeV/c.

[1] The term 'electron' is used for both, the electron and its anti–particle, the positron.

Track segments in the muon drift chambers are referred to "stubs" to distinguish them from CTC tracks. The Level 1 dimuon trigger requires the presence of two stubs in the CMU or CMX at the time of the beam crossing. Further, the two stubs must be located in noncontiguous modules. That is, at least one muon module lacking a muon stub must have resided between the two modules where stubs are observed. Dimuon triggers are possible with two CMU stubs, two CMX stubs or one of each.
At Level 2, each CFT track is extrapolated to the muon chambers using a lookup table. If a track matches a module which fired at Level 1, it is recorded as a muon candidate. There are different Level 2 dimuon triggers, all requiring two muon stubs in the CMU and/or CMX and one or two CFT tracks. These triggers changed substantially between runs. In Run Ia, one CMU stub with an associated CFT track and a second Level 1 CMU stub is required. During Run Ib, three triggers are relevant to this analysis. One of them requires two CMU stubs, each with an associated CFT track. The second trigger also allows one CMX muon stub together with a CMU stub with associated CFT track. The third trigger is specialized for muon pairs which are close in azimuth. Also, the P_T cuts on the two muon candidates are quite different. During Run Ia the values were $\approx$ 2.8 GeV/c for the first muon and $\approx$ 1.6 GeV/c for the second muon, whereas in Run Ib, the thresholds were $\approx$ 2.0 GeV/c for both muon candidates.
The third level dimuon trigger uses three-dimensional tracking information from the CTC. In Run Ia the trigger required two muon candidates with opposite charge and an invariant mass between 2.8 and 3.4 GeV/c^2. During Run Ib the mass window was 2.7 – 4.1 GeV/c^2 and there was no opposite sign charge requirement. The Level 3 trigger also performs precise matching between CTC tracks and muon stubs. The tracks are extrapolated to the position of the muon chambers and required to match the muon stub positions in both, the $r-\phi$ plane and the z direction. The match was required to be within 4 standard deviations (σ) of the combined multiple scattering and measurement uncertainties during Run Ia and 3σ during Run Ib respectively.

3.2 THE INCLUSIVE ELECTRON DATASET

The inclusive electron dataset is a data sample collected with several different triggers requiring an isolated energy deposition in the central electromagnetic calorimeter (CEM) and a CTC track pointing at it. These triggers have various different requirements for the transverse momentum (P_T) of the tracks and the energy deposition (E_T) in the calorimeter. The Level 3 trigger with the lowest thresholds used during Run Ia requires a P_T of at least 4 GeV/c in combination with an energy deposit of $E_T > 6$ GeV in the CEM. During Run Ib, the lowest thresholds were $P_T > 5$ GeV/c and $E_T > 5$ GeV. Mainly, triggers with higher thresholds were used. Typical requirements are P_T >6 GeV/c and $E_T > 8$ GeV or $E_T > 9$ GeV. Some triggers also require a signal in the central electromagnetic shower chamber whose lateral profile resembles those typical for electron showers.

3.3 Data Storage

The event data written to tape by the data acquisition system is processed again by the 'production and splitting' computer farm. In this step, run-dependent calibration and alignment corrections are applied and a more sophisticated track reconstruction takes place. An example are the CTC drift constants which vary from run to run and are available after the run only. Events are split into physics categories. Examples would be dimuon events in the J/ψ and $\psi(2S)$ mass regions or W-candidates. The events are written in the YBOS [46] format in which physics objects are stored sequentially in indexed banks. Examples for such objects in YBOS banks would be muon candidates, primary vertex objects or CTC tracks, including SVX information if available.
These reprocessed data are stored on hard disk or tape and are accessible from the main offline computer system (cdfsga) for further processing. The typical size of an event is approximately 15 kB. The data samples used for this analysis are listed in appendix A.

Chapter 4

Reconstruction of B Meson Decays and Lifetime Measurement

In this section the third principal stage of the data selection process (after the trigger and the 'production' processing as described before), the application of analysis specific algorithms is described. In particular the step by step reconstruction of $B^{\pm}$ and B^0 mesons and the computation of their lifetime is discussed. The B meson reconstruction software is written in FORTRAN and consists of several modules, each performing a specific part of the reconstruction process. These modules work within the CDF Run I Analysis Control [48] software framework and are easily configurable, e.g. cut values on different quantities can be changed and some modules can be reconfigured to search for a different particle without recompiling them. Some of the modules create their own YBOS banks[1] to store results and add them to the event record. Specifically, for this analysis the following modules were developed and used:

GETLEP[2]	: this module finds trigger electrons.
PSIEE	: identifies low P_T ("soft") electron tracks and pairs them with electron candidates provided by GETLEP.
GETDIMU	: applies quality requirements on muon candidates and forms pairs of muons in a specific invariant mass region.
MAKEJPSI	: this module takes the information from PSIEE or GETDIMU and reconstructs J/ψ or $\psi(2S)$ decays into leptons.
GETPSI2S	: checks, if the J/ψ candidates reconstructed by MAKEJPSI are produced in the decay $\psi(2S) \to J/\psi\ \pi^+\pi^-$.
GETKAON	: this module seeks for the decays $K^0_S \to \pi^+\pi^-$, $K^{*\pm} \to K^{\pm}\pi^{\mp}$, $\phi \to K^+K^-$ and $\Lambda \to p\ \pi^-$.

[1] These are DILP banks to store dilepton pairs, PSIS banks for charmonium decays and KAON banks for K^0_S, K^{*0}, ϕ and Λ decays.

[2] GETLEP was developed by Hans Wenzel.

MAKEB	: selects $B^{\pm}$ meson candidates decaying into J/ψ and $\psi(2S)$ final states.
MKB0	: reconstructs B^0 meson decays into J/ψ and $\psi(2S)$ final states.
MNPSIS	: monitors PSIS banks (e.g. for debugging purposes).
MNKAON	: monitors KAON banks.

In the following the successive steps of the reconstruction of B mesons are described in more detail. As a general strategy, the cuts applied on different quantities are loose in order to collect as many B meson candidates as possible. Cuts on the transverse momentum of the B meson and the kaon candidates are applied later and differ for the different B decay modes. They are not listed in this chapter. Since it is essential for this analysis to know the beamline position and slope, only data from stores[3] for which this information is available are at all used.

4.1 Track Quality Cuts

To ensure that the B vertices are well measured, certain quality requirements are applied on all tracks considered to form B vertex candidates. These requirements are :
– a good 3-D fit in the CTC.
– at least 2 CTC axial superlayers with a minimum of 4 hits.
– at least 2 CTC stereo superlayers with a minimum of 2 hits.
If a track is measured in at least two layers of the SVX, the combined CTC/SVX fit is used for the reconstruction of B vertices. Otherwise, the CTC-only fit is used. Requirements for the leptons originating from the charmonium decays are described below.

4.2 Reconstruction of J/ψ and $\psi(2S)$ Decays

The four charmonium decay modes used in this study are $J/\psi \rightarrow \mu^+\mu^-$, $J/\psi \rightarrow e^+e^-$, $\psi(2S) \rightarrow \mu^+\mu^-$ and $\psi(2S) \rightarrow J/\psi\ \pi^+\pi^-$ where in the latter case the J/ψ meson is reconstructed in its dimuon mode.

4.2.1 The $J/\psi \rightarrow \mu^+\mu^-$ and $\psi(2S) \rightarrow \mu^+\mu^-$ modes

The first step of the ψ (J/ψ or $\psi(2S)$) reconstruction is to search for muon candidates. This is done by the module GETDIMU. Muons detected in the CMU, CMP or CMX muon detectors are accepted as well as muon candidates which hit more than one muon system. Rejected are only candidates which hit CMP and CMX since

[3]'store' denotes here a 'collider fill', an uninterrupted running period with the same set of proton– and antiproton bunches, which typically lasts for several hours.

this combination is geometrically impossible (see Figure 2.4). The muon tracks in the CTC are extrapolated to the muon chambers and the position difference between the track and the muon stub as well as its uncertainty caused by multiple scattering and energy loss are calculated. The match between the muon stub and the CTC track is required to have a χ^2 less than 9 and 12 (for one degree of freedom) in ϕ and z directions respectively. Minimum ionizing particles are expected to deposit ≈ 0.4 GeV in the hadronic calorimeter. Therefore, for muon candidates, an energy deposit of at least 0.1 GeV associated with the muon track is required. Muon candidate tracks must have been reconstructed in both the CTC and SVX. The muons must have clusters matched to their tracks in at least three of four possible layers of the SVX.

Pairs of oppositely charged muon candidates are formed and their invariant mass is calculated. At least one of the muons of the pair is required to have a $P_T > 2.5$ GeV/c for Run Ia data and $P_T > 2.0$ GeV/c for Run Ib and Ic data. Pairs with a mass of $\pm$ 300 MeV/c^2 around the world average J/ψ mass of 3.097 GeV/c^2 [14] and pairs with a mass of $\pm$ 375 MeV/c^2 around the $\psi(2S)$ mass of 3.686 GeV/c^2 are passed to the MAKEJPSI module. Here a least-squares fit to the muon pair is performed and a vertex constraint [49] is applied[4]. The χ^2 propability of this vertex fit is required to be at least 1%. Vertices which pass this requirement and have a mass of $\pm$ 80 MeV/c^2 around the peak mass and a transverse momentum of at least 1.5 GeV/c are considered J/ψ or $\psi(2S)$ candidates and are passed to the B meson reconstruction modules. The mass distributions of the reconstructed di-muon vertices in the J/ψ and $\psi(2S)$ mass regions are shown in Figures 4.1 and 4.2.

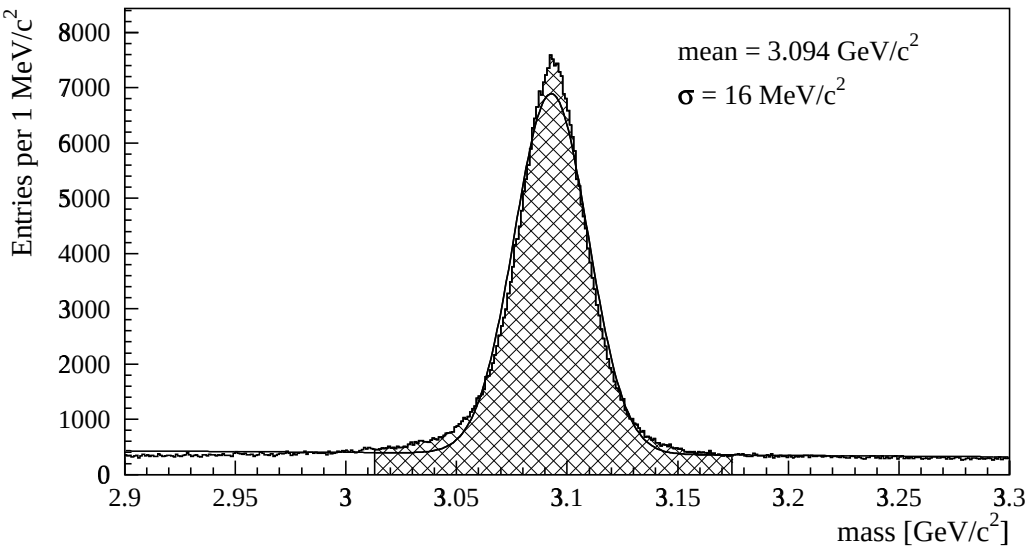

Figure 4.1: The J/ψ mass distribution. The hatched area shows the signal region which contains $\approx$ 280000 signal candidates over a background of $\approx$ 50000 events.

[4]The track parameters are adjusted within errors so that the two muons originate from a common point in space.

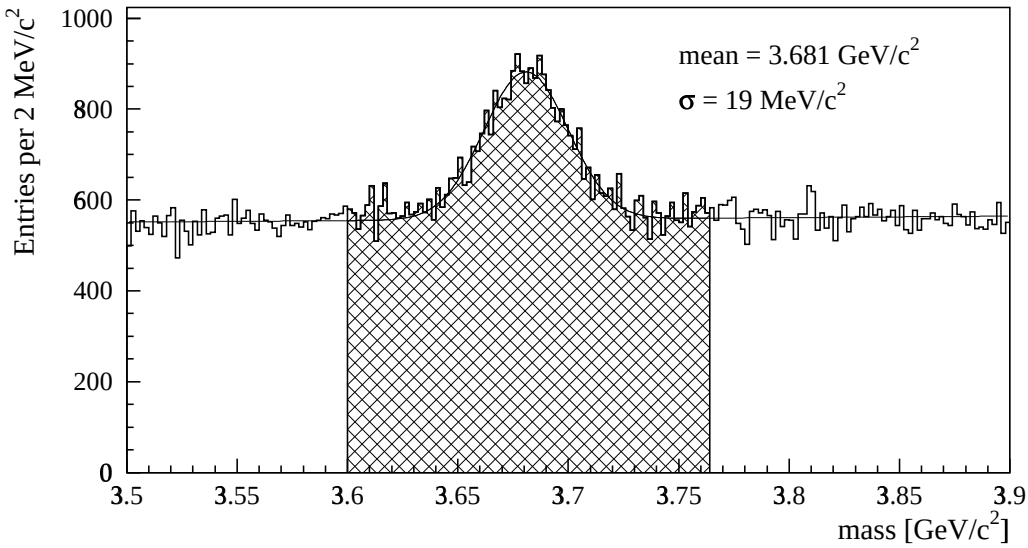

Figure 4.2: The $\psi(2S) \to \mu^+\mu^-$ mass distribution. The hatched area shows the signal region which contains $\approx$ 7800 signal candidates over a background of $\approx$ 44000 events.

4.2.2 The Decay $J/\psi \to e^+e^-$

As mentioned above, no low-P_T dielectron trigger was implemented during Run I. Only an "inclusive electron" data sample is available in which the trigger electrons have a rather high transverse momentum of $\approx$ 10 GeV/c on average (Figure 4.3 (b)). The "standard" CDF electron reconstruction algorithm was designed for high P_T electrons, e.g. from W-decays. For electron candidates found by this algorithm a so-called ELES bank is created. The numerous implicit isolation requirements that go into the making of ELES banks render such banks inefficient for non-isolated, low P_T electrons that are expected from b decays. The efficiency for the making of ELES banks is shown in Figure 4.4. Consequently not only ELES electrons are considered as second (non-trigger) electrons for the J/ψ reconstruction, but also a track–based algorithm to identify low P_T ("soft") electrons is utilized. This algorithm uses information from the Central Strip Chamber (CES), the Central Pre–Radiator (CPR) and the CTC. It is applied to tracks with a minimum transverse momentum of 1 GeV/c. The steps of this algorithm are listed below:

1. Extrapolate tracks into the fiducial volume of the CPR and CES.

2. Impose matching cuts between the extrapolated CTC track and CES strip and wire clusters. The matching requirements are choosen relatively loose: $\Delta x < 4$ cm and $\Delta z < 6$ cm.

3. Cut on the quotient of the energy deposits in the hadronic and the electromagnetic compartment of the calorimeter since electrons deposit their whole energy in the electromagnetic calorimeter: $\mathrm{E}_{Had}/\mathrm{E}_{EM} < 0.125$.

4. Require the ionization loss in the CTC to be consistent with that of an electron.

5. Electrons start electromagnetic showers already in the solenoid. Therefore a minimum charge deposition in the CPR corresponding to several minimum ionizing particles is required.

6. Require the transversal shower shape measured in the CES to be consistent with that of an electron. This is imposed via a cut on a cluster χ^2 which is calculated by comparing the fractional pulse heigths with those determined in an electron test beam.

Tracks fulfilling all requirements are considered 'soft electron' candidates. The trigger electron is paired with ELES electrons or 'soft electrons'. Pairs with an invariant mass between 2.0 and 4.0 GeV/c^2 are passed to the MAKEJPSI module where a vertex constrained fit is applied. Figure 4.3 (a) shows the mass distribution of dielectron vertices after the vertex fit. The energy loss of particles in matter due to bremsstrahlung is proportional to $1/m^2_{particle}$ and thus for electrons substantially

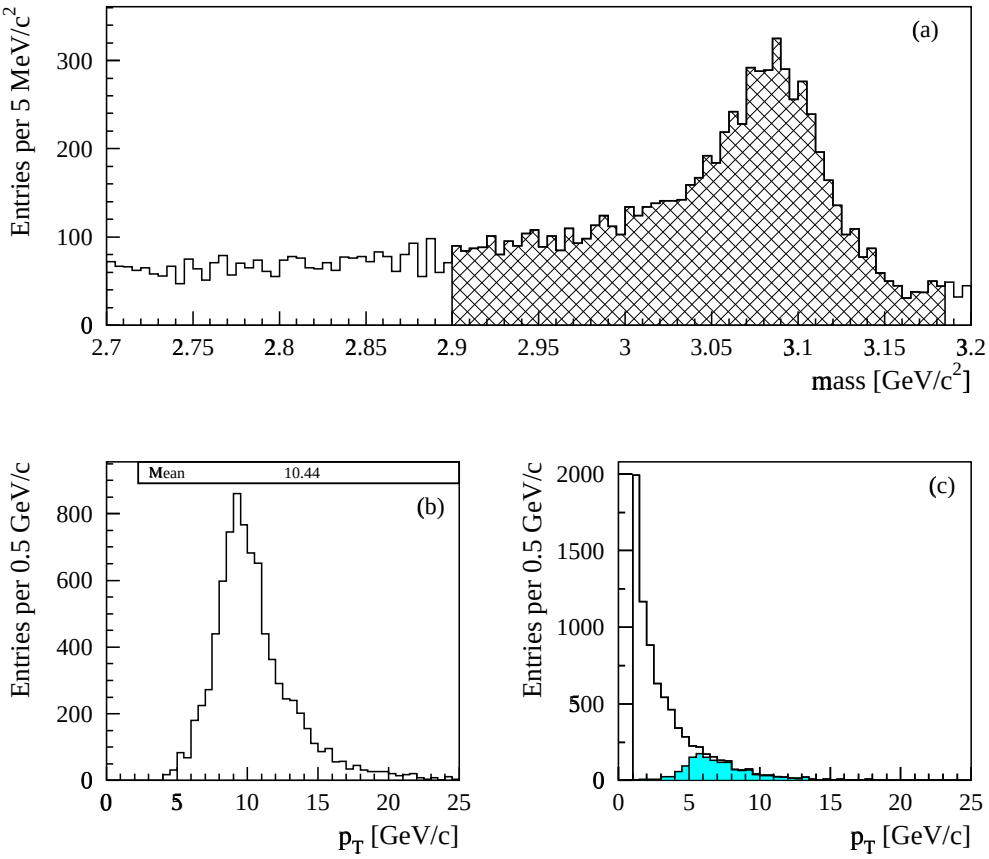

Figure 4.3: (a) The dielectron mass spectrum after a vertex constrained fit. The hatched area is the signal region. Below, the transverse momenta of electrons mainly originating from J/ψ decays are shown. The left picture (b) shows the P_T distribution of the trigger electron, the right picture (c) of the second ("soft") electron. The P_T distribution of the electrons which have a dedicated ELES bank is the shaded area in picture (c).

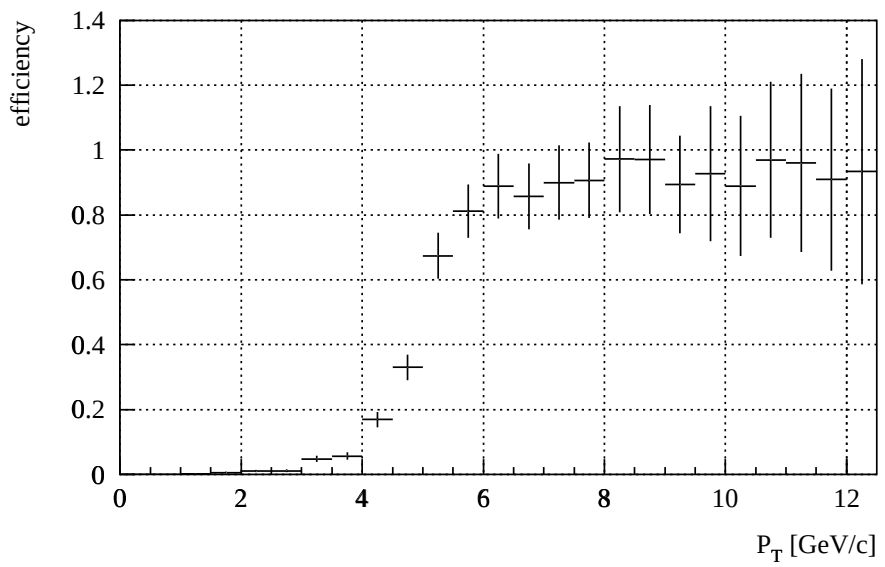

Figure 4.4: The ELES efficiency as a function of the electron P_T. The histogram is obtained by dividing the shaded and non-shaded histograms 4.3 (c).

higher than for muons. Compared to the $J/\psi \to \mu^+\mu^-$ mass distribution (Figure 4.1) the low mass tail in the $J/\psi \to e^+e^-$ mass distribution caused by bremsstrahlung is clearly visible. However, the tail seems longer than expected due to background from sequential semileptonic B decays, e.g. $B^+ \to \bar{D}^0 e^+ \nu_e$, $\bar{D}^0 \to K^+ e^- \bar{\nu_e}$, whose branching ratios are in the order of 10 times higher than that of the charmonium modes. The shape of this background can be seen in Figure 4.5.

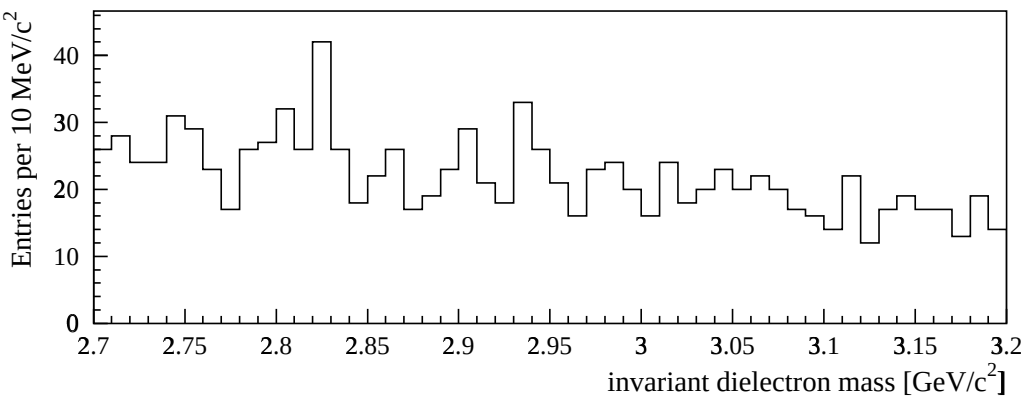

Figure 4.5: The shape of the background in the dielectron mass spectrum 4.3 (a) caused by $B^+ \to \bar{D}^0 e^+ \nu_e$, $\bar{D}^0 \to K^+ e^- \bar{\nu_e}$ decays (Monte Carlo generated). This histogram is not scaled to 4.3 (a).

4.2.3 THE CASCADE DECAY $\psi(2S) \to J/\psi\ \pi^+\pi^-$

When a J/ψ candidate is found in an event, the module GETPSI2S searches for the decay of a $\psi(2S)$ into the J/ψ and two pions. The algorithm looks for pairs of oppositely charged tracks and assigns the world average $\pi^\pm$ mass of 139.57 MeV/c^2 to them. If the invariant mass of the pair is < 610 MeV/c^2, the two tracks are combined with the J/ψ candidate and a vertex constrained fit of all 4 tracks is performed where the two muons from the J/ψ decay are mass constrained[5] [49] to the world average J/ψ mass. The upper mass limit for the pion pair corresponds to the maximum kinematically allowed di-pion invariant mass, defined by the $\psi(2S) - J/\psi$ mass difference in consideration of measurement uncertainties. The χ^2 probability of the 4-track vertex fit is required to be $> 0.1\%$ and the transverse momentum of the vertex is required to be > 1.5 GeV/c. Vertices which fulfil these requirements and have an invariant mass of $\pm$ 24 MeV/c^2 around the peak mass are regarded as $\psi(2S)$ candidates and stored for further processing by the B meson reconstruction modules. The mass distribution of the reconstructed 4-track vertices is shown in Figure 4.6.

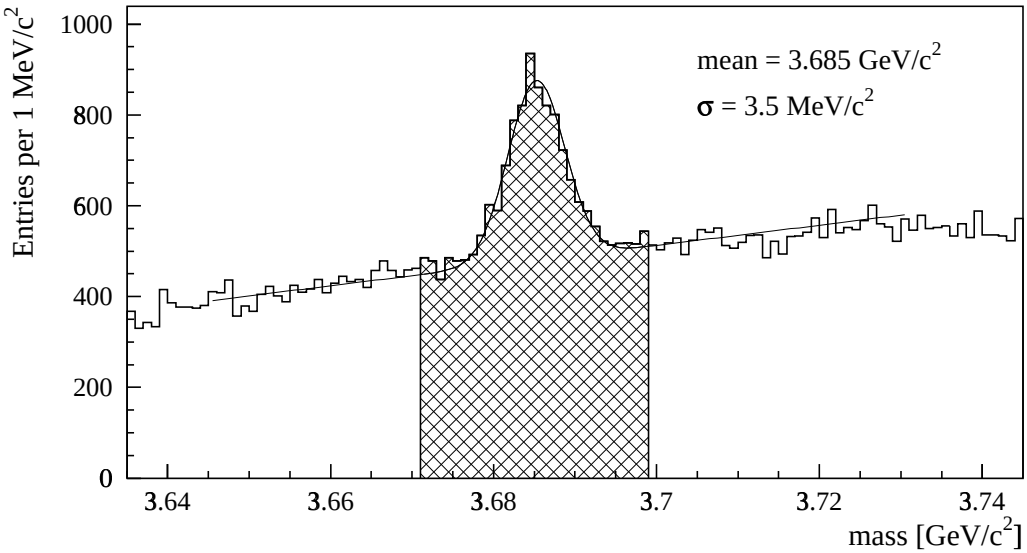

Figure 4.6: The $\psi(2S) \to J/\psi\ \pi^+\pi^-$ mass distribution. The hatched area is the signal region. A fit of a Gaussian+linear background yields 3466 $\pm$ 188 $\psi(2S)$ candidates.

4.3 RECONSTRUCTION OF KAON DECAYS

Decays of K^0_S and $K^*(892)^0$ are searched for within the J/ψ and $\psi(2S)$ samples. These searches are performed by the GETKAON module.

[5]The track parameters are adjusted within errors so that the $\mu^+\mu^-$ invariant mass is equal to the J/ψ mass.

4.3.1 K_S^0 $(\overline{K_S^0})$ $\rightarrow \pi^+\pi^-$

The K_S^0 candidates are found by matching pairs of oppositely charged tracks, assumed to be pions. A vertex constrained fit of the track pair is done. Due to the long lifetime of the K_S^0 mesons of $\approx 0.89 \times 10^{-10} s$ [14], most of the K_S^0 decay outside the SVX detector. Nevertheless, in many cases SVX information is available for one or both pion candidate tracks. Since there is a risk that wrong SVX hit clusters are attached to those CTC tracks, the SVX information is not used for the K_S^0 reconstruction. No P_T cut is applied on the pion candidate tracks. To reduce background, the K_S^0 candidates are required to travel a significant distance $L_{xy} > 3\ \sigma_{Lxy}$. The quantity $L_{xy} = (\vec{X} \cdot \vec{P_T^B})/|\vec{P_T^B}|$ is 2-D flight distance, where $\vec{X}$ is the vector pointing from the production vertex to the decay vertex. σ_{Lxy} is the measurement uncertainty of L_{xy}.[6]
Figure 4.7 shows the invariant mass distribution of the pion pairs after the vertex fit. The signal region is defined as the region $\pm$ 25 MeV/c^2 around the peak mass of 497.5 MeV/c^2. K_S^0 candidates with a mass within these boundaries are passed to the B meson reconstruction modules for further processing.

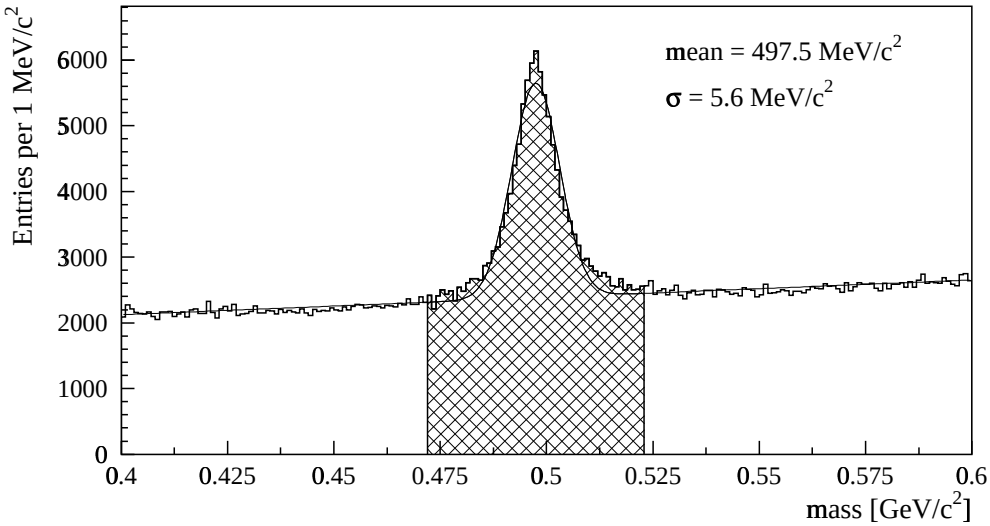

Figure 4.7: Approximately 50000 $K_S^0 \rightarrow \pi^+\pi^-$ are found within the $J/\psi \rightarrow \mu^+\mu^-$ sample. The hatched signal region also contains about 115000 background entries.

4.3.2 $K^*(892)^0$ $(\overline{K^*(892)^0})$ $\rightarrow K^\pm\pi^\mp$

K^{*0} candidates are reconstructed by considering all oppositely charged track pairs which have a distance in z of less than 5 cm at their point of minimum approach to the origin. For each pair of tracks considered, both mass assignment hypotheses, $K^+\pi^-$ and π^+K^- are initially retained. Further, cuts on the transverse momentum of the tracks are applied to reduce combinatorial background. For the tracks with

[6]The calculation of L_{xy} and σ_{Lxy} is explained in more detail in 4.7.2

kaon and pion mass assignments, $P_T(K) > 800$ MeV/c and $P_T(\pi) > 400$ MeV/c are required, respectively. A vertex constrained fit of the two tracks is then performed and the χ^2 probability of this fit is required to be $> 0.1\%$. Vertices with an invariant mass of $\pm$ 120 MeV/c^2 around the world average K^{*0} mass of 896.1 MeV/c^2 [14] are considered K^{*0} candidates and are further processed by the B^0 reconstruction module. The relatively wide mass range of 240 MeV/c^2 is necessary due to the natural width of the $K^*(892)^0$ resonance of 50.7 MeV/c^2 [14].

4.4 B Candidate Selection

The B meson reconstruction modules MAKEB (for charged B mesons) and MKB0 (for neutral B mesons) combine J/ψ or $\psi(2S)$ candidates with kaon candidates and/or tracks. Two basic topologies of B meson decays are distinguished: with and without a tertiary K^0_S decay vertex. These two topologies are shown in Figures 4.8 and 4.9.
For the decays $B^\pm \to \psi\ K^\pm$ ($\psi = J/\psi$ or $\psi(2S)$), charged tracks assumed to be a $K^\pm$ are combined with the ψ candidate. All tracks are fitted to form a common B vertex. A mass constraint on the ψ is applied for all charmonium decays, except $J/\psi \to e^+\ e^-$ [7]. Due to bremsstrahlung losses of the electron and positron in $J/\psi \to e^+\ e^-$ final states, the reconstructed B meson mass is lower than the true mass. The B mass is corrected by adding the difference of the true and reconstructed J/ψ masses. The decay $B^\pm \to J/\psi\ K^{*\pm}$ is reconstructed by combining a charged track assumed to be a $\pi^\pm$ with the ψ candidate. In addition, a K^0_S candidate is required in the event whose momentum points back in 3 dimensions to the B vertex (see Figure 4.9). Both vertices are fitted simultaneously and mass constraints on the ψ and the K^0_S are applied. The reconstruction of $B^0 \to J/\psi\ K^{*0}$ is again rather simple. All four tracks, the ψ legs and the $K^\pm$ and $\pi^\mp$ candidate tracks from the K^{*0} decay are vertex constrained to the same B vertex. The ψ is also mass constrained. $B^0 \to \psi\ K^0_S$ decays are reconstructed by requiring a K^0_S pointing back to the ψ vertex. Both vertices are then fitted simultaneously with mass constraints on the ψ and the K^0_S. In addition, to reduce background, the B momentum is required to point back to the beam. However, a beam pointing constraint can bias the lifetime measurement since the efficiency of such a constraint could depend on the distance of the B vertex to the beam. Also, the vertex position may be shifted in the vertex fit. Thus, the original ψ vertex is used to calculate the decay length of the B meson. A possible lifetime bias is determined with Monte Carlo generated B^0 decays. The results of this study are discussed later in section 7.4. A 1% probability cut on the χ^2 of the vertex fits is applied.

[7] This is also true for all other decay channels.

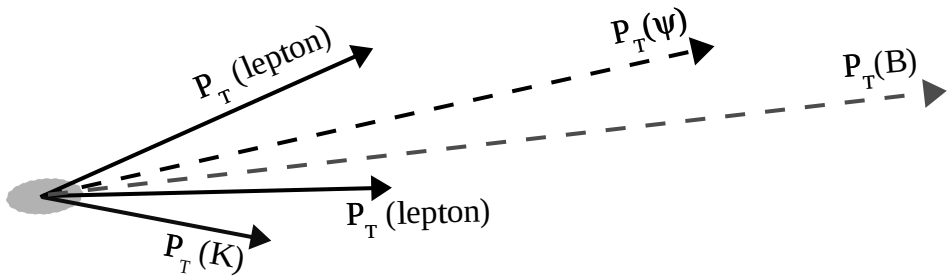

Figure 4.8: The first basic B decay topology relevant to this measurement. All tracks originate from the same vertex. The primary interaction vertex is not shown. The shaded ellipse represents the uncertainties of the measured vertex coordinates. Examples for decay channels with all daughter tracks originating from the same vertex are $B^{\pm} \to J/\psi K^{\pm}$ and $B^0 \to J/\psi K^{*0}$.

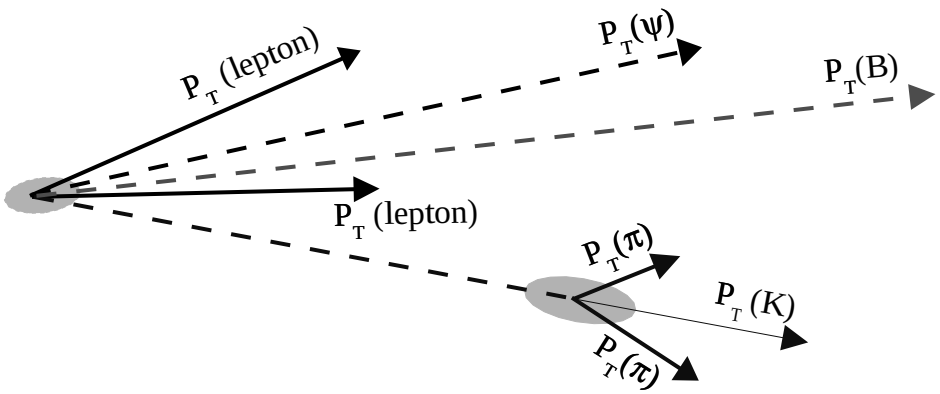

Figure 4.9: In this topology a tertiary vertex from the K_S^0 decay is present. The average distance of the K_S^0 and the B decay vertex in the plane transverse to the beam is $\approx$ 15 cm. The shaded ellipses represent the uncertainties of the measured vertex coordinates. Examples for decay channels with this topology are $B^0 \to J/\psi K_S^0$ and $B^{\pm} \to J/\psi K^{*\pm}$.

4.5 MULTIPLE B MESON CANDIDATES

Multiple B meson candidates (duplicates) that pass all the selection criteria for a given event can arise since all possible combinations of ψ and K candidates are used for the B meson reconstruction. Such additional candidates arise from several other tracks forming an acceptable vertex with the J/ψ or $\psi(2S)$. Another obvious source for duplicates in the decay channel $B^0 \to \psi K^{*0}$ are the $K - \pi$ mass assignment ambiguity and the size of the mass window. Multiple B candidates of the same type in a single event are a significant source of background and can bias the lifetime measurement. B candidates using the same ψ have vertices very close to each other. Including all these vertices in the lifetime measurement would be almost equivalent to use the same B vertex several times. As a consequence, only one candidate of either type is kept. It is important to avoid all selection criteria for the "right" candidate which can possibly bias the lifetime measurement. On the other hand, it makes basically no difference which one of the B candidates is selected since the B vertex is mainly defined by the leptons from the ψ. In the case of the K^{*0} candidates, the one with the mass closest to the accepted world average K^{*0} mass of 896.1 MeV/c^2 [14] is selected. Of all other candidates using the same ψ, the one with the highest χ^2 probability from the global B vertex fit is selected.
Figures 4.10 and 4.11 show the $B^{\pm}$ and B^0 mass distribution after the duplicate removal procedure. To create these histograms, the same cuts are applied on all decay channels: $P_T(B) > 4.5$ GeV/c and $P_T(K) > 1$ GeV/c. For the histograms on the right, an additional cut on the proper decay length (see section 4.7.2) of $c\tau > 100$ μm is applied. This cut reduces background significantly and is ≈ 85 % efficient.

4.6 MISINTERPRETED Λ_B DECAYS

The topology of the decay $\Lambda_B \to J/\psi\ \Lambda$ is very similar to that of the decay $B^0 \to J/\psi\ K^0_S$. This is due to the long lifetime of the Λ baryon of 2.63×10^{-10} s [14]. The decay $\Lambda \to p\ \pi^-$ could be wrongly reconstructed as $K^0_S \to \pi^+\pi^-$ when the π^+ mass is assigned to the proton track. Hence, the $B^0 \to J/\psi\ K^0_S$ data sample might be polluted with Λ_B baryons decaying into $J/\psi\ \Lambda$. This assumption is checked with Monte Carlo (MC) data. 1000000 Λ_B forced to decay into $J/\psi\ \Lambda$ have been generated. These decays are then reconstructed as $B^0 \to J/\psi\ K^0_S$. Figure 4.12 (a) shows the invariant mass spectrum of these wrongly reconstructed Λ_B baryons. 487 entries are in the B^0 signal region between 5.22 and 5.34 GeV/c^2. Using the same selection criteria, 18003 out of 1000000 MC generated B^0 forced to decay into $J/\psi K^0_S$ are correctly reconstructed (Figure 4.12 (b)). The "efficiency" for the reconstruction of Λ_B decays as fake B^0 decays is therefore 0.027 times the efficiency for the reconstruction of real B^0 decays.
The production fractions of the b–hadrons $\Lambda_B : B^0 : B^{\pm} : B^0_S$ are given in [14] as $0.116 \pm 0.020 : 0.389 \pm 0.013 : 0.389 \pm 0.013 : 0.107 \pm 0.014$ and thus for

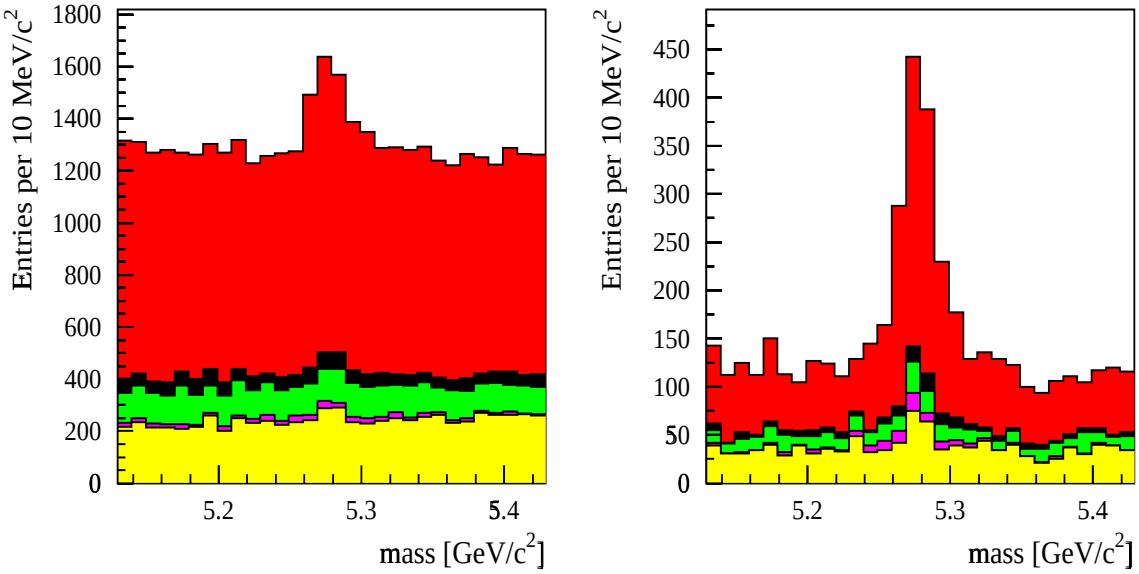

Figure 4.10: The $B^{\pm}$ mass distribution without (left) and with cut $c\tau > 100\ \mu$m (right). The signals are (bottom to top): $B^{\pm} \to J/\psi\ K^{*\pm},\ J/\psi \to \mu^+\mu^-$; $B^{\pm} \to J/\psi\ K^{\pm},\ J/\psi \to e^+e^-$; $B^{\pm} \to \psi(2S)\ K^{\pm}, \psi(2S) \to \mu^+\mu^-$; $B^{\pm} \to \psi(2S)\ K^{\pm}, \psi(2S) \to J/\psi\ \pi^+\pi^-$; $B^{\pm} \to J/\psi\ K^{\pm},\ J/\psi \to \mu^+\mu^-$.

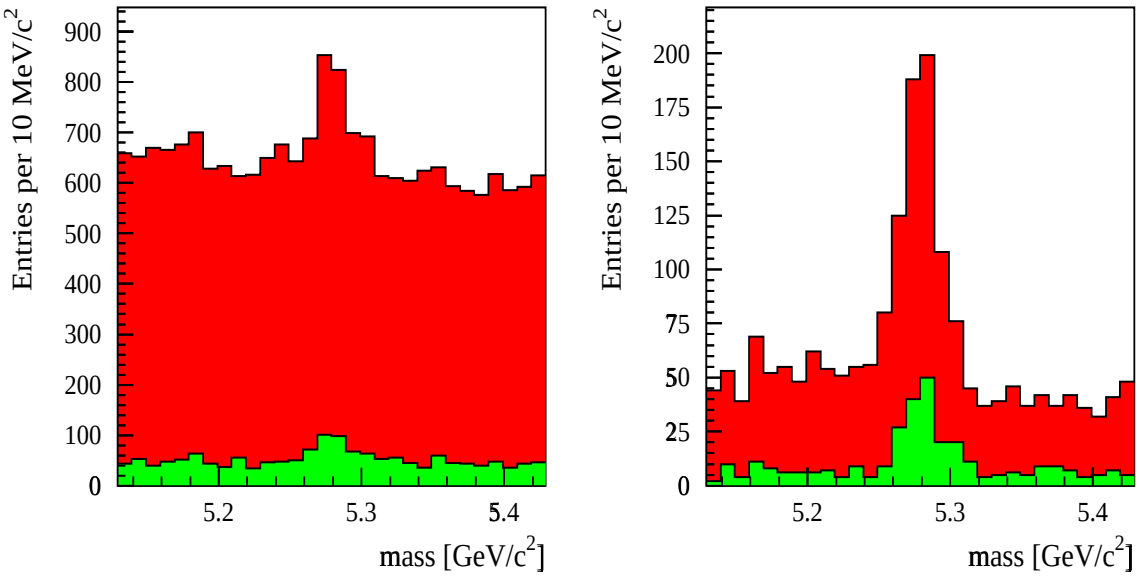

Figure 4.11: The B^0 mass distribution without (left) and with cut $c\tau > 100\ \mu$m (right). The signals are (bottom to top): $B^0 \to J/\psi\ K^0_S,\ J/\psi \to \mu^+\mu^-$; $B^0 \to J/\psi\ K^{*0},\ J/\psi \to \mu^+\mu^-$

$\frac{Br(b\to B^0)}{Br(b\to\Lambda_B)} = 3.35 \pm 0.59$.[8] The branching ratios of the relevant decay channels are:

$$Br(B^0 \to J/\psi\ K^0_S;\ K^0_S \to \pi^+\ \pi^-;\ J/\psi \to \mu^+\ \mu^-) = (3.59 \pm 0.48) \times 10^{-5}$$
$$Br(\Lambda_B \to J/\psi\ \Lambda;\ \Lambda \to p\ \pi^-;\ J/\psi \to \mu^+\ \mu^-) = (1.77 \pm 1.05) \times 10^{-5}$$

Taking reconstruction efficiency, production- and branching ratios into account, the fraction of Λ_B in the $B^0 \to J/\psi\ K^0_S$ sample can be estimated to 0.40 ± 0.25 %. Since the Λ_B lifetime is in the same order of magnitude than the B^0 lifetime, this pollution of the B^0 sample can be neglected.

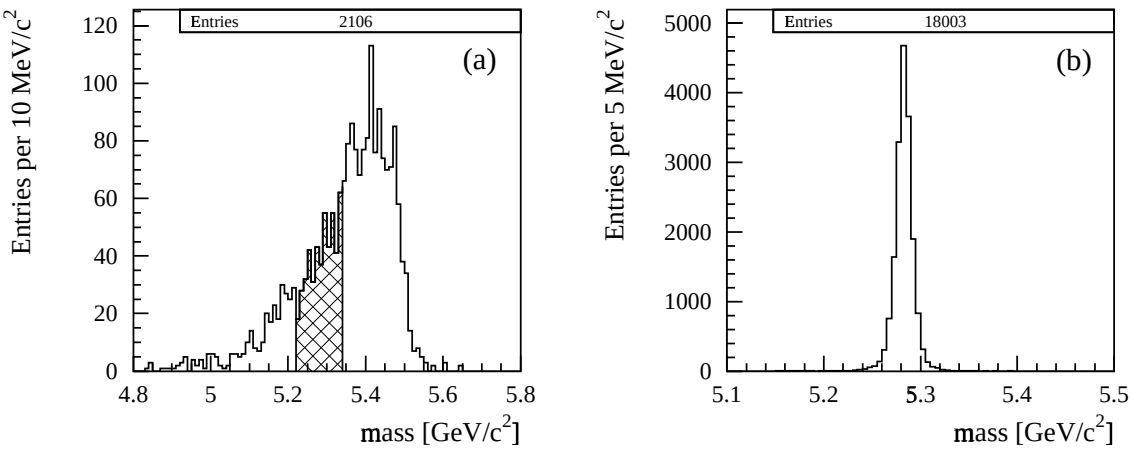

Figure 4.12: (a) The invariant mass spectrum of MC generated $\Lambda_B \to J/\psi\ \Lambda$ decays reconstructed as $B^0 \to J/\psi K^0_S$. The dashed area shows the B^0 signal region. (b) MC generated $B^0 \to J/\psi K^0_S$ decays reconstructed using the same selection criteria as used for (a).

4.7 LIFETIME MEASUREMENT

4.7.1 THE PRIMARY INTERACTION VERTEX

The Tevatron beam has a circular profile which can be described by a Gaussian function with a width of 22 to 23 μm for the Ib running period. During Runs Ia and Ic, the width of the beam was slightly larger. Figure 4.13 shows the beam profile in the interaction region for a typical store (collider fill) during the Ib running period. Plotted is the variation of reconstructed primary vertices in the transverse plane with respect to the calculated average beam position. In the interaction region, the beams follow a straight line but can have an offset with respect to the z axis of the detector. Also, the beams are not necessarily parallel to this axis. The slope of the beam is typically 6 μm/cm in x and -3 μm/cm in y. To get the offset and slope of the beam, a method described in reference [51] is used. The beam position is in general very stable in time. Typical shifts in x and y during one store are less than 4 μm

[8] Reference [50] quotes (0.375 ± 0.023)/(0.09 ± 0.029) = 4.17 ± 1.37 for the ratio $\frac{Br(b\to B^0)}{Br(b\to\Lambda_B)}$.

[52] and contribute only an insignificant amount to the error of the average beam position. The interaction probability as a function of the z coordinate is shown in Figure 4.14 and has a sigma of $\approx$ 31 cm.
In this analysis, the position of the beam at the z coordinate of the reconstructed J/ψ vertex is used as an estimate for the position of the primary interaction vertex. The σ of the transverse beam profile gives the uncertainty of this estimate.

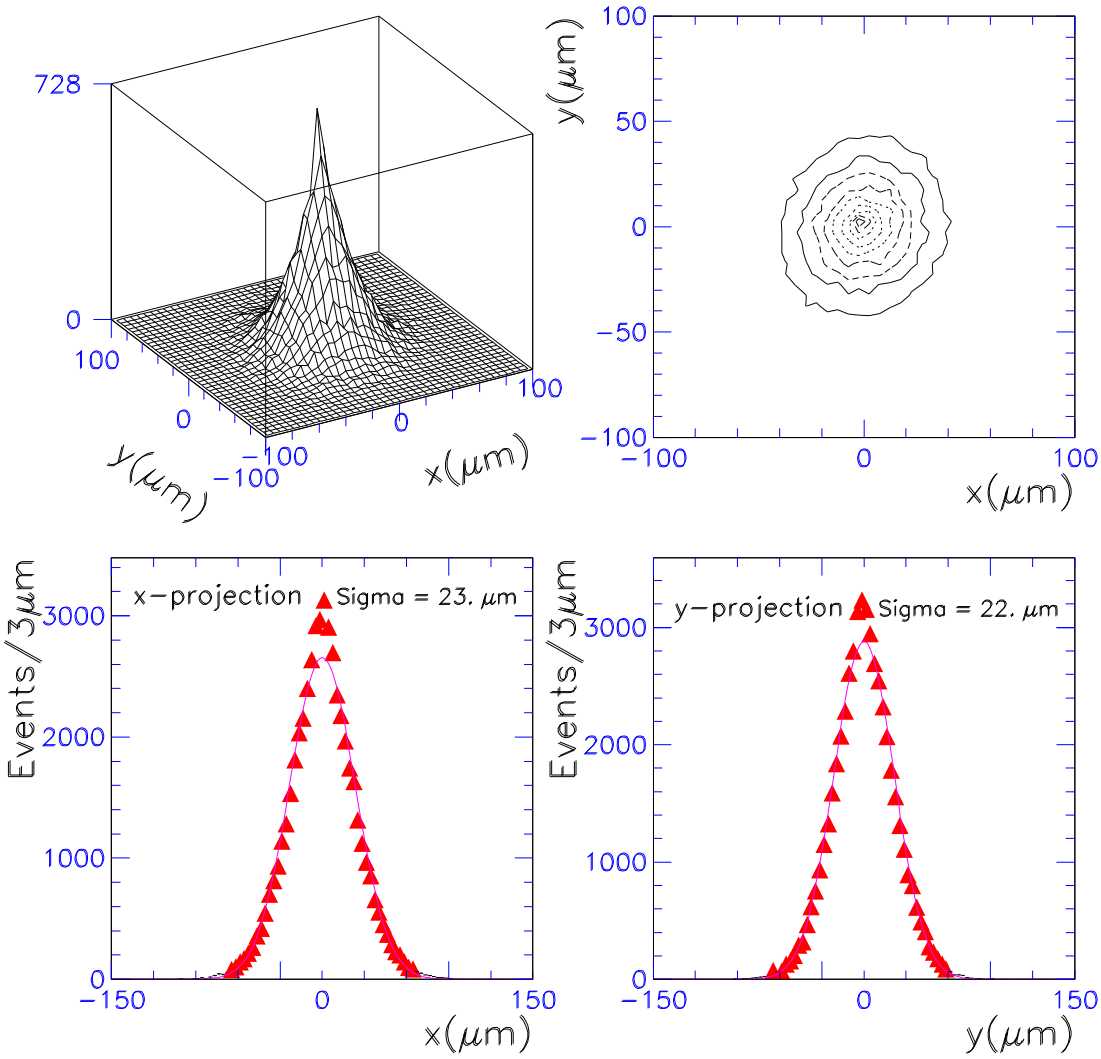

Figure 4.13: The Tevatron beam spot measured with the SVX detector. The upper two plots show the two-dimensional distribution of the beam spot for a given data acquisition run during Run Ib, averaged over the z range covered by the SVX detector. The lower two plots show the x and y projections respectively. [52]

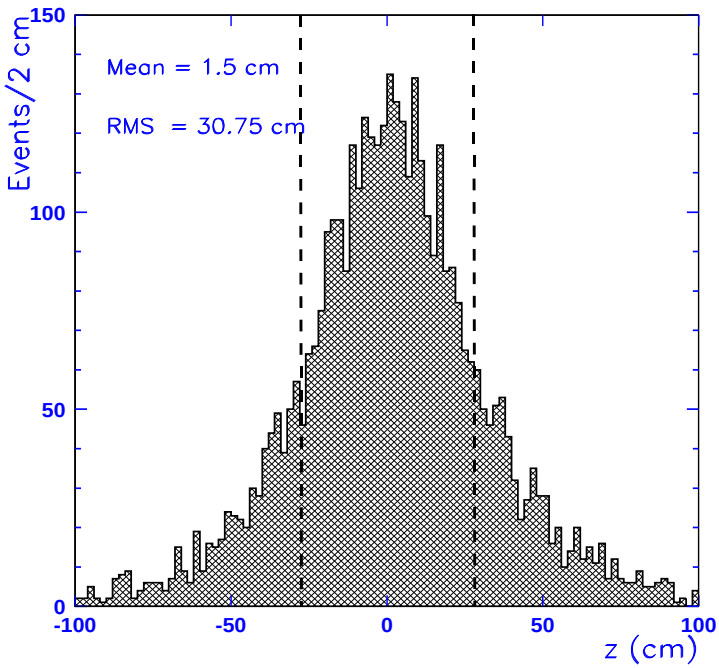

Figure 4.14: The distribution of primary vertices in the z direction for a typical store (collider fill). The interaction probability as a function of z has approximately a Gaussian shape with a σ of $\approx$ 31 cm. The vertical dashed lines mark the range covered by the SVX detector.

4.7.2 THE PROPER DECAY LENGTH

Figure 4.15 shows the primary vertex (x_{prim}, y_{prim}), the decay vertex of the B meson (x_B, y_B) and the momentum vector of the B in the transverse plane $(\vec{P_T^B})$.
The vector $\vec{X}$ is the vector pointing from the primary vertex to the B decay vertex:

$$\vec{X} = \vec{x}_B - \vec{x}_{prim} \tag{4.1}$$

L_{xy} is defined as the projection of this vector onto the transverse momentum of the B meson:

$$L_{xy} = \frac{\vec{X} \cdot \vec{P_T^B}}{|\vec{P_T^B}|} = (x_B - x_{prim}) \cdot \frac{P_x^B}{P_T^B} + (y_B - y_{prim}) \cdot \frac{P_y^B}{P_T^B} \tag{4.2}$$

L_{xy} is a signed variable and is negative for the unlikely configuration where the momentum of the B meson points from the B decay vertex to the direction of the primary vertex; it seems that the particle decays before the point where it was produced.
Using error propagation and assuming that only errors of the B vertex and primary vertex coordinates contribute, one gets the following expression of the error of L_{XY}:

$$\sigma_{L_{xy}}^2 = \frac{1}{(P_T^B)^2} \cdot \left[(\sigma_{xv} P_x^B)^2 + 2\sigma_{xyv} P_x^B P_y^B + (\sigma_{yv} P_y^B)^2 + (\sigma_{x,prim} P_x^B)^2 + (\sigma_{y,prim} P_y^B)^2\right] \tag{4.3}$$

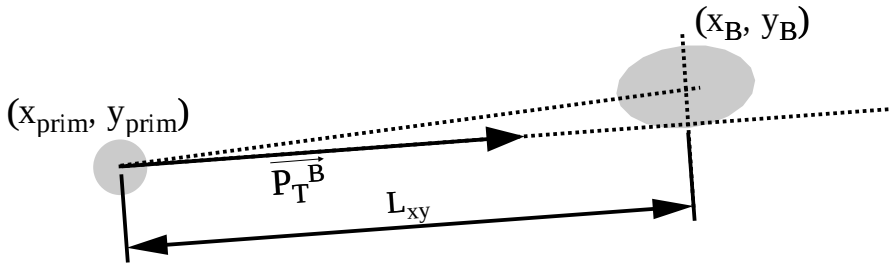

Figure 4.15: Measured path and momentum of a B meson projected onto the plane transverse to the beam. Due to measurement uncertainties, $\vec{P_T^B}$ does not necessarily point to the reconstructed B decay vertex.

where:

$\sigma^2_{xv}, \sigma^2_{yv}, \sigma^2_{xyv}$	: covariance matrix elements from the fit to the B decay vertex
$\sigma_{x,prim}, \sigma_{y,prim}$	: sigma of the primary vertex (beamspot) in x and y
P^B_x, P^B_y	: x and y components of the B momentum.
P^B_T	$= \sqrt{(P^B_x)^2 + (P^B_y)^2}$: transverse momentum of the B.

The value of the proper decay length is then calculated as:

$$c\tau = L_{xy} \cdot \frac{1}{(\beta\gamma)^B_T} = L_{xy} \cdot \frac{m_B}{P^B_T} \tag{4.4}$$

where m_B is the world average B mass (5.2790 GeV/c^2 for the B_u and 5.2794 GeV/c^2 for the B_d). The error of $c\tau$ is :

$$\sigma_{c\tau} = \sigma_{L_{xy}} \cdot \frac{m_B}{P^B_T} \tag{4.5}$$

4.7.3 BREMSSTRAHLUNG CORRECTIONS FOR $J/\psi \to e^+e^-$

Bremsstrahlung losses of the J/ψ decay products cause a smaller measured transverse momentum of the J/ψ and thus a smaller transverse momentum of the reconstructed B meson. Bremsstrahlung losses of muons and other B decay products like pions and kaons are not significant due to the higher mass of these particles. This relative error of the B transverse momentum ($P_T(B)$) due to bremsstrahlung is studied using Monte Carlo (MC) generated data. Figure 4.16 (a) shows the calculated dielectron invariant mass of those MC events where a bremsstrahlung photon is produced. The relative error $(P_T(true) - P_T(measured))/P_T(true)$ is shown in Figure 4.16 (b) as a function of the dielectron mass. Within the dielectron mass range of 2.9 - 3.3 GeV/c^2 the error is less than 4% and can be parameterized with

sufficient accuracy by a straight line. When analysing real data, the $P_T(B)$ is corrected using the fitted function shown in Figure 4.16 (b). This correction is applied to all events with an dielectron invariant mass smaller than the peak mass of 3.057 GeV/c^2. This simplification is acceptable in view of the small relative correction. Events with a dielectron mass less than 2.9 GeV/c^2 are not used for the B meson reconstruction. The dashed area in Figure 4.16 (a) denotes the dielectron mass range for which $P_T(B)$ is corrected.

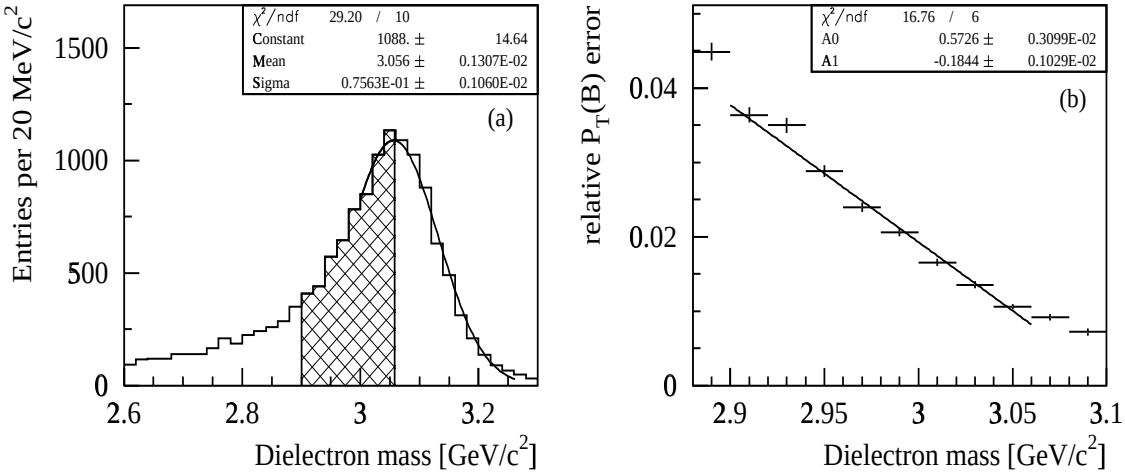

Figure 4.16: (a) Corrections of the B meson P_T are applied for the marked region of the dielectron mass. (b) The relative correction factor of the B meson transverse momentum as a function of the dielectron invariant mass.

Chapter 5

The Fitting Technique

In this chapter, the fitting technique used to extract the B meson lifetime from the data as well as the parameterizations of background and signal distributions are discussed. The actual fitting procedure which is performed in several steps using a C++/ROOT program is described.

5.1 The Maximum Likelihood Method

To determine the best fit lifetime, the maximum likelihood method is used. In general, the likelihood function is defined as:

$$L = \prod_{i=1}^{N} f(x_i, \vec{p}) \tag{5.1}$$

where $f(x_i, \vec{p})$ is the probability density function. The x_i are measurement results and the $\vec{p}$ are a set of unknown parameters. It is important, that the probability density function is normalized for all possible parameters $\vec{p}$.

$$\int f(x, \vec{p})\ dx = 1 \tag{5.2}$$

For a given set of measured values x_i, $L(\vec{p})$ is a function of the parameters $\vec{p}$. It gives the probability to find the values x_i for a given set of parameters $\vec{p}$.
The challenge is now to determine the best estimates of the parameters $\vec{p}$ from the measured values x_i ("fit" the parameters $\vec{p}$ to the data). This is done by maximizing the likelihood function L. For practical reasons one uses the log-likelihood function $\mathcal{L} = -2\ log\ L$ which is then minimized. Also, to avoid extremely large or small numbers during calculations, one writes the log-likelihood function as:

$$\mathcal{L} = -2\ log \prod_{i=1}^{N} f(x_i, \vec{p}) = -2 \sum_{i=1}^{N}\ log\ f(x_i, \vec{p}) \tag{5.3}$$

The maximum likelihood method is described in more detail in numerous books, e.g. [53] and [54].

In this analysis, the parameter to be determined is the average B meson decay length $c\tau$. This is done simultaneously with the determination of parameters describing the shape of the background decay length distribution and parameters relevant to the invariant mass distributions of signal and background. The probability density function has the following form:

$$f = (1 - f_B) \cdot F_{sig} \cdot H_{sig} + f_B \cdot F_{bgr} \cdot H_{bgr} \tag{5.4}$$

f_B is the fraction of the background in the data and is a free parameter in the fit. F_{sig} and F_{bgr} are the parameterizations of the decay length distributions of signal and background. H_{sig} and H_{bgr} are the parameterizations of the invariant mass distributions of signal and background, respectively.
Of each B meson candidate i, the following quantities are determined and used to calculate the probability density function f :

$\lambda^{(i)} = c\tau^{(i)}$	: the proper decay length
$\sigma_\lambda^{(i)}$	: the measurement error of $\lambda^{(i)}$
$m^{(i)}$	: the invariant mass of the tracks constituting the reconstructed B decay vertex
$\sigma_m^{(i)}$	: the measurement error of $m^{(i)}$.

5.2 THE MASS DISTRIBUTIONS OF SIGNAL AND BACKGROUND

The signal mass distribution is parameterized by a Gaussian function

$$H_{sig}(M, s_m; m^{(i)}, \sigma_m^{(i)}) = \frac{1}{\sqrt{2\pi}\ s_m \sigma_m^{(i)}} \cdot exp\left\{ -\frac{(m^{(i)} - M)^2}{2\ (s_m \sigma_m^{(i)})^2} \right\} \tag{5.5}$$

The mean B meson mass M and the error scale factor s_m are free parameters in the fit. s_m is introduced to account for a possible scaling of errors in the data.
The background mass distribution is described by a straight line

$$H_{bgr}(C_m; m^{(i)}) = \left(\frac{2}{(M_{max})^2 - (M_{min})^2} - \frac{2\ C_m}{M_{max} + M_{min}} \right) \cdot m^{(i)} + C_m \tag{5.6}$$

M_{max} and M_{min} are the upper and lower mass boundaries used for the fit. C_m is a free parameter in the fit. The second parameter of the straight line equation is eliminated by the normalization condition

$$\int_{M_{min}}^{M_{max}} H_{bgr}(C_m; m)\ dm = 1 \tag{5.7}$$

5.3 THE SIGNAL $c\tau$ DISTRIBUTION

The probability density function of the measured proper decay length of the B mesons is an exponential decay function. However, there is an error on each measurement and therefore the probability density function is modeled by a Gaussian resolution function convoluted with an exponential function : $F_{sig} = G \otimes E$. The normalized Gaussian and exponential functions have the following form:

$$G(s_\lambda; y, \sigma_\lambda^{(i)}) = \frac{1}{\sqrt{2\pi}\ s_\lambda \sigma_\lambda^{(i)}} \cdot exp\left\{\frac{-y^2}{2\ (s_\lambda \sigma_\lambda^{(i)})^2}\right\} \tag{5.8}$$

$$E(c\tau; \lambda_{true}^{(i)}) = \frac{1}{c\tau} \cdot exp\left\{\frac{-\lambda_{true}^{(i)}}{c\tau}\right\}; \quad for\ \lambda_{true}^{(i)} > 0 \tag{5.9}$$

$\lambda_{true}^{(i)}$ is the (unknown) true decay length of the B candidate and $y = \lambda^{(i)} - \lambda_{true}^{(i)}$ is the difference of measured and true decay length.
The average B meson decay length $c\tau$ and the error scale factor s_λ are free parameters in the fit. Similar as s_m in the signal mass distribution, s_λ is introduced to account for a possible scaling of the measurement errors $\sigma_\lambda^{(i)}$.
The convolution of G and E is defined by

$$G \otimes E(s_\lambda, c\tau; \lambda^{(i)}, \sigma_\lambda^{(i)}) = \frac{1}{\sqrt{2\pi}\ s_\lambda \sigma_\lambda^{(i)}\ c\tau} \int_{-\infty}^{\lambda^{(i)}} exp\left\{\frac{-(\lambda^{(i)} - y)}{c\tau}\right\} exp\left\{\frac{-y^2}{2\ (s_\lambda \sigma_\lambda^{(i)})^2}\right\} dy \tag{5.10}$$

The exponent can be written as

$$\begin{aligned}
&-\tfrac{1}{2\ (s_\lambda \sigma_\lambda^{(i)})^2\ c\tau}\left[2\ (s_\lambda \sigma_\lambda^{(i)})^2\ (\lambda^{(i)} - y) + c\tau\ y^2\right] \\
&= -\tfrac{1}{2\ (s_\lambda \sigma_\lambda^{(i)})^2\ c\tau} \cdot \left[2\ (s_\lambda \sigma_\lambda^{(i)})^2 \lambda^{(i)} - 2\ (s_\lambda \sigma_\lambda^{(i)})^2 y + c\tau y^2 + \tfrac{(s_\lambda \sigma_\lambda^{(i)})^4}{c\tau} - \tfrac{(s_\lambda \sigma_\lambda^{(i)})^4}{c\tau}\right] \\
&= -\tfrac{\lambda^{(i)}}{c\tau} + \tfrac{(s_\lambda \sigma_\lambda^{(i)})^2}{2\ (c\tau)^2} - \tfrac{1}{2\ (s_\lambda \sigma_\lambda^{(i)})^2}\left(y - \tfrac{(s_\lambda \sigma_\lambda^{(i)})^2}{c\tau}\right)^2
\end{aligned}$$

which gives:

$$G \otimes E = \frac{1}{\sqrt{2\pi} s_\lambda \sigma_\lambda^{(i)} c\tau}\ exp\left\{\frac{(s_\lambda \sigma_\lambda^{(i)})^2}{2(c\tau)^2} - \frac{\lambda^{(i)}}{c\tau}\right\} \int_{-\infty}^{\lambda^{(i)}} exp\left\{-\frac{1}{2}\left(\frac{y}{s_\lambda \sigma_\lambda^{(i)}} - \frac{s_\lambda \sigma_\lambda^{(i)}}{c\tau}\right)^2\right\} dy$$

Substituting $v = \frac{y}{s_\lambda \sigma_\lambda^{(i)}} - \frac{s_\lambda \sigma_\lambda^{(i)}}{c\tau}$; $dy = \sigma_\lambda^{(i)} dv$ results in

$$G \otimes E = \frac{1}{\sqrt{2\pi}\ c\tau}\ exp\left\{\frac{(s_\lambda \sigma_\lambda^{(i)})^2}{2(c\tau)^2} - \frac{\lambda^{(i)}}{c\tau}\right\} \int_{-\infty}^{\frac{\lambda^{(i)}}{s_\lambda \sigma_\lambda^{(i)}} - \frac{s_\lambda \sigma_\lambda^{(i)}}{c\tau}} exp\left\{\frac{v^2}{2}\right\} dv$$

The function normal frequency function in the CERN library [55] is defined as:

$$freq(x) = \frac{1}{\sqrt{2\pi}} \cdot \int_{-\infty}^{x} exp\left\{\frac{-t^2}{2}\right\} dt \tag{5.11}$$

Using the $freq$ function, one finally gets the following expression for $F_{sig} = G \otimes E$ which has then to be substituted in equation 5.4:

$$G \otimes E = \frac{1}{c\tau}\, exp\left\{\frac{(s_\lambda \sigma_\lambda^{(i)})^2}{2(c\tau)^2} - \frac{\lambda^{(i)}}{c\tau}\right\} \cdot \left[1 - freq\left(\frac{s_\lambda \sigma_\lambda^{(i)}}{c\tau} - \frac{\lambda^{(i)}}{s_\lambda \sigma_\lambda^{(i)}}\right)\right] \tag{5.12}$$

5.4 THE BACKGROUND $c\tau$ DISTRIBUTION

The background $c\tau$ distribution F_{bgr} is parameterized as the sum of a central Gaussian function for the zero-lifetime events, an exponential tail at negative $\lambda^{(i)}$ and two exponential tails at positive $\lambda^{(i)}$. The negative exponential tail handles the mismeasured background for $\lambda^{(i)} < 0$. In the $\lambda^{(i)} > 0$ region, two exponential tails are needed to accurately fit the data. In this region there is also long-lifed background, for example from sequential B-decays ($b \to c\mu^- \to s\mu^+\mu^-$) and so-called "volunteers", tracks which accidently fit to a ψ vertex but do not originate from the B meson decay. The parameterization of F_{bgr} is as follows:

$$\begin{aligned}
F_{bgr} &= (1 - f_- - f_+ - f_{++}) \cdot \frac{1}{\sqrt{2\pi}\; s_\lambda \sigma_\lambda^{(i)}} \cdot exp\left\{\frac{-(\lambda^{(i)})^2}{2\;(s_\lambda \sigma_\lambda^{(i)})^2}\right\} \\
&+ \frac{f_+}{\lambda_+} \cdot e^{-\lambda^{(i)}/\lambda_+} + \frac{f_{++}}{\lambda_{++}} \cdot e^{-\lambda^{(i)}/\lambda_{++}}; \qquad for\ \lambda^{(i)} \geq 0 \\
F_{bgr} &= (1 - f_- - f_+ - f_{++}) \cdot \frac{1}{\sqrt{2\pi}\; s_\lambda \sigma_\lambda^{(i)}} \cdot exp\left\{\frac{-(\lambda^{(i)})^2}{2\;(s_\lambda \sigma_\lambda^{(i)})^2}\right\} \\
&+ \frac{f_-}{\lambda_-} e^{-\lambda^{(i)}/\lambda_-}; \qquad for\ \lambda^{(i)} < 0
\end{aligned} \tag{5.13}$$

The six free parameters in the fit describing the shape of the background $c\tau$ distribution are:

λ_-, f_- : slope and fraction of the negative exponential tail.
λ_+, f_+ : slope and fraction of the first positive exponential tail.
λ_{++}, f_{++} : slope and fraction of the second positive exponential tail.

5.5 FITTING PROCEDURE

To perform the lifetime fits, a C++ program was developed, using the ROOT [56] package for data handling, histograming and as an interface to the general function minimization software MINUIT [57]. MINUIT is used in this analysis to do the actual minimization of the log-likelihood functions. It returns the best fit values of the free parameters as well as their uncertainties.

Before a combined fit of all decay channels is done, the data of each decay channel is fitted individually in several steps:

- An unbinned likelihood fit to the mass distribution is performed to determine first estimates of the parameters M and C_m (see Section 5.2). For this fit a decay length cut of $c\tau >$ 100 μm is imposed on the data.
- An unbinned likelihood fit to the background $c\tau$ distribution is made to determine first estimates of the fractions and length scales of the exponential tails in the background $c\tau$ parameterization. For this fit, events with an invariant mass in the sideband regions (see Figure 5.1) are used.
- The simultaneous mass and lifetime fit. The log-likelihood function to be minimized has the form

$$\mathcal{L} = -2 \sum_{i=1}^{N} log\ f(...) \tag{5.14}$$

  where f is the probability density function (5.4). Its components are described in the sections 5.2, 5.3 and 5.4. $\mathcal{L}$ is calculated using all events in the mass range of $\pm$ 150 MeV/c^2 around the world average B meson mass of 5.279 GeV/c^2. N is the number of events in this mass range.

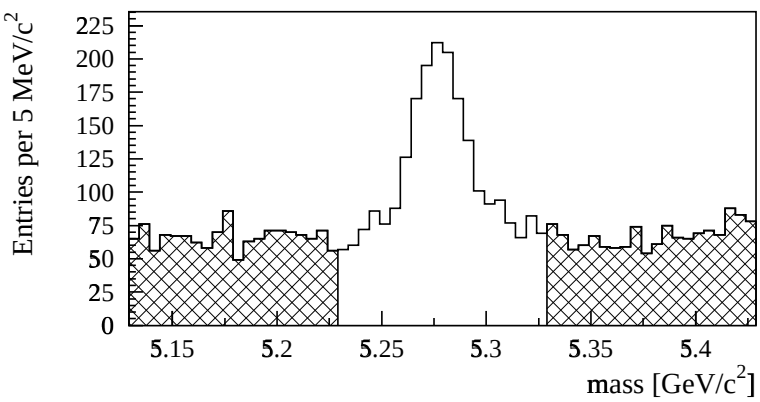

Figure 5.1: The mass distribution of $B^{\pm} \rightarrow J/\psi\ K^{\pm}$ events. The dashed areas are the "sidebands". In this histogram, the background is reduced significantly by requiring a decay length > 100 μm to point up the mass peak. This requirement is not applied on the data used in the fit.

When all fits of the individual decay channels are done, a combined fit of all decay channels of each B species ($B^{\pm}$ and B^0) is performed. The log-likelihood function to be minimized in this combined fit has the following form :

$$\mathcal{L} = -2 \sum_{j=1}^{K} \sum_{i=1}^{N_j} log\ f(...) \tag{5.15}$$

K is the number of data samples (decay channels). N_j is the number of events of the data sample j in the ± 150 MeV/c^2 mass range around the world average B meson mass. f is the probability density function (5.4) as described in sections 5.2 – 5.4 with some important changes:

- All measured quantities get j as a second superscript: $\lambda^{(ji)}, \sigma_{\lambda}^{(ji)}, m^{(ji)}, \sigma_{m}^{(ji)}$.
- Fit parameters describing the shape of the background mass and $c\tau$ distributions as well as the background fraction f_B are different for each data sample. Thus they get a superscript j to denote their dependence on the data sample: $C_m^{(j)},\ f_-^{(j)},\ f_+^{(j)},\ f_{++}^{(j)},\ \lambda_-^{(j)},\ \lambda_+^{(j)},\ \lambda_{++}^{(j)},\ f_B^{(j)}$
  It is very important to use different background parameters for the diverse decay channels in order to fit the different background $c\tau$ and mass distributions accurately.
- Common parameters to all data samples are the average decay length $c\tau$, the error scale factor s_λ, the mean mass M and the error scale factor s_m.

The number of free parameters in the combined fit is $4 + K \cdot 8$. The results of the fits of the individual decay channels serve as first estimates for the combined fit.

Chapter 6

Results

In this chapter, the results of the fitting procedures are presented. The results of the fits to the different individual data samples are shown as well as the results of the combined fits of all $B^{\pm}$ and B^0 decay channels. Consistency checks of the lifetime results are discussed.

6.1 Individual Decay Channels

In Chapter 4 the issue of transverse momentum thresholds on the reconstructed B meson candidates and daughter kaons was not addressed. These thresholds influence the number of signal events and the background fraction f_B in the data samples and thus have an effect on the statistical error of the average B meson decay length determined in the fit. Minimum transverse momentum cuts of the reconstructed B meson ($P_T(B)$) and the decay kaon ($P_T(K)$) are applied individually for each data sample (decay channel). The $P_T(B)$ cut is varied from 4 GeV/c to 6 GeV/c in steps of 0.5 GeV/c. The $P_T(K)$ cut is varied from 0.75 GeV/c to 1.5 GeV/c in steps of 0.25 GeV/c for each $P_T(B)$ cut value. For every combination of $P_T(B)$ and $P_T(K)$ cuts, the fitting procedure as described in section 5.5 is performed. Finally, the cut values are chosen in the way that the statistical error of the average B meson decay length $c\tau$ is smallest.

The number of signal candidates in the different data samples depends on the B meson production cross section, the branching ratios (BR) and reconstruction efficiencies (including trigger efficiencies). Branching ratios and reconstruction efficiencies vary for the different decay channels. Not all data samples are big enough to achieve stable fits. Stable fit results could be achieved for the following five $B^{\pm}$ and two B^0 decay channels:

$B^{\pm} \to J/\psi\ K^{\pm}$; $\quad J/\psi \to \mu^+\mu^-$
$B^{\pm} \to J/\psi\ K^{\pm}$; $\quad J/\psi \to e^+e^-$
$B^{\pm} \to \psi(2S)\ K^{\pm}$; $\quad \psi(2S) \to \mu^+\mu^-$
$B^{\pm} \to \psi(2S)\ K^{\pm}$; $\quad \psi(2S) \to J/\psi\ \pi^+\pi^-;\ J/\psi \to \mu^+\mu^-$

$B^{\pm} \to J/\psi\ K^{*\pm}$; $\quad K^{*\pm} \to K_S^0\ \pi^{\pm} \to \pi^+\ \pi^-\ \pi^{\pm}$; $J/\psi \to \mu^+\mu^-$

$B^0 \to J/\psi\ K_S^0$; $\quad K_S^0 \to \pi^+\pi^-$; $J/\psi \to \mu^+\mu^-$
$B^0 \to J/\psi\ K^{*0}$; $\quad K^{*0} \to K^{\pm}\ \pi^{\mp}$; $J/\psi \to \mu^+\mu^-$

These are the data samples included in the combined $B^{\pm}$ and B^0 fits. On the following pages, the fit results of these individual decay channels are presented. The transverse momentum cuts giving the smallest statistical uncertainties for each particular decay channel are stated on the top of each page. The histograms displayed on each page show the results of the fits performed to find first estimates for the parameters to be fitted in the simultaneous mass-lifetime fit as well as the result of this simultaneous fit. The histogram on the top left shows the fit to the mass distribution of events with $c\tau > 100\ \mu$m to determine M and C_m. The histogram on the top right shows the fit to the background decay length distribution of sideband events (see Figure 5.1) to determine f_-, λ_-, f_+, λ_+, f_{++} and λ_{++}. Clearly visible are the different shapes of the background decay length distributions of the individual decay channels. Note also the quite different background fractions f_B stated in the tables for the different decay channels. The necessity to use different parameters for the background parameterizations of the various decay channels in the combined fit is obvious.
The result of the simultaneous fit is shown in the bottom histogram where the hatched area is the signal contribution. The best fit values and corresponding uncertainties of the parameters are shown in the table below the histograms. The bottom line of the table contains the average B meson lifetime τ determined by the fit to the particular data sample as well as its statistical uncertainty. The number of signal candidates N_{Signal} is computed from the total number of events in the data sample (N_{Sample}) and the fitted background fraction f_B as $N_{Signal} = (1-f_B)\cdot N_{Sample}$.

6.1.1 Results for the Decay Channel $B^{\pm} \to J/\psi\ K^{\pm}$; $J/\psi \to \mu^+\mu^-$

P_T cuts for smallest error of $c\tau$: $P_T(B) > 4.5$ GeV/c^2, $P_T(K) > 1.0$ GeV/c^2

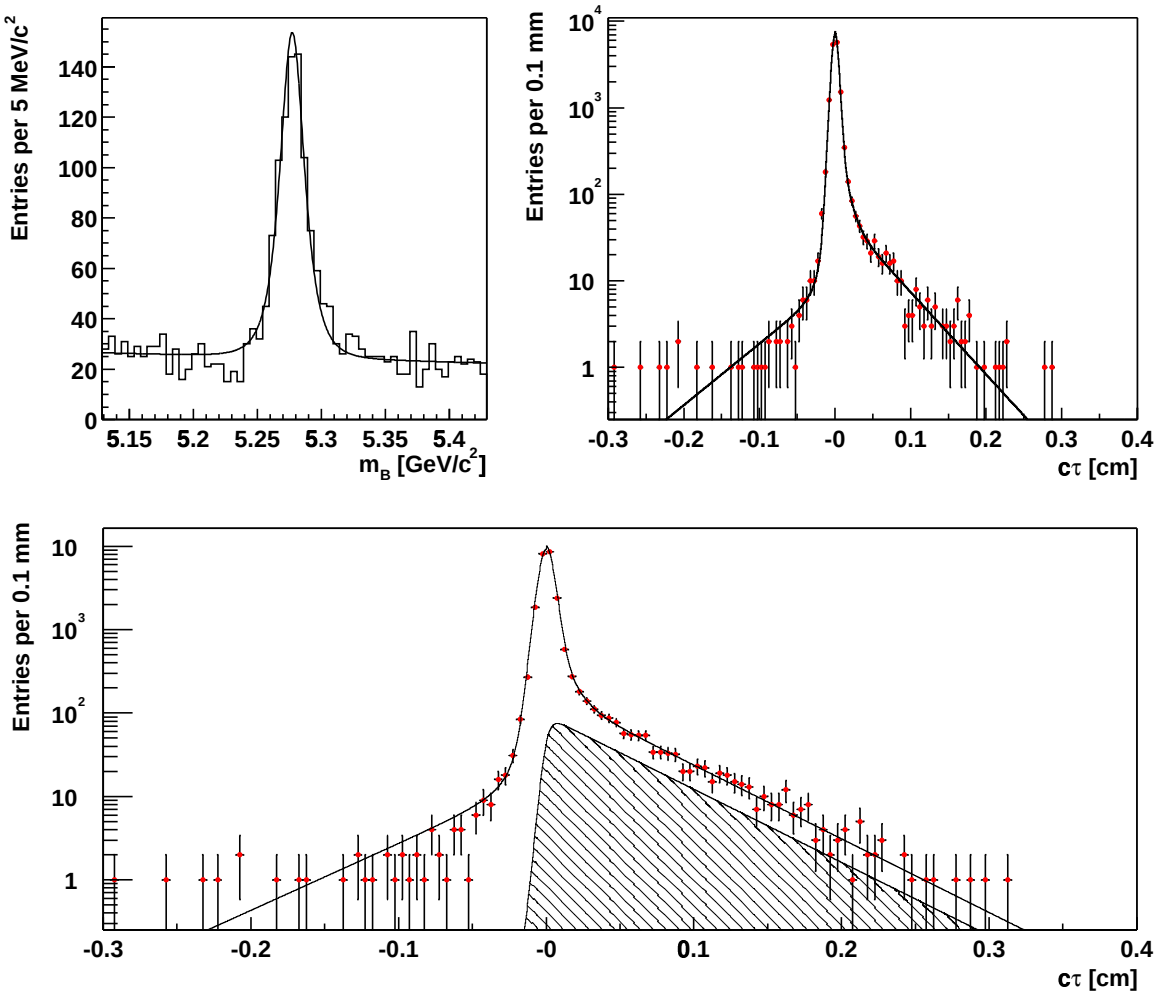

Figure 6.1: Mass distribution (top left), background $c\tau$ (top right) and $c\tau$ (bottom) distributions of reconstructed $B^{\pm} \to J/\psi\ K^{\pm}$; $J/\psi \to \mu^+\mu^-$ decays.

parameter	value	error	parameter	value	error
M [GeV/c^2]	5.2773	0.0005	f_-	0.00827	0.00073
C_M	13.124	5.331	λ_- [μm]	541.69	46.68
s_m	1.1388	0.0540	f_+	0.06267	0.00509
$c\tau$ [μm]	495.59	18.73	λ_+ [μm]	81.84	7.71
s_λ	1.1571	0.0070	f_{++}	0.03859	0.00316
f_B	0.9616	0.0016	λ_{++} [μm]	487.39	29.03
τ [ps]	**1.653**	**0.061**	N_{Signal}	905.7	36.9

Table 6.1: Fit results of the decay channel $B^{\pm} \to J/\psi\ K^{\pm}$; $J/\psi \to \mu^+\mu^-$.

6.1.2 RESULTS FOR THE DECAY CHANNEL $B^{\pm} \rightarrow J/\psi\ K^{\pm}$; $J/\psi \rightarrow e^{+}e^{-}$

P_T cuts for smallest error of $c\tau$: $P_T(K) > 0.75$ GeV/c^2. The minimum transverse momentum of the B mesons is ≈ 6 GeV/c due to the high P_T of the trigger electron. The average $P_T(B)$ is ≈ 14 GeV/c. No further P_T cut on the B candidate is applied.

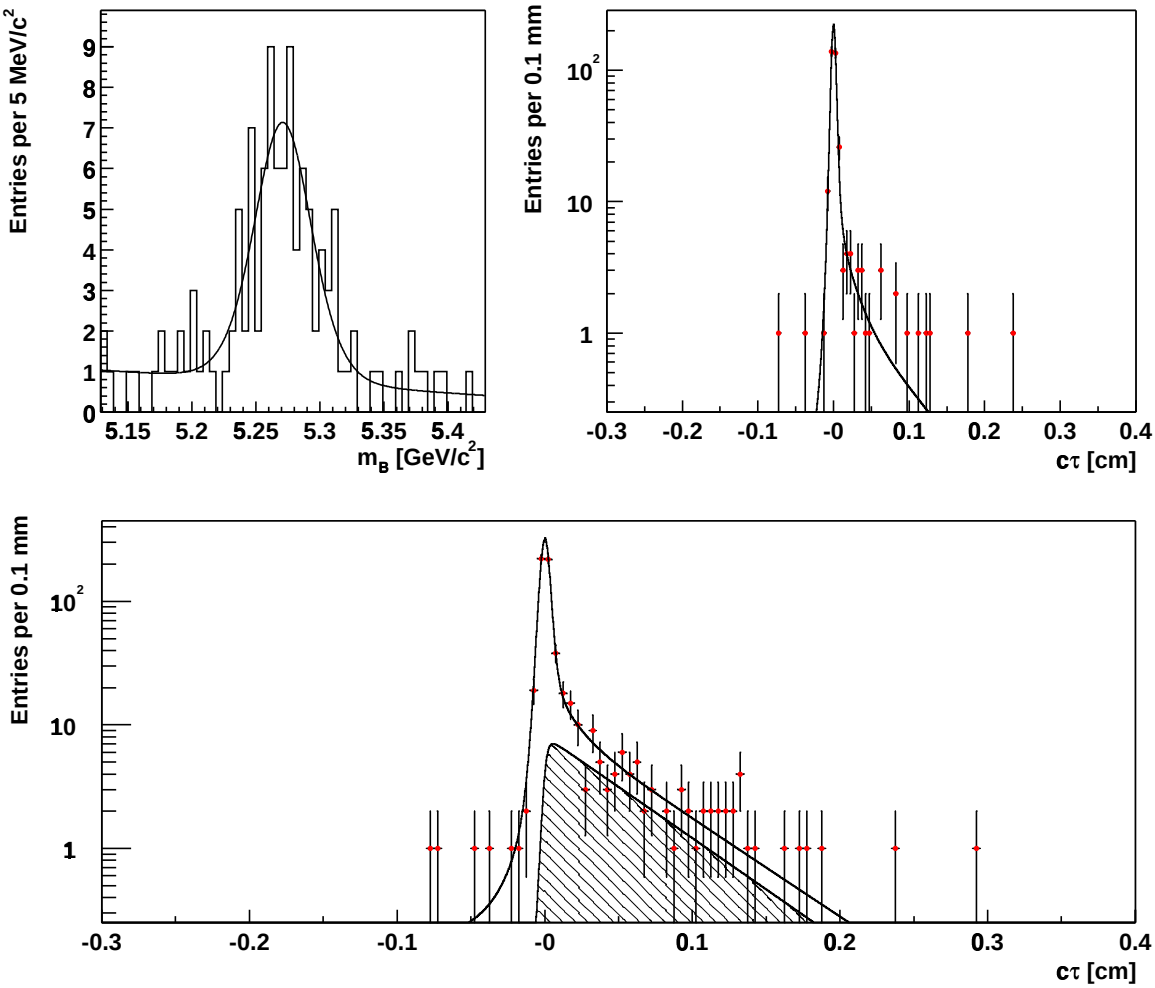

Figure 6.2: Mass distribution (top left), background $c\tau$ (top right) and $c\tau$ (bottom) distributions of reconstructed $B^{\pm} \rightarrow J/\psi\ K^{\pm}$; $J/\psi \rightarrow e^{+}e^{-}$ decays.

parameter	value	error	parameter	value	error
M [GeV/c^2]	5.2712	0.0032	f_-	0.01690	0.00599
C_M	53.791	31.742	λ_- [μm]	1517.05	536.97
s_m	0.7693	0.0997	f_+	0.05948	0.02932
$c\tau$ [μm]	523.23	63.07	λ_+ [μm]	124.19	61.79
s_λ	1.1708	0.0468	f_{++}	0.06355	0.02767
f_B	0.8631	0.0167	λ_{++} [μm]	598.69	178.72
τ [ps]	**1.745**	**0.210**	N_{Signal}	85.4	10.4

Table 6.2: Fit results of the decay channel $B^{\pm} \rightarrow J/\psi\ K^{\pm}$; $J/\psi \rightarrow e^{+}e^{-}$.

6.1.3 Results for the Decay Channel $B^{\pm} \to \psi(2S)\ K^{\pm}$; $\psi(2S) \to \mu^+\mu^-$

P_T cuts for smallest error of $c\tau$: $P_T(B) > 4.5$ GeV/c^2, $P_T(K) > 1.0$ GeV/c^2

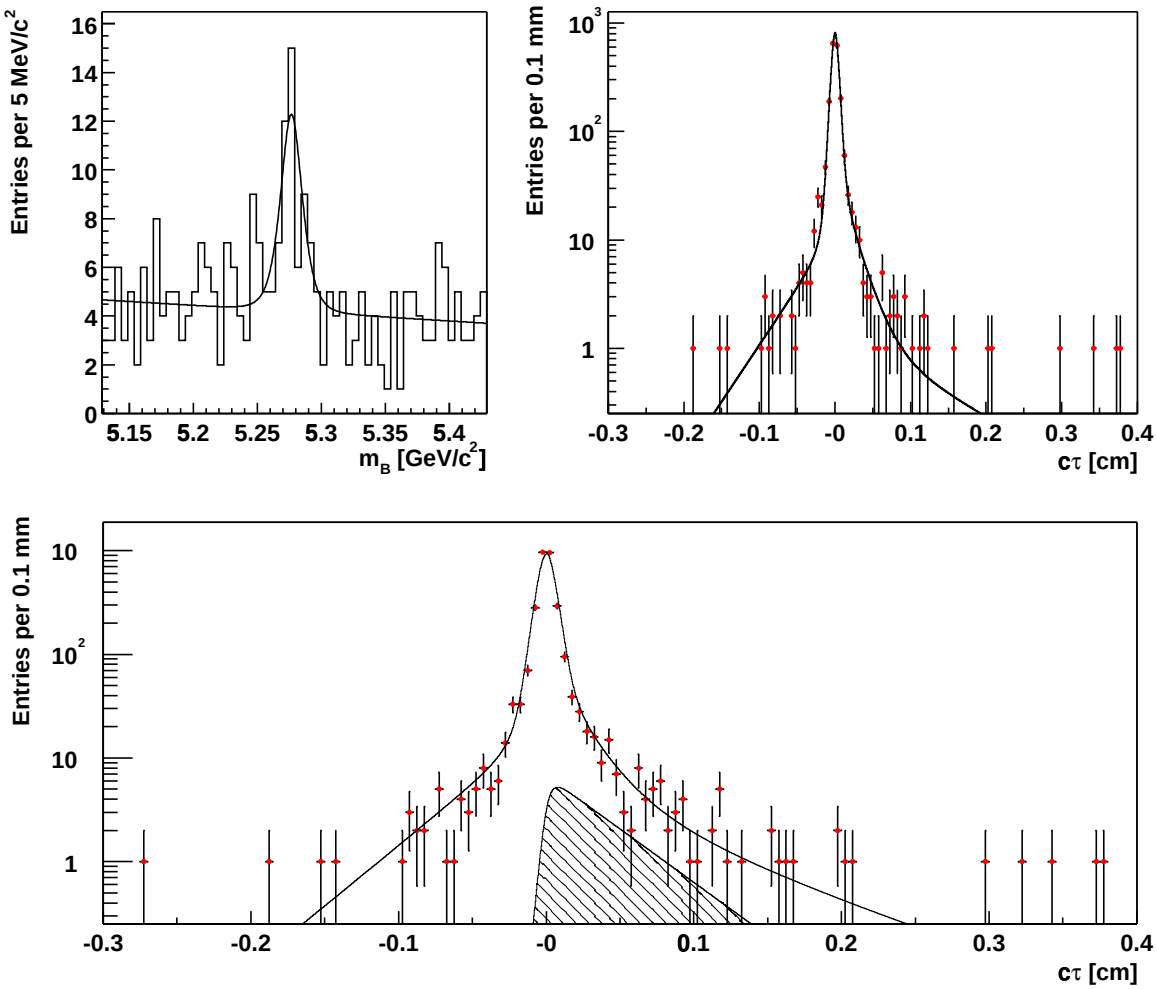

Figure 6.3: Mass distribution (top left), background $c\tau$ (top right) and $c\tau$ (bottom) distributions of reconstructed $B^{\pm} \to \psi(2S)\ K^{\pm}$; $\psi(2S) \to \mu^+\mu^-$ decays.

parameter	value	error	parameter	value	error
M [GeV/c^2]	5.2767	0.0022	f_-	0.05312	0.00544
C_M	16.790	12.764	λ_- [μm]	373.04	36.87
s_m	1.2529	0.3548	f_+	0.07296	0.00844
$c\tau$ [μm]	420.82	74.70	λ_+ [μm]	170.02	34.85
s_λ	1.3122	0.0244	f_{++}	0.02038	0.00735
f_B	0.9810	0.0035	λ_{++} [μm]	925.99	211.37
τ [ps]	**1.404**	**0.249**	N_{Signal}	56.7	10.6

Table 6.3: Fit results of the decay channel $B^{\pm} \to \psi(2S)\ K^{\pm}$; $\psi(2S) \to \mu^+\mu^-$.

6.1.4 RESULTS FOR THE DECAY CHANNEL $B^{\pm} \to \psi(2S)\ K^{\pm}$; $\psi(2S) \to J/\psi\ \pi^+\pi^-$; $J/\psi \to \mu^+\mu^-$

P_T cuts for smallest error of $c\tau$: $P_T(B) > 4.5$ GeV/c^2, $P_T(K) > 0.75$ GeV/c^2

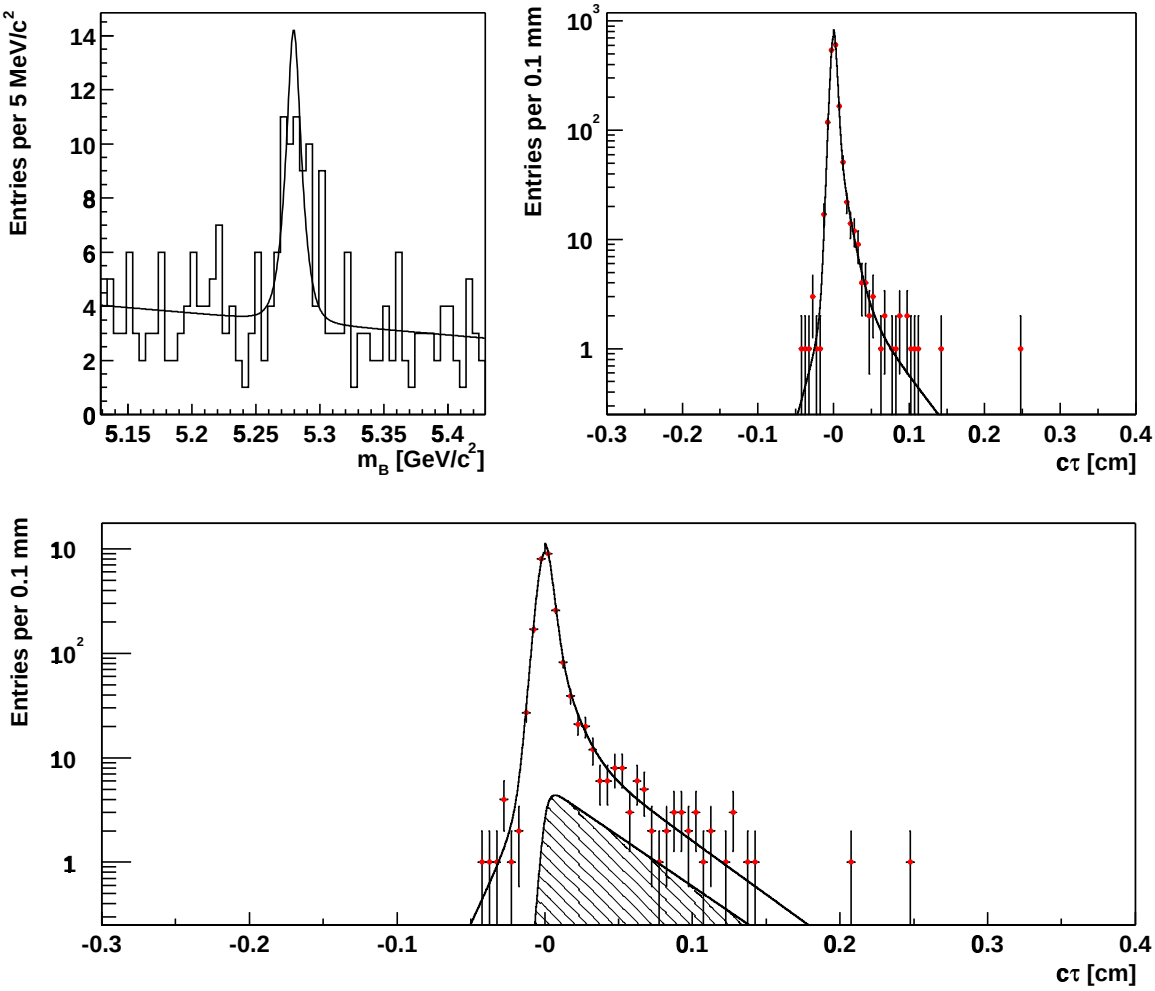

Figure 6.4: Mass distribution (top left), background $c\tau$ (top right) and $c\tau$ (bottom) distributions of reconstructed $B^{\pm} \to \psi(2S)\ K^{\pm}$; $\psi(2S) \to J/\psi\ \pi^+\pi^-$; $J/\psi \to \mu^+\mu^-$ decays.

parameter	value	error	parameter	value	error
M [GeV/c^2]	5.2796	0.0017	f_-	0.00832	0.00428
C_M	24.114	14.310	λ_- [μm]	149.86	55.58
s_m	1.0413	0.2795	f_+	0.1490	0.01697
$c\tau$ [μm]	450.88	76.77	λ_+ [μm]	86.83	11.80
s_λ	1.1562	0.0241	f_{++}	0.04042	0.01179
f_B	0.9799	0.0043	λ_{++} [μm]	408.81	78.62
τ [ps]	**1.504**	**0.256**	N_{Signal}	48.5	10.3

Table 6.4: Fit results of the decay channel $B^{\pm} \to \psi(2S)\ K^{\pm}$; $\psi(2S) \to J/\psi\ \pi^+\pi^-$; $J/\psi \to \mu^+\mu^-$.

6.1.5 RESULTS FOR THE DECAY CHANNEL $B^{\pm} \to J/\psi\ K^{*\pm}$; $K^{*\pm} \to K^0_S\ \pi^{\pm}$; $J/\psi \to \mu^+\mu^-$

P_T cuts for smallest error of $c\tau$: $P_T(B) > 5.5$ GeV/c^2, $P_T(K) > 1.0$ GeV/c^2

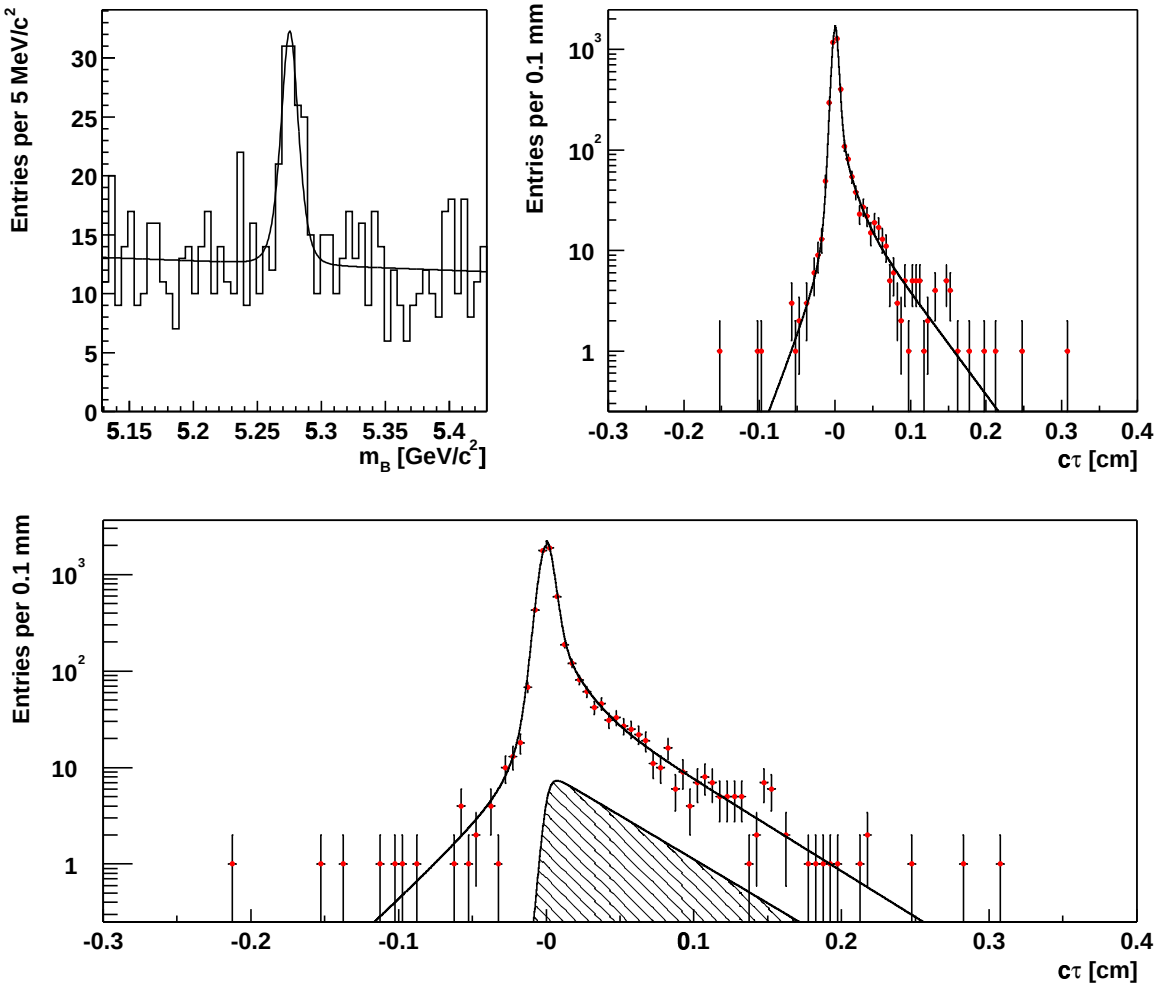

Figure 6.5: Mass distribution (top left), background $c\tau$ (top right) and $c\tau$ (bottom) distributions of reconstructed $B^{\pm} \to J/\psi\ K^{*\pm}$; $K^{*\pm} \to K^0_S\ \pi^{\pm}$; $J/\psi \to \mu^+\mu^-$ decays.

parameter	value	error	parameter	value	error
M [GeV/c^2]	5.2753	0.0017	f_-	0.01278	0.00225
C_M	9.001	7.428	λ_- [μm]	302.67	45.35
s_m	1.0282	0.2153	f_+	0.10057	0.01633
$c\tau$ [μm]	478.33	70.08	λ_+ [μm]	127.40	24.10
s_λ	1.1784	0.0163	f_{++}	0.09529	0.01745
f_B	0.9847	0.0024	λ_{++} [μm]	453.02	44.77
τ [ps]	**1.596**	**0.234**	N_{Signal}	86.1	13.4

Table 6.5: Fit results of the decay channel $B^{\pm} \to J/\psi\ K^{*\pm}$; $K^{*\pm} \to K^0_S\ \pi^{\pm}$; $J/\psi \to \mu^+\mu^-$.

6.1.6 RESULTS FOR THE DECAY CHANNEL $B^0 \to J/\psi\ K^0_S$; $K^0_S \to \pi^+\ \pi^-$; $J/\psi \to \mu^+\mu^-$

P_T cuts for smallest error of $c\tau$: $P_T(B) > 4.5$ GeV/c^2, $P_T(K) > 1.0$ GeV/c^2

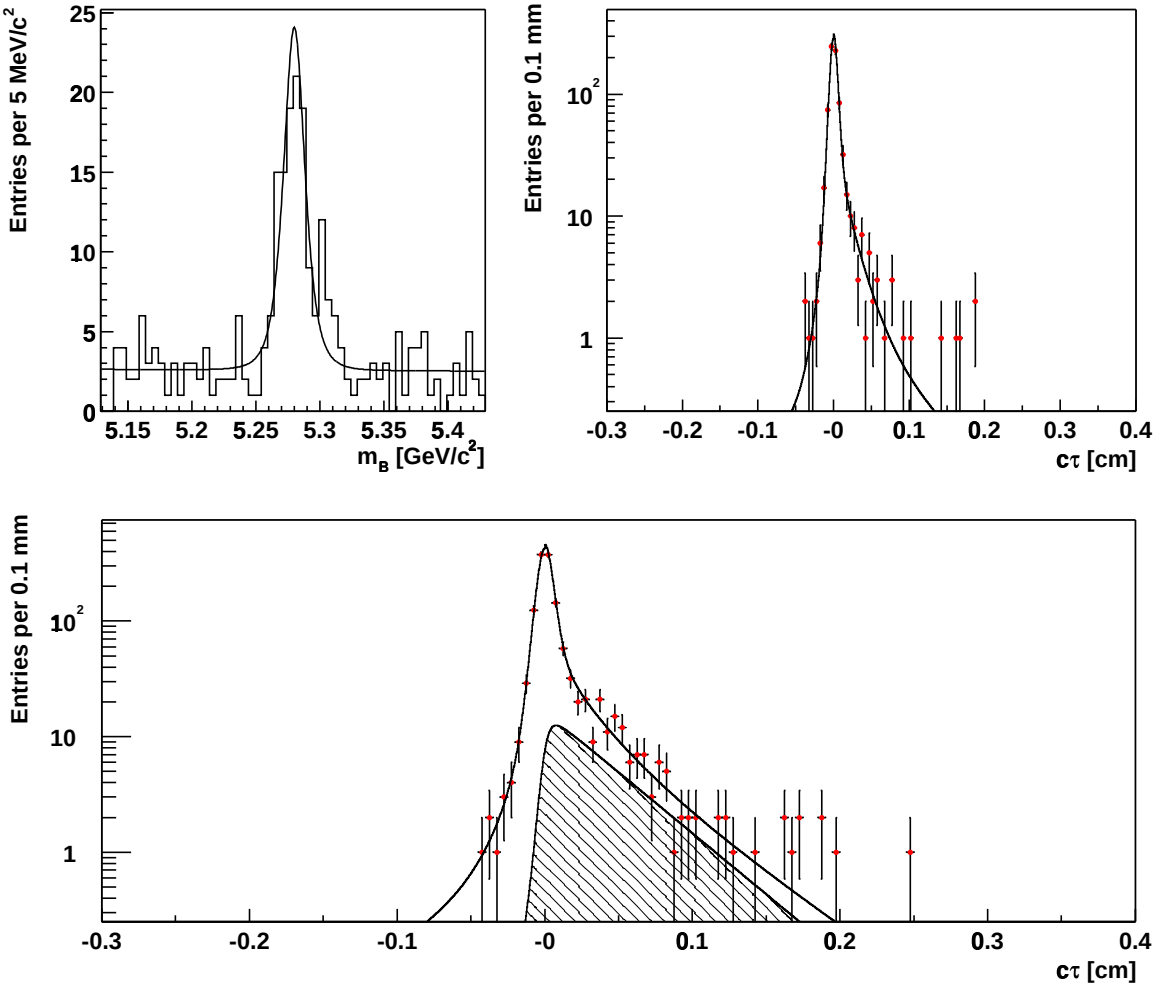

Figure 6.6: Mass distribution (top left), background $c\tau$ (top right) and $c\tau$ (bottom) distributions of reconstructed $B^0 \to J/\psi\ K^0_S$; $K^0_S \to \pi^+\pi^-$; $J/\psi \to \mu^+\mu^-$ decays.

parameter	value	error	parameter	value	error
M [GeV/c^2]	5.2800	0.0014	f_-	0.01081	0.00430
C_M	6.007	17.132	λ_- [μm]	448.37	166.34
s_m	1.1660	0.1490	f_+	0.11914	0.02792
$c\tau$ [μm]	411.65	41.11	λ_+ [μm]	201.31	42.55
s_λ	1.1040	0.0334	f_{++}	0.02755	0.02526
f_B	0.8980	0.0102	λ_{++} [μm]	615.80	263.41
τ [ps]	**1.373**	**0.137**	N_{Signal}	135.1	13.6

Table 6.6: Fit results of the decay channel $B^0 \to J/\psi\ K^0_S$; $K^0_S \to \pi^+\pi^-$; $J/\psi \to \mu^+\mu^-$.

6.1.7 RESULTS FOR THE DECAY CHANNEL $B^0 \to J/\psi\ K^{*0}$; $K^{*0} \to K^{\pm}\pi^{\mp}$; $J/\psi \to \mu^+\mu^-$

P_T cuts for smallest error of $c\tau$: $P_T(B) > 5.0$ GeV/c^2, $P_T(K) > 1.25$ GeV/c^2

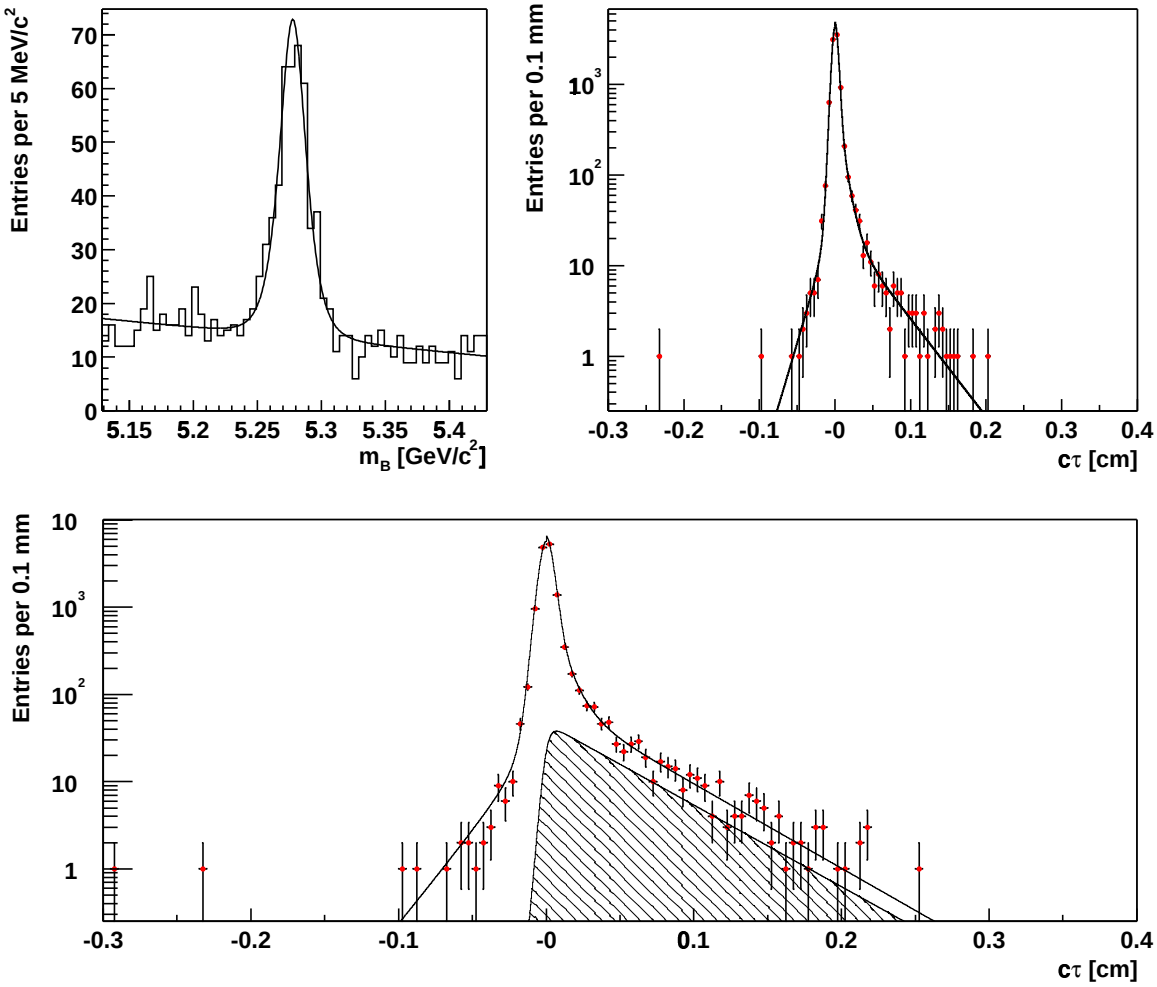

Figure 6.7: Mass distribution (top left), background $c\tau$ (top right) and $c\tau$ (bottom) distributions of reconstructed $B^0 \to J/\psi\ K^{*0}$; $K^{*0} \to K^{\pm}\pi^{\mp}$; $J/\psi \to \mu^+\mu^-$ decays.

parameter	value	error	parameter	value	error
M [GeV/c^2]	5.2777	0.0008	f_-	0.00879	0.001404
C_M	33.377	6.979	λ_- [μm]	208.73	26.16
s_m	1.3868	0.0977	f_+	0.10315	0.00666
$c\tau$ [μm]	464.04	24.98	λ_+ [μm]	84.26	6.27
s_λ	1.1563	0.0095	f_{++}	0.02683	0.00419
f_B	0.9689	0.0019	λ_{++} [μm]	427.52	43.12
τ [ps]	**1.548**	**0.083**	N_{Signal}	430.3	26.3

Table 6.7: Fit results of the decay channel $B^0 \to J/\psi\ K^{*0}$; $K^{*0} \to K^{\pm}\pi^{\mp}$ $J/\psi \to \mu^+\mu^-$.

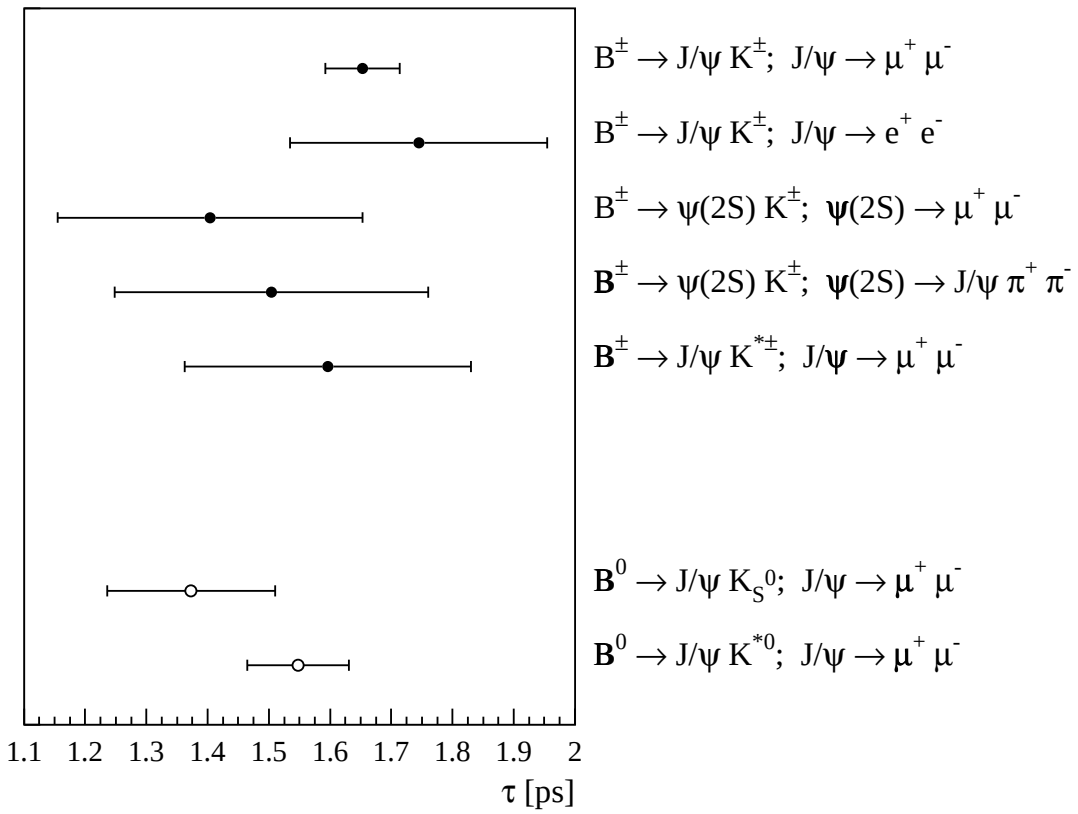

Figure 6.8: The measured lifetimes and corresponding statistical uncertainties for the individual 5 $B^{\pm}$ and 2 B^0 decay channels.

Figure 6.8 shows a comparison of the lifetime results and statistical uncertainties of the different decay channels. The results agree within statistical uncertainties.

Looking at tables 6.1 to 6.7 one observes that the measured B meson masses are slightly too low compared to the world average mass values [14]. This is due to the fact that certain – for a mass measurement necessary – systematic corrections [58] are not applied in this analysis. These small corrections do not play a role in the lifetime determination.

6.2 Results of the Combined Fits

In this section the results of the combined fits to the data of all decay channels of each B meson species are presented. Figures 6.9 and 6.10 show the combined $c\tau$ distributions of all $B^{\pm}$ and B^{0} candidates used to calculate the log-likelihood function (5.15). Tables 6.8 and 6.9 show the best fit values and uncertainties of the common fit parameters in the combined fits.

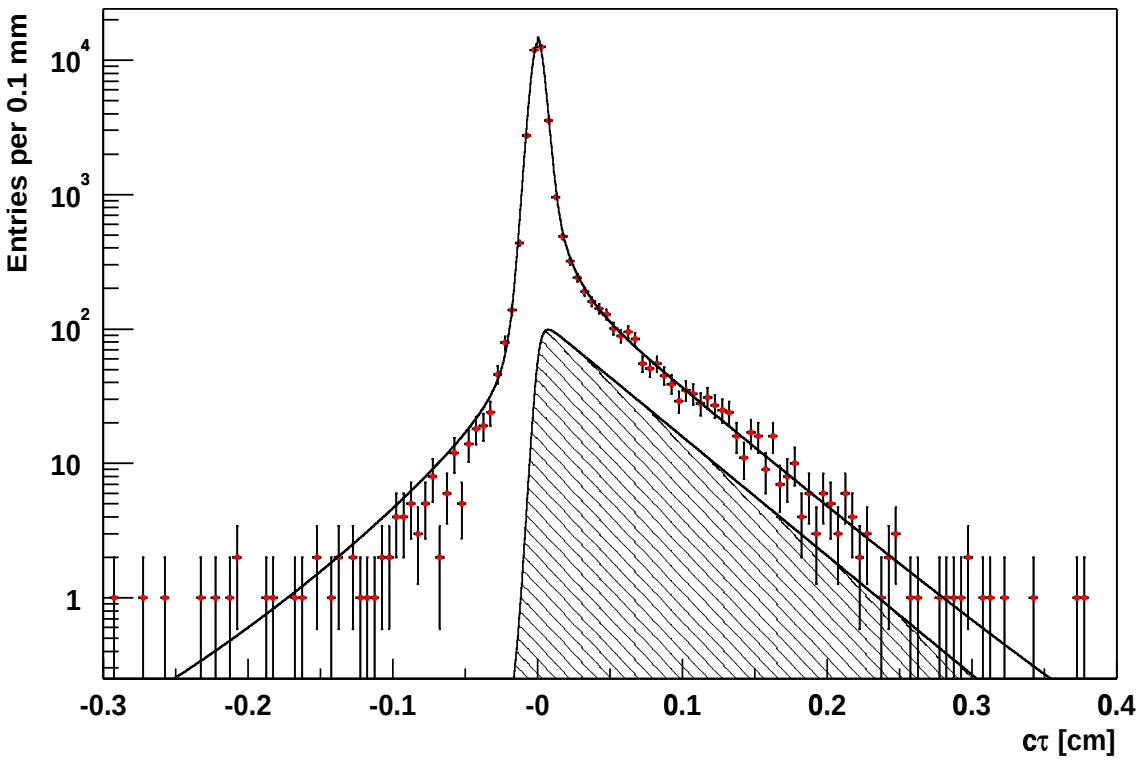

Figure 6.9: $c\tau$ distribution of all $B^{\pm}$ decay channels combined with the fitted function superimposed. The hatched area is the signal contribution.

parameter	value	error
decay length $c\tau$ [μm]	490.41	17.53
error scale factor s_{λ}	1.1702	0.0058
mean mass M	5.2770	0.0005
error scale factor s_m	1.1875	0.0408
mean lifetime τ [ps]	**1.636**	**0.058**
N_{Signal}	1182.4	43.2

Table 6.8: Best fit values and corresponding uncertainties of the common parameters in the fit to the combined $B^{\pm}$ decay channels. τ is the average $B^{\pm}$ meson lifetime $\tau = c\tau/c$. N_{Signal} is the total number of signal candidtes in the $B^{\pm}$ data samples.

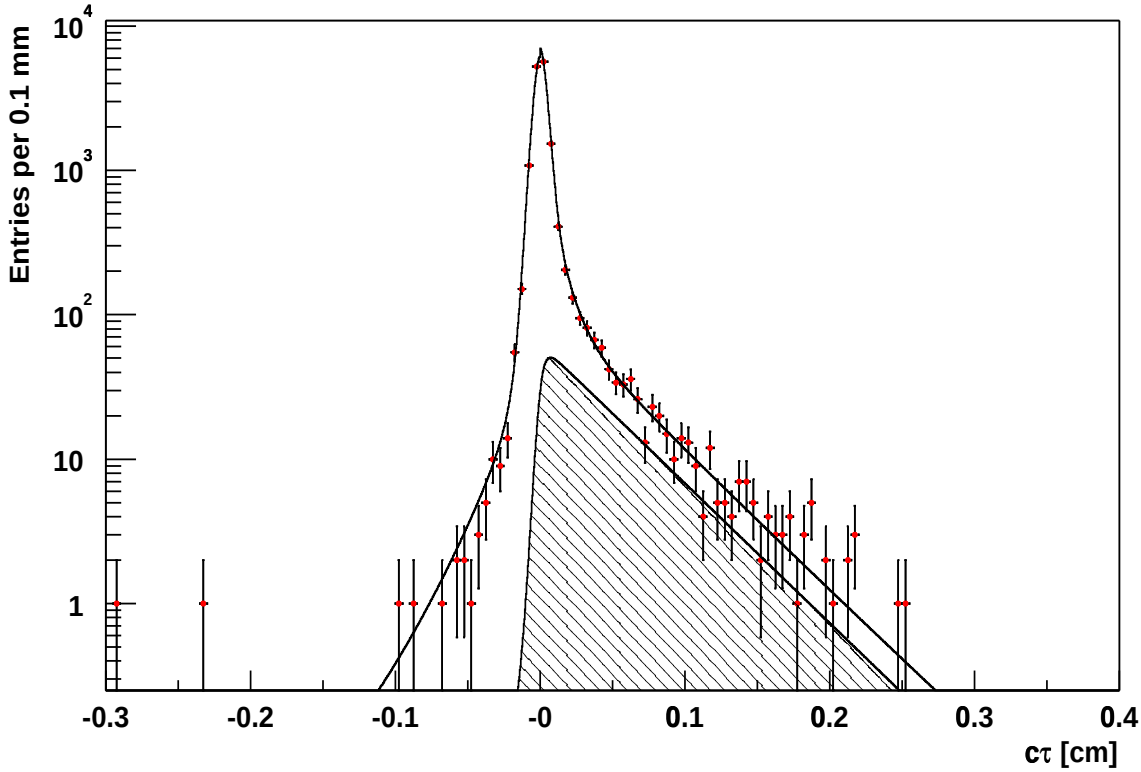

Figure 6.10: $c\tau$ distribution of all B^0 decay channels combined with the fitted function superimposed. The hatched area is the signal contribution.

parameter	value	error
decay length $c\tau$ [μm]	448.80	21.84
error scale factor s_λ	1.1526	0.0086
mean mass M	5.2778	0.0006
error scale factor s_m	1.3316	0.0688
mean lifetme τ [ps]	**1.497**	**0.073**
N_{Signal}	565.3	29.4

Table 6.9: Best fit values and corresponding uncertainties of the common parameters in the fit to the combined B^0 decay channels. τ is the average B^0 meson lifetime $\tau = c\tau/c$. N_{Signal} is the total number of signal candidtes in the B^0 data samples.

Figures 6.11 and 6.12 show the log-likelihood $\mathcal{L}$ as a function of $c\tau$ for the combined $B^\pm$ and B^0 decay channels, respectively. Figures 6.13 and 6.14 show 1 σ contour plots of the fitted decay length $c\tau$ versus fitted mass M. The fact that these ellipses are almost not sloped indicates that the correlation between the parameters $c\tau$ and M is very small.

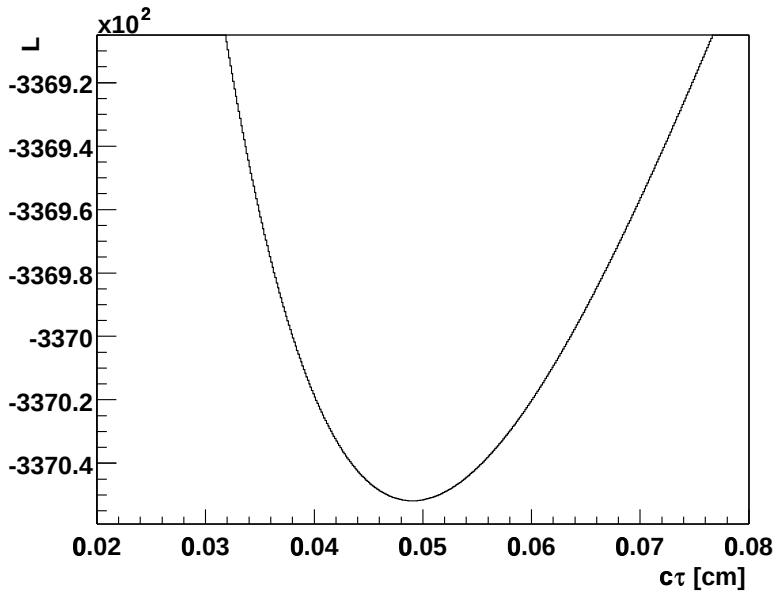

Figure 6.11: The log-likelihood value as a function of the decay length $c\tau$ for the $B^{\pm}$ combined fit.

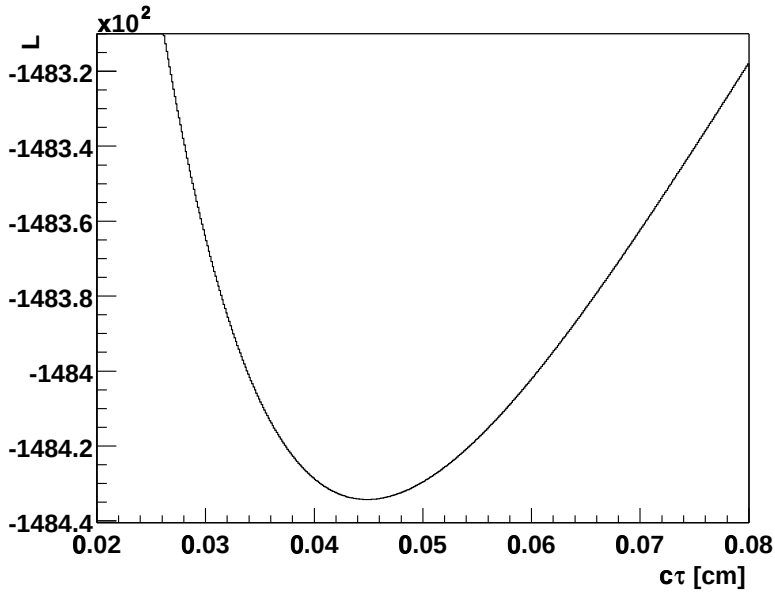

Figure 6.12: The log-likelihood value as a function of the decay length $c\tau$ for the B^0 combined fit.

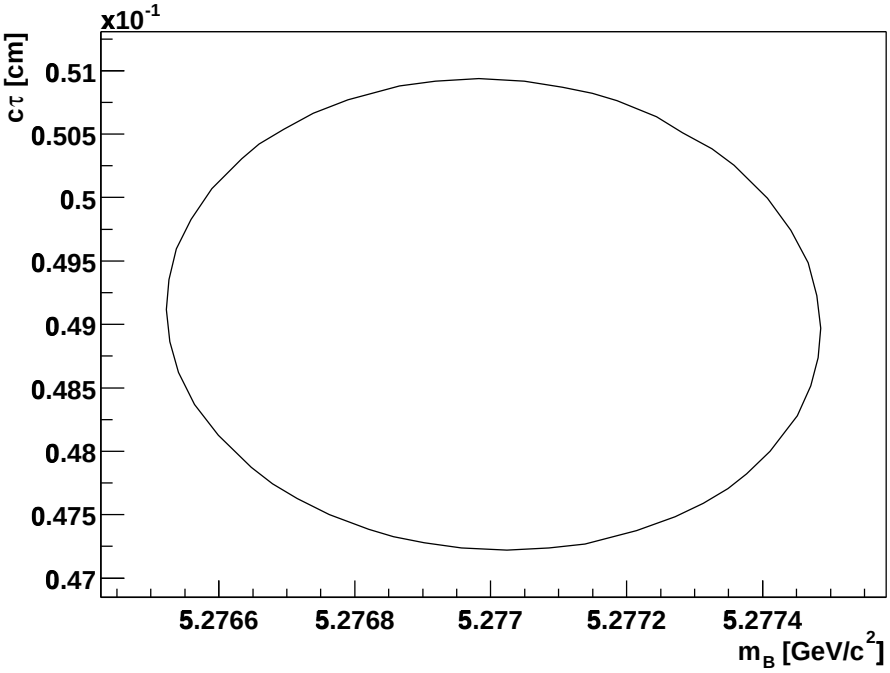

Figure 6.13: A 1 σ contour plot of the fitted decay length $c\tau$ versus the fitted mass M (m_B) for the $B^{\pm}$ combined fit.

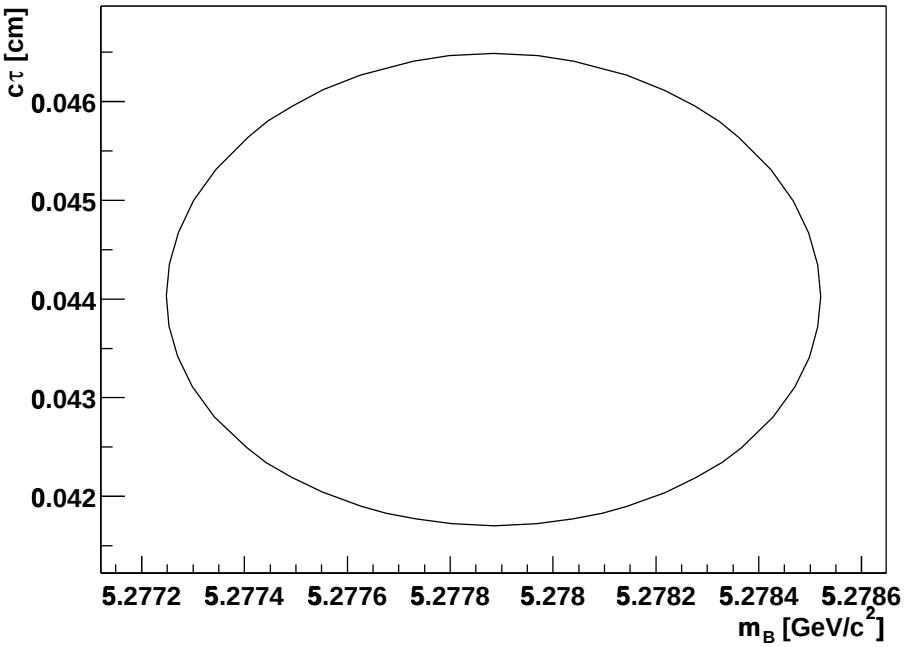

Figure 6.14: A 1 σ contour plot of the fitted decay length $c\tau$ versus the fitted mass M (m_B) for the B^0 combined fit.

6.3 Consistency Checks

In this section the stability of the results is examined when the mass range of in the fitting procedure or the P_T cuts on the B mesons and their decay kaons are varied. Results of the fits to B^+ and B^- data samples as well as B^0 and $\bar{B}^0$ data samples are compared.

6.3.1 Size of the Mass Window

As mentioned in section 5.5, B meson candidates within a relatively wide mass window of ± 150 MeV/c^2 around the world average B meson mass are used to calculate the log-likelihood functions. A possible effect of the size of the mass window and the sideband regions (see Figure 5.1) on the best fit decay length is studied for individual decay channels. Tables 6.10, 6.11 and 6.12 show the results for three different decay channels. In the first row of each table, the results with the actually used mass window size are stated. A correlation of the results with the size of the mass window is not observed. The advantage of using wide mass windows for the fits is in most cases the smaller statistical error and the better convergence of the fit.

masswindow	size of sidebands	$c\tau$ [μm]	N_{Signal}
$\pm$ 150 MeV/c^2	100 MeV/c^2	495.59 $\pm$ 18.73	905.7 $\pm$ 36.9
$\pm$ 130 MeV/c^2	80 MeV/c^2	496.30 $\pm$ 18.89	907.7 $\pm$ 39.3
$\pm$ 110 MeV/c^2	60 MeV/c^2	492.69 $\pm$ 19.03	903.5 $\pm$ 36.0
$\pm$ 90 MeV/c^2	40 MeV/c^2	487.46 $\pm$ 20.75	904.8 $\pm$ 40.6
$\pm$ 80 MeV/c^2	30 MeV/c^2	488.81 $\pm$ 19.46	881.1 $\pm$ 39.9

Table 6.10: Fitted decay length and number of signal candidates for different mass windows. Decay channel $B^\pm \to J/\psi\ K^\pm$; $J/\psi \to \mu^+\mu^-$.

masswindow	size of sidebands	$c\tau$ [μm]	N_{Signal}
$\pm$ 150 MeV/c^2	100 MeV/c^2	420.82 $\pm$ 74.70	56.7 $\pm$ 10.6
$\pm$ 130 MeV/c^2	80 MeV/c^2	422.85 $\pm$ 77.42	54.8 $\pm$ 10.8
$\pm$ 110 MeV/c^2	60 MeV/c^2	416.91 $\pm$ 75.86	56.1 $\pm$ 10.5
$\pm$ 90 MeV/c^2	40 MeV/c^2	419.76 $\pm$ 79.04	58.1 $\pm$ 12.2
$\pm$ 80 MeV/c^2	30 MeV/c^2	421.97 $\pm$ 79.57	56.0 $\pm$ 11.6

Table 6.11: Fitted decay length and number of signal candidates for different mass windows. Decay channel $B^\pm \to \psi(2S)\ K^\pm$; $\psi(2S) \to \mu^+\mu^-$.

masswindow	size of sidebands	$c\tau$ [μm]	N_{Signal}
$\pm$ 150 MeV/c^2	100 MeV/c^2	464.04 $\pm$ 24.98	430.3 $\pm$ 26.3
$\pm$ 130 MeV/c^2	80 MeV/c^2	463.98 $\pm$ 26.17	429.9 $\pm$ 26.6
$\pm$ 110 MeV/c^2	60 MeV/c^2	461.34 $\pm$ 27.37	426.1 $\pm$ 27.2
$\pm$ 90 MeV/c^2	40 MeV/c^2	460.47 $\pm$ 28.10	423.3 $\pm$ 29.5
$\pm$ 80 MeV/c^2	30 MeV/c^2	458.75 $\pm$ 27.94	422.4 $\pm$ 26.3

Table 6.12: Fitted decay length and number of signal candidates for different mass windows. Decay channel $B^0 \to J/\psi\ K^{*0}$; $K^{*0} \to K^{\pm}\pi^{\mp}$; $J/\psi \to \mu^+\mu^-$.

6.3.2 B^+ VS. B^- AND B^0 VS. $\bar{B}^0$ LIFETIMES

The fitting procedure is also performed seperately for B^+ and B^- meson candidates as well as B^0 and $\bar{B}^0$ meson candidates reconstructed in the decay channels $B^{\pm} \to J/\psi\ K^{\pm}$; $J/\psi \to \mu^+\mu^-$ and $B^0 \to J/\psi\ K^{*0}$; $K^{*0} \to K^{\pm}\pi^{\mp}$; $J/\psi \to \mu^+\mu^-$ respectively. The results are shown in table 6.13. Within the statistical uncertainties, the best fit decay lengths of B^+ and B^- mesons as well as B^0 and $\bar{B}^0$ mesons are compatible.

B meson species	$c\tau$ [μm]	N_{Signal}
B^+	513.06 $\pm$ 26.62	461.2 $\pm$ 25.1
B^-	473.78 $\pm$ 28.90	444.5 $\pm$ 26.4
B^0	448.80 $\pm$ 35.21	221.6 $\pm$ 18.8
$\bar{B}^0$	486.04 $\pm$ 40.94	208.8 $\pm$ 17.3

Table 6.13: B versus $\bar{B}$ comparison of best fit decay lengths and number of signal candidates. The errors are statistical.

6.3.3 DEPENDENCE ON MOMENTUM CUTS

In this section the dependence of the fit results on the P_T thresholds applied on B meson candidates and decay kaons is examined. As mentioned before, these thresholds are choosen for smallest statistical errors. Figures 6.15, 6.16 and 6.17 show the best fit decay length $c\tau$ of three different decay channels for different thresholds. The left histogram shows the dependence on the $P_T(B)$ threshold with the $P_T(K)$ threshold fixed to the value actually used for the particular data sample. The right histogram shows the dependence on the $P_T(K)$ threshold with the $P_T(B)$ threshold fixed to the actually used value. For some P_T values, no stable fit could be achived. The corresponding points in the histograms are therefore missing. The best fit values of $c\tau$ vary only slightly within errors with changing P_T-thresholds.

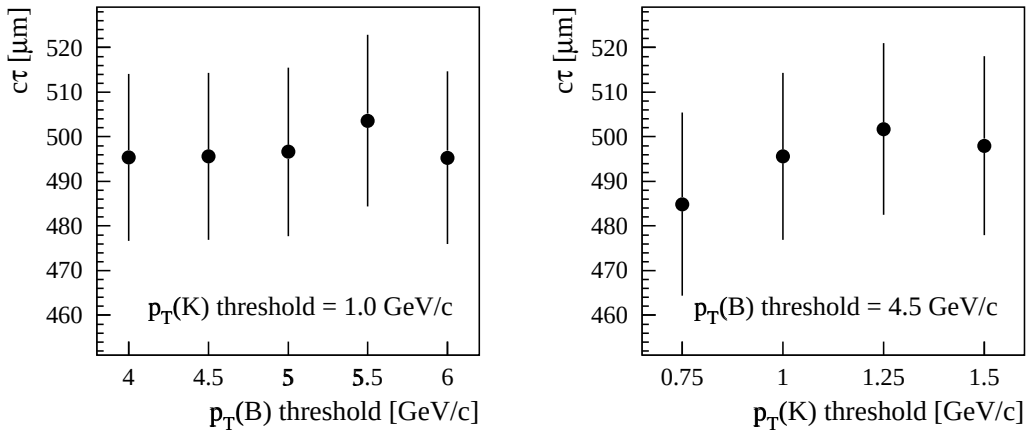

Figure 6.15: The dependence of the best fit decay length on the P_T thresholds of the B meson candidates (left) and the decay kaon (right). Decay channel $B^{\pm} \rightarrow J/\psi\ K^{\pm}$; $J/\psi \rightarrow \mu^+\mu^-$.

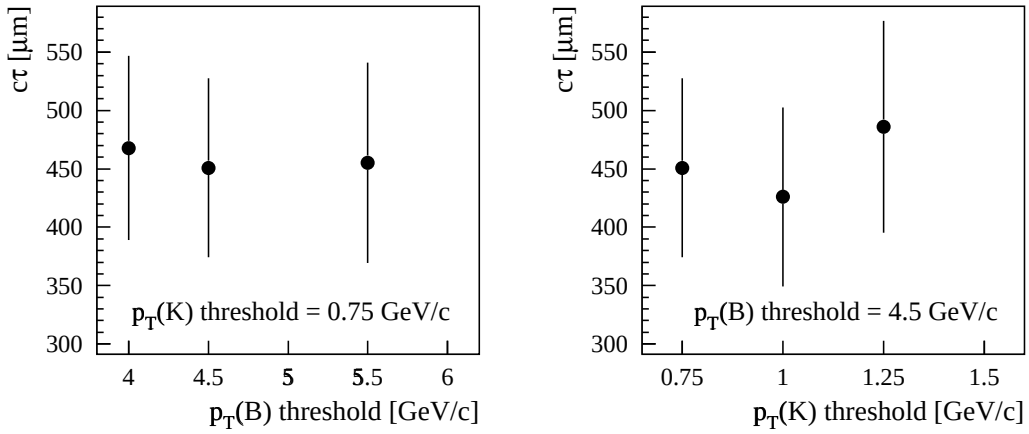

Figure 6.16: The dependence of the best fit decay length on the P_T thresholds of the B meson candidates (left) and the decay kaon (right). Decay channel $B^{\pm} \rightarrow \psi(2S)\ K^{\pm}$; $\psi(2S) \rightarrow \mu^+\mu^-$.

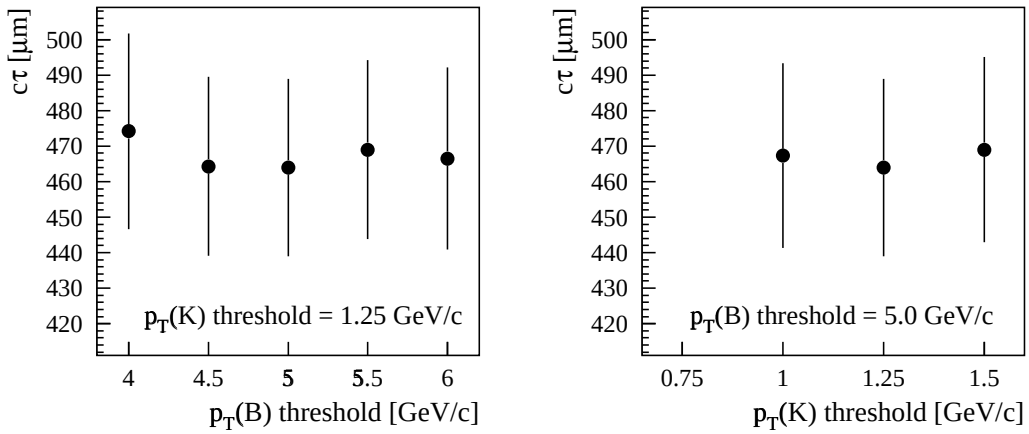

Figure 6.17: The dependence of the best fit decay length on the P_T thresholds of the B meson candidates (left) and the decay kaon (right). Decay channel $B^0 \rightarrow J/\psi\ K^{*0}$; $K^{*0} \rightarrow K^{\pm}\pi^{\mp}$; $J/\psi \rightarrow \mu^+\mu^-$.

Chapter 7

Systematic Uncertainties

In this chapter the sources of systematic uncertainties are described and their magnitudes are estimated. Two sources of systematic uncertainties apply to lifetime measurements in general. These are the residual misalignment of the silicon vertex detector and the trigger bias. The corresponding uncertainties are taken from earlier analysis. All other sources are examined in this analysis.

7.1 Background parameterizations

Unlike the parameterization of the $c\tau$ distribution from signal events (5.12) which has a physics justification (the decay of the B mesons), the parameterization of the background $c\tau$ distribution (5.13) is more or less arbitrary (one of the two positive exponential tails is justified by the known background of sequential B-meson decays). In order to determine an uncertainty due to the possibly wrong background parameterization, the fractions and and length scales of the three exponential functions are varied by $\pm$ 1 σ of the best fit values and fixed in the fit. The resulting shift of the best fit decay length with respect to the result of the fit with all parameters floating is < 4 μm for both, $B^{\pm}$ and B^0. As expected, changing the fraction or the length scale of the negative exponential and fixing it in the fit does not effect the best fit decay length significantly. By changing the fraction f_- or the length scale λ_- by a factor of 2, the resulting shift of the best fit decay length is less than 1 μm. For individual decay channels, the fits are also performed with only one positive exponential function in the background parameterization. A single positive exponential function can clearly not describe the data satisfactorily. The observed shifts of the best fit decay length are < 4 μm for most decay channels. Only for the decay channel $B^0 \to J/\psi\ K^{*0}$, the shift is ≈ 24 μm. However, the match of the fitted function to the data is extraordinary bad in this particular case. Taking the results stated in this section into account, 4 μm are a reasonable systematic uncertainty due to a possible wrong background parameterization.

7.2 NON-GAUSSIAN TAILS OF THE RESOLUTION FUNCTION

It is assumed that the resolution function is a pure Gaussian function and that the sigma of this Gaussian is equal to the measured error of the proper decay length for each event. A good place to look at to find non-Gaussian tails of the resolution function is the negative $c\tau$ region of the background-subtracted $c\tau$ distributions (Figures 7.1 and 7.2 (a)). There is no evidence that the negative part of the signal $c\tau$ distributions is not well described by the signal function. Figures 7.1 and 7.2 (b) show the background-subtracted $c\tau$ distributions with the fitted signal function also subtracted. A second, very wide Gaussian function with a sigma fixed to 100 μm is introduced in the fit to describe possible tails of the resolution function. This fixed-width Gaussian function is illustrated in the histograms. (The Gaussian is drawn as an illustration, it is not fitted.) The Gaussian (5.8) is therefore replaced by the following expression:

$$f_{tail} \cdot G_2 + (1 - f_{tail}) \cdot G \tag{7.1}$$

where G_2 is the newly introduced fixed-width Gaussian function and G is the original Gaussian. f_{tail}, the fraction of the fixed-width Gaussian function, is a free parameter in the fit. Table 7.1 shows the results of the fitting procedures with the f_{tail} parameter floating in the fit and compares them with the results of the fits without the second Gaussian. f_{tail} is compatible with zero in both cases. Nevertheless, the observed shifts of the best fit decay lengths are considered as systematic uncertainties.

B meson	without 2nd Gaussian	with 2nd Gaussian	shift	f_{tail}
$B^{\pm}$	490.4 μm	484.4 μm	6 μm	(1.5 ± 1.8) %
B^0	448.8 μm	440.3 μm	8.5 μm	(2.1 ± 1.4) %

Table 7.1: Results of the combined lifetime fits without and with a second Gaussian function describing tails of the resolution function.

7.3 FITTING PROCEDURE BIAS

A possible bias due to the fitting procedure is studied by fitting a convolution of a Gaussian and an exponential function (5.12) to Monte Carlo (MC) generated pure signal data samples. The number of events in these samples is equal to the number of signal candidates in the measured data samples. Several hundred MC data samples are used. The shifts of the mean of the fitted lifetimes with respect to the true value of the lifetime used to generate the samples is a good indication of the bias due to the fitting procedure itself. These shifts are equal to 1.2 ± 0.9 μm and 0.5 ± 1.3 μm for charged and neutral B mesons respectively. These values are compatible with zero. Nevertheless, a systematic uncertainty of 1 μm is assigned due to the possible existence of a bias for both cases, $B^{\pm}$ and B^0.

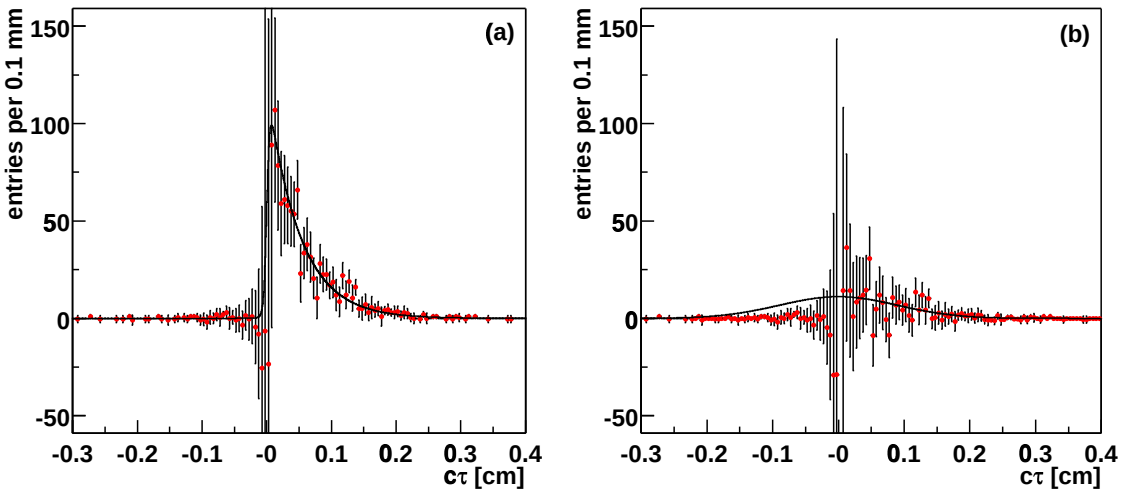

Figure 7.1: a) Background subtracted $c\tau$ distribution of $B^{\pm}$ candidates with the fitted signal contribution superimposed. b) Histogram (a) with subtracted fitted signal contribution. The Gaussian function is an illustration, not a fitted function.

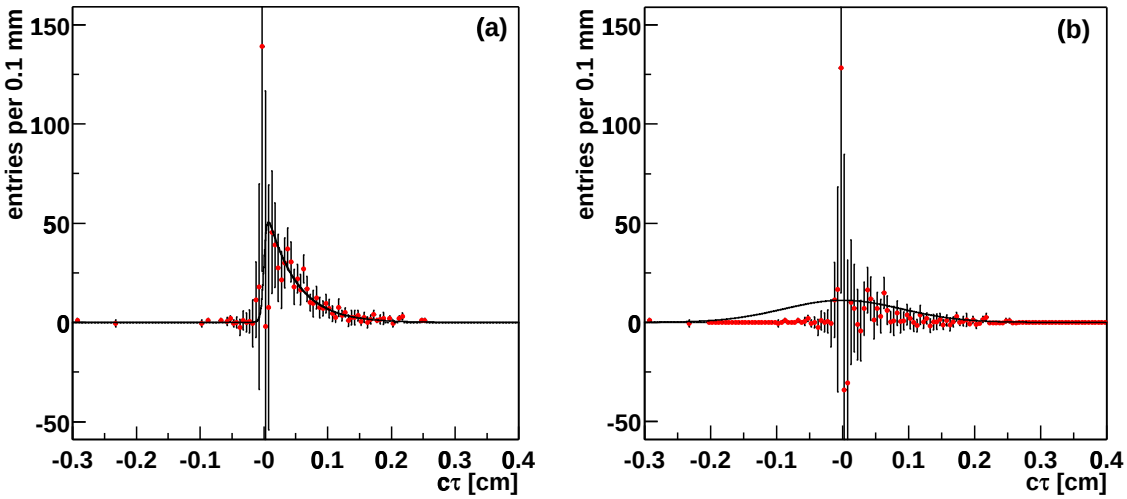

Figure 7.2: a) Background subtracted $c\tau$ distribution of B^0 candidates with the fitted signal contribution superimposed. b) Histogram (a) with subtracted fitted signal contribution. The Gaussian function is an illustration, not a fitted function.

7.4 BIAS DUE TO THE BEAM POINTING CONSTRAINT IN THE DECAY CHANNEL $B^0 \to J/\psi K_S^0$

As mentioned in section 4.4, the B meson momentum was required to point back to the beam for the decay channel $B^0 \to J/\psi K_S^0$ only. A possible effect of this pointing constraint was studied similar to the fitting procedure bias. A convolution of a Gaussian and an exponential function (5.12) was fitted to several hundred Monte Carlo data samples. The data samples are generated with and without the pointing

constraint in the reconstruction procedure. The mean decay length of the samples reconstructed with pointing constraint is shifted by $+1.6 \pm 2.0$ μm. Since the decay channel $B^0 \to J/\psi K_S^0$ contributes only $\approx 25\%$ to the whole B^0 data and the shift is compatible with zero, no extra systematic error is assigned to this effect.

7.5 Residual misalignment of the SVX

When tracks were used to align the detector, the radius of the fourth SVX layer was kept constant while the radial positions of the three inner layers were allowed to float. Significant shifts of the order of 80 μm between the optical survey alignment constants and the track based alignment constants were observed. A study of the possible shift of the lifetime result was done for an older analysis [59]. The observed shift of the lifetime result was 0.3%. Therefore, the systematic uncertainty due to the SVX misalignment is estimated to 1.5 μm.

7.6 Trigger Bias

Any variation of the CFT trigger efficiency with the magnitude of the track impact parameter[1] would bias the lifetime distribution. The CFT impact parameter resolution is > 50 times that of the SVX and 3 times the average displacement of secondary tracks from B meson decays. Hence, no lifetime bias is expected. A study of the CFT trigger efficiency was performed [59] and no variation of the trigger efficiency with the impact parameter was found resulting in a negligible effect on the lifetime distribution.

7.7 Total Systematic Uncertainty

Table 7.2 summarizes all sources of systematic uncertainties.

Description	Contribution	
	$B^\pm$	B^0
Background parameterizations	4 μm	4 μm
Non-Gaussian tails of the resolution function	6 μm	8.5 μm
Fitting procedure bias	1 μm	1 μm
Residual misalignment of the SVX detector	1.5 μm	1.5 μm
Total systematic uncertainty	7.4 μm	9.6 μm
	0.025 ps	0.032 ps

Table 7.2: Summary of the systematic uncertainties.

[1] The track impact parameter is defined as the closest approach of the track helix to the beam axis measured in the plane perpendicular to the beam.

Chapter 8

Measurement of the Λ_B Lifetime

The B reconstruction software described in Chapter 4 can also be used to find decays of Λ_B baryons into J/ψ and Λ where the Λ decays into $p\ \pi^-$.
The reconstruction of $\Lambda \to p\ \pi^-$ is similar to the $K^{*0}(\overline{K^{*0}}) \to K^{\pm}\ \pi^{\mp}$ reconstruction. Track pairs of opposite charge are searched for and both mass assignment hypotheses, $p\ \pi^-$ and $\pi^+\ \bar{p}$, are initially retained. A vertex constraint fit of the two tracks is performed and the χ^2 probability is required to be $> 0.1\%$. Vertices with an invariant mass of ± 10 MeV/c^2 around the world average Λ mass of 1.11568 GeV/c^2 [14] are considered Λ candidates.
Λ_B candidates are reconstructed in the same way as $B^0 \to J/\psi\ K^0_S$ decays. The J/ψ vertex and the Λ vertex are fitted simultaneously. Mass constraints are applied on both vertices while the momentum vector of the Λ is required to point back to the J/ψ decay vertex. An overall χ^2 probability of at least 1% is required for this simultaneous fit.
Multiple candidates (duplicates) in the mass region of $\pm$ 150 MeV/c^2 are treated in the same way as for the decay channel $B^0 \to J/\psi\ K^{*0}$. Duplicates arising from the $p - \pi^-$ mass assignment ambiguity are removed by choosing the candidate with the Λ mass closest to the world average mass. Of all other candidates, the one with the highest χ^2 probability from the Λ_B global fit is selected.
The fitting procedure to determine the average lifetime is exactly the same as for the individual B meson data samples, described in Chapter 5. It was performed for different transverse momentum thresholds for the Λ_B and the Λ. The smallest statistical uncertainty is achieved with thresholds of $p_T(\Lambda_B) > 4.0$ GeV/c and $p_T(\Lambda) > 1.25$ GeV/c. The results of the three fitting steps, the fits to the mass distribution, background $c\tau$ and overall $c\tau$ distributions are shown in Figure 8.1. The hatched area in the bottom histogram denotes the signal contribution. The best fit parameters are summarised in Table 8.1. With 38 $\pm$ 11 candidates, the Λ_B lifetime is found to be

$$\tau_{\Lambda_B} \ = \ 1.22 \ \pm \ 0.36 \text{ ps}$$

where the error is statistical only. This is the first measurement of the Λ_B lifetime using this exclusive decay channel. The statistical significance, however, is still low.

With the expected integrated luminosity of 2 fb^{-1} for the first two years of the Tevatron Run II, the $\Lambda_B \to J/\psi\ \Lambda$ data sample will contain at least 2500 candidates resulting in a statistical uncertainty smaller by a factor of ≈ 8 compared to this measurement.

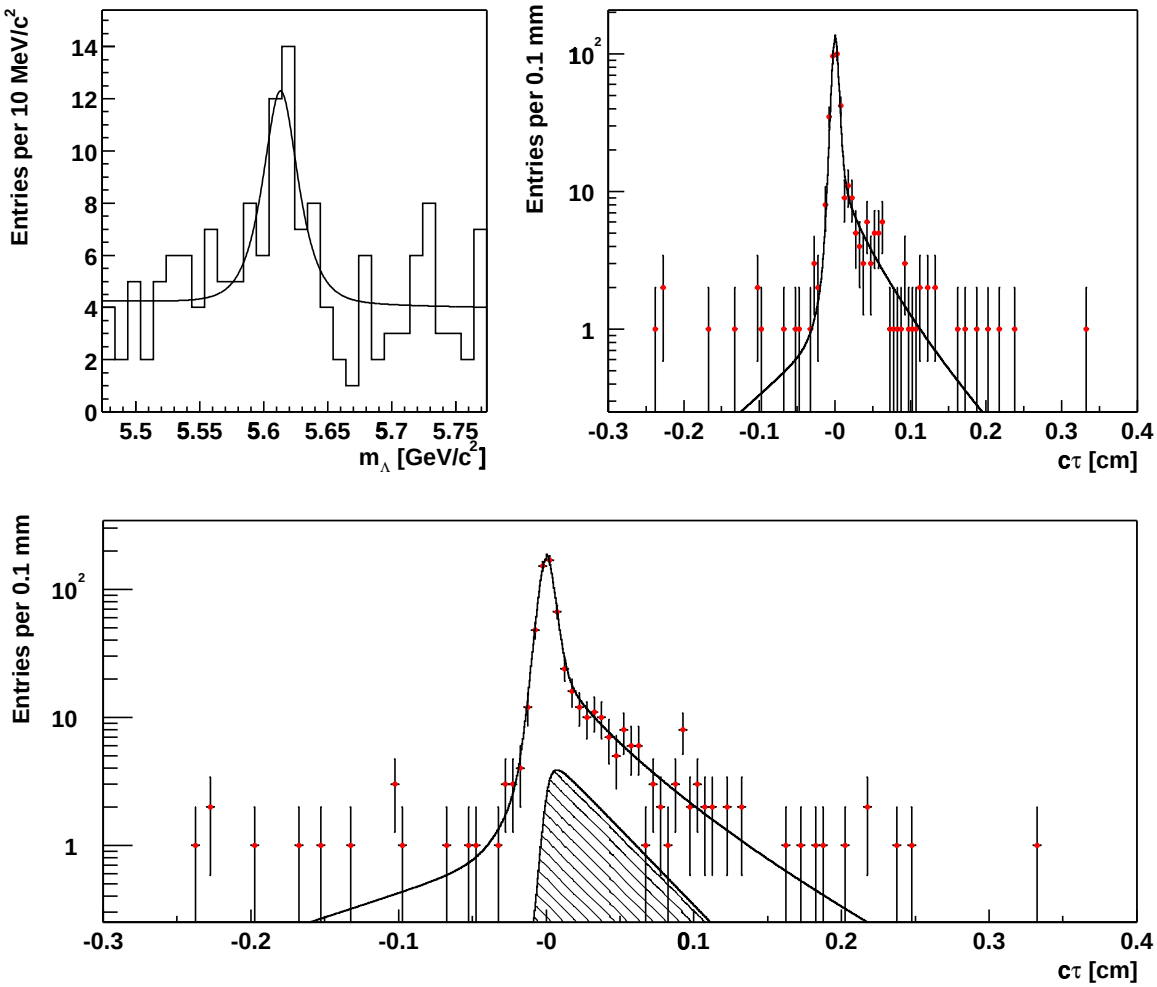

Figure 8.1: Mass distribution (top left), background $c\tau$ (top right) and $c\tau$ (bottom) distributions of reconstructed $\Lambda_B \to J/\psi\ \Lambda$; $J/\psi \to \mu^+\mu^-$, $\Lambda \to p\ \pi^-$ decays.

parameter	value	error	parameter	value	error
M [GeV/c^2]	5.6132	0.0037	f_-	0.03923	0.01006
C_M	7.014	19.460	λ_- [μm]	1145.10	255.92
s_m	2.0946	0.5020	f_+	0.11313	0.12752
$c\tau$ [μm]	364.73	108.02	λ_+ [μm]	298.68	187.31
s_λ	1.1609	0.0523	f_{++}	0.13102	0.12946
f_B	0.9395	0.0176	λ_{++} [μm]	675.71	246.08
τ [ps]	**1.22**	**0.36**	N_{Signal}	38.1	11.1

Table 8.1: Fit results of the decay channel $\Lambda_B \to J/\psi\ \Lambda$; $J/\psi \to \mu^+\mu^-$, $\Lambda \to p\ \pi^-$

Chapter 9

Conclusion and Final Results

In this analysis a new measurement of the B meson lifetime using fully reconstructed B decays has been performed. The lifetime was measured individually for different decay channels including $J/\psi \to e^+e^-$ final states for the first time. All results agree with each other within the statistical uncertainties. Contrary to the previous CDF measurement [59], a simultaneous fit of lifetime and mass was performed which also takes the lifetime distribution of background events under the mass peak into account. To determine the average $B^\pm$ and B^0 lifetimes, combined log-likelihood fits of five $B^\pm$ decay channels and two B^0 decay channels were performed in which the background mass and lifetime distributions were parameterized differently for each decay channel. The results of the combined fits are as follows:

$$\tau(B^\pm) = 1.636 \ \pm \ 0.058 \ (stat.) \ \pm \ 0.025 \ (syst.) \text{ ps}$$
$$\tau(B^0) \ = 1.497 \ \pm \ 0.073 \ (stat.) \ \pm \ 0.032 \ (syst.) \text{ ps}$$

The result of the lifetime ratio is therefore:

$$\frac{\tau(B^\pm)}{\tau(B^0)} \ = 1.093 \ \pm \ 0.066 \ (stat.) \ \pm \ 0.029 \ (syst.) \text{ ps}$$

in good agreement with the theoretical predictions. The systematic uncertainty stated for the lifetime ratio includes all contributions to the $B^\pm$ and B^0 systematic uncertainties and is therefore a conservative estimate. Figures 9.1, 9.2 and 9.3[1] show the results in comparison with other experiments and older CDF results as well as the world average values as calculated by the CERN B lifetimes working group [60]. The results are in good agreement with the world average values and other measurements. Compared to the previous exclusive CDF measurement, the statistical uncertainty of this measurement is 17 – 18 % smaller. The systematic uncertainty however is slightly larger. In this analysis, a possible wrong background parameterization is considered as an additional source of systematic uncertainties.

[1]The PAW macro used to create these plots is taken from [60].

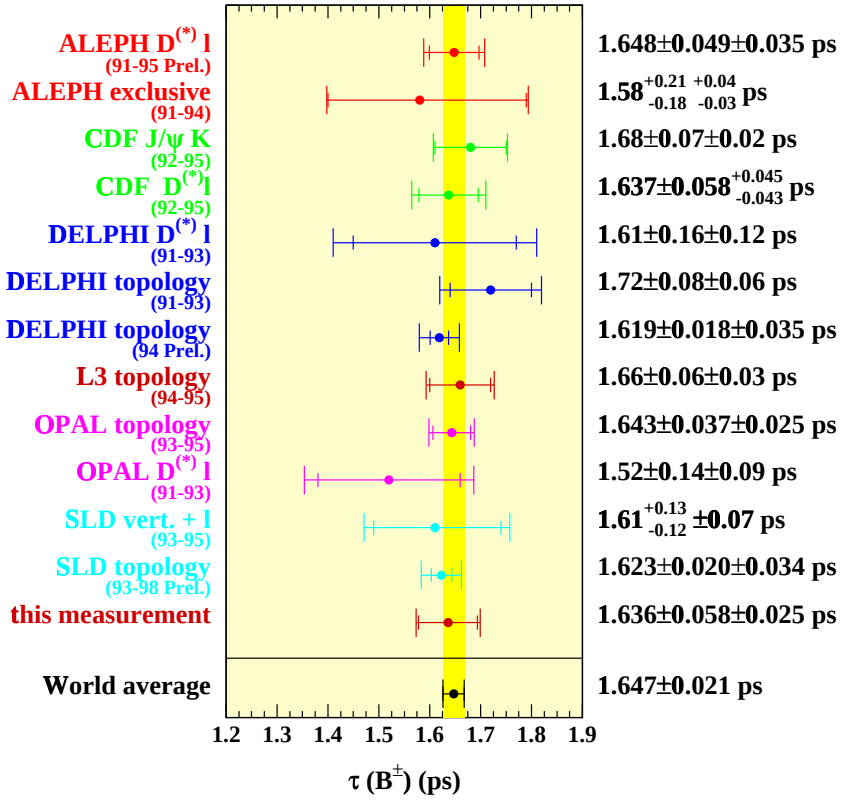

Figure 9.1: Comparison of the measured $B^{\pm}$ lifetime with other measurements and the world average value.

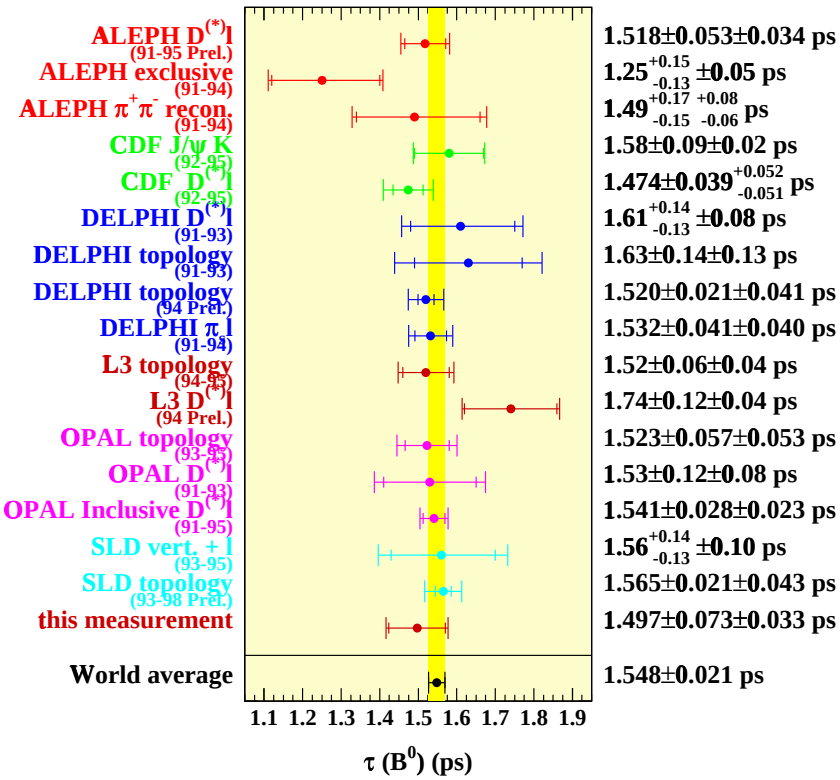

Figure 9.2: Comparison of the measured B^0 lifetime with other measurements and the world average value.

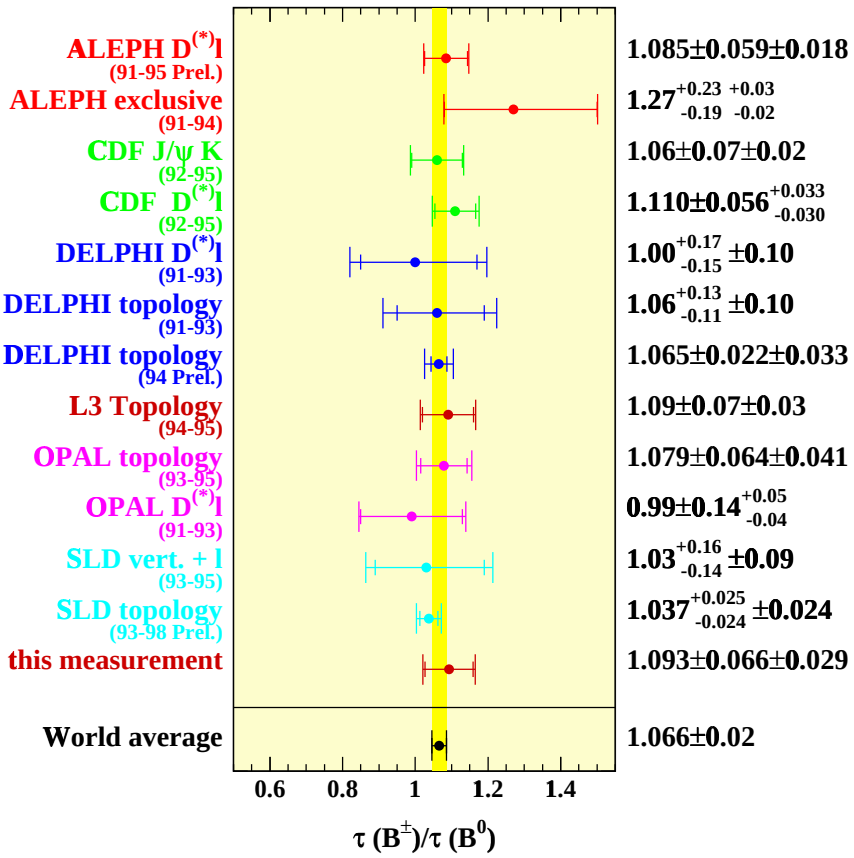

Figure 9.3: Comparison of the measured lifetime ratio with other measurements and the world average value.

Chapter 10

Future Prospects

The Fermilab accelerator complex underwent recently a major upgrade for higher luminosity and center-of-mass energy. The stated goal is to deliver 2 fb^{-1} integrated luminosity at $\sqrt{s} = 2.0$ TeV to the experiments within 2 years (Run IIa)[1] The instantaneous luminosity will reach $2 \cdot 10^{32}$ cm^{-2} s^{-1}. The higher luminosity compared to Run I is mainly achieved by replacing the old 'Main Ring' by the 'Main Injector' which will provide much higher proton intensity on the antiproton production target. The bunch spacing of the Tevatron beams will change from 3500 ns during Run I to initially 396 ns and later 132 ns during Run II. In order to handle the higher luminosities and shorter bunch spacing, the CDF experiment was also upgraded [71] within the last years. Figure 10.1 shows the upgraded detector for Run II.
The front-end electronics of all detector components is designed to handle the 132 ns beam crossing period. The trigger system and data acquisition system allow much higher data rates compared to Run I. A track trigger at Level 1 with transverse momenta as low as 1.5 GeV/c and a secondary vertex trigger at Level 2 allow to trigger on purely hadronic B decays.
The existing scintillator-based central calorimeters continue to perform well in Run II. The gas calorimeters in the pseudorapidity region $|\eta| > 1$ are replaced by new scintillating tile plug calorimeters. The changes in the muon systems represent incremental improvements. Gaps in the azimuthal coverage of CMP and CMX systems are closed. The forward muon system is replaced by the new Intermediate Muon System (IMU) which covers the region $1 < |\eta| < 1.5$. A more detailed description of calorimeter and muon system upgrades is given in [71]. A time-of-flight (TOF) system [63] consisting of 216 scintillator bars and mounted inside the solenoid coil will allow $K^{\pm}/\pi^{\pm}$ separation especially for low-P_T tracks.
The new tracking system is the upgrade most relevant to B physics. The new drift chamber, the Central Outer Tracker (COT), has been designed to cope with the short interbunch time. The size of the drift cells is roughly 4 times smaller than in the CTC. The usage of a faster gas reduces the drift time by another factor of two, down to 100 ns. The old SVX detector is replaced by a new, much more sophisti-

[1] It is planed to run the Tevatron and the detectors as long as possible and collect another 10 fb^{-1} or more before the Large Hadron Collider (LHC) at CERN turns on.

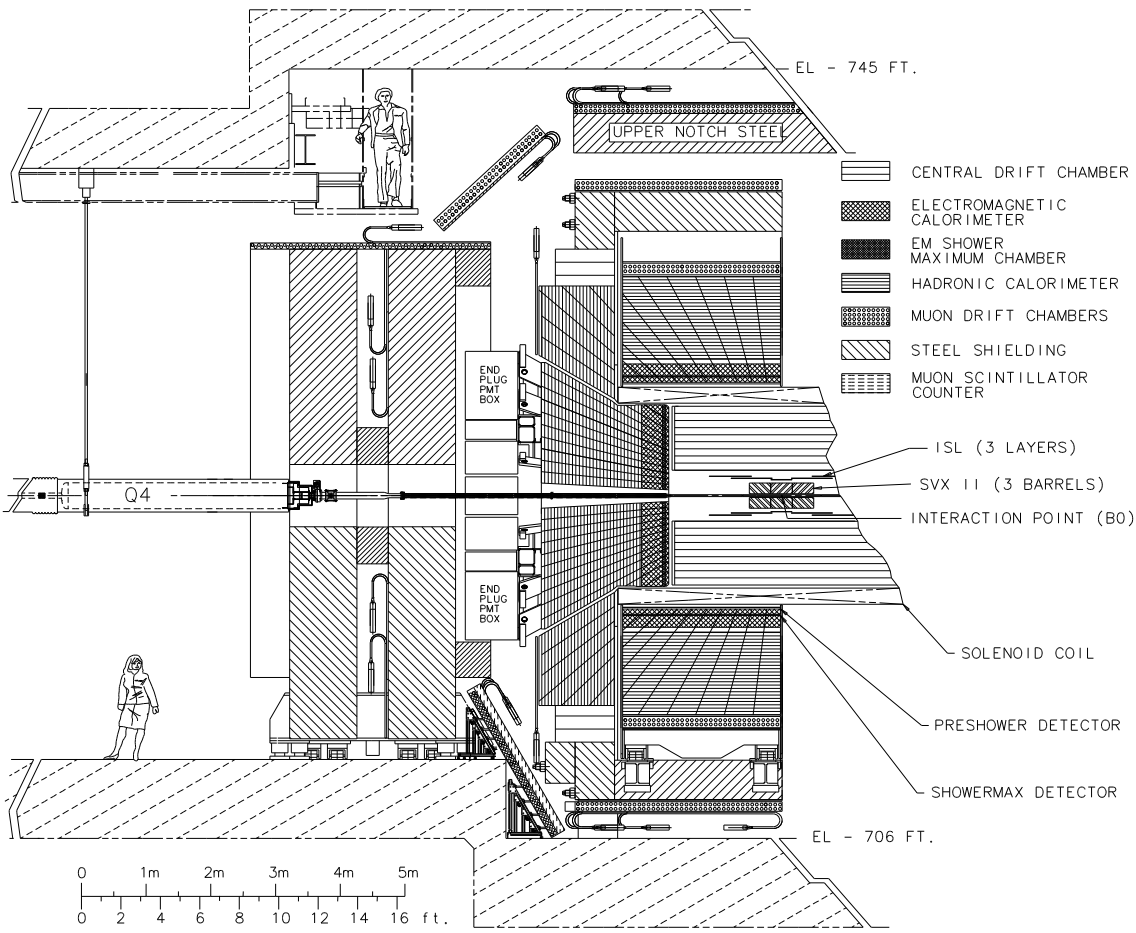

Figure 10.1: Elevation view of one half of the CDF II detector.

cated silicon tracking system consisting of the SVXII detector and the Intermediate Silicon Layers (ISL). SVXII and ISL use double-sided silicon strip sensors and provide 3D information. An additional layer of single-sided silicon strip sensors (Layer 00) is mounted directly on the beampipe at a distance of only 1.6 cm to the beam. A sketch of the SVXII and ISL detectors is shown in Figure 10.2.

SVXII alone covers $\approx 2.5\sigma$ of the luminous region. The additional silicon layers of the ISL extend the track finding capabilities to $|\eta| < 2$ in pseudorapidity. SVXII is 87 cm long and consists of 5 layers of silicon strip sensors at radii between 2.7 and 10.7 cm. z information is provided by 2 layers with 1.2° stereo angle and 3 layers with 90° angle of the z-side strips with respect to the beamline. ISL is 195 cm long and consists of two sensor layers mounted at radii of 20 cm and 28 cm respectively. Both layers provide z-coordinate measurements with 1.2° stereo strips.

The readout chips (SVX3, revision D [62][71]) used for Layer 00, SVXII and ISL are significantly more complex than the SVX chip from Run I to provide deadtime-less readout with Level 1 trigger rates up to 50 kHz. The SVX3 chip is a mixed analog–digital CMOS integrated circuit. It has 128 parallel input channels with amplifiers, integrators and 46 cell analog pipelines. Up to 4 groups of pipeline cells can be marked for digitisation and readout by Level 1 trigger signals. The digital

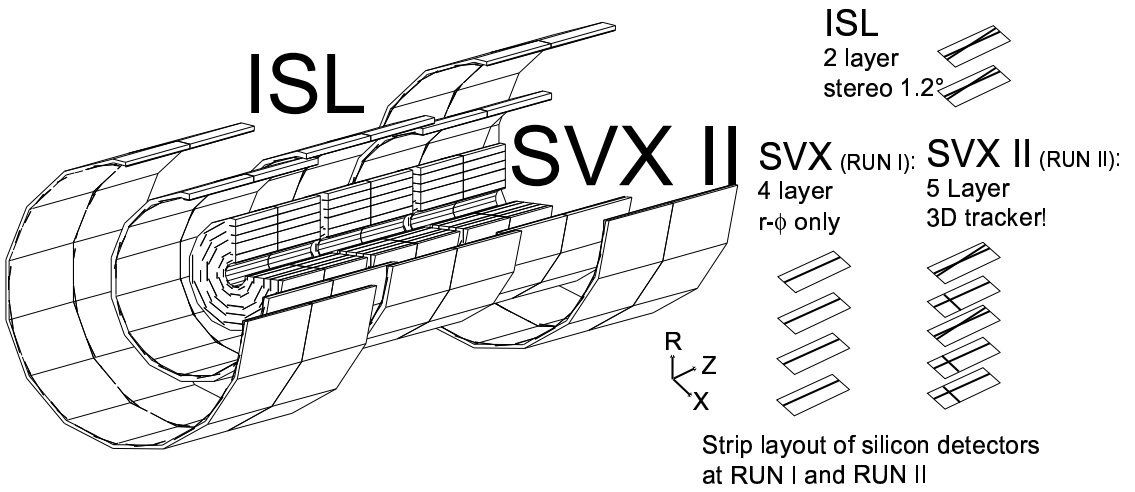

Figure 10.2: Isometric view of the layout of SVXII and ISL. The diagrams at the right side compare the tracking measurements of SVXII and ISL to those made by the SVX. From [61].

part of the chip consists of the pipeline logic, 8-bit Wilkinson ADCs[2] and a readout FIFO[3]. The chip is programmable for different collider running conditions (e.g. 132 ns and 396 ns bunch spacing) and capacitance loads from 10 to 35 pF at the inputs. With Layer 00, SVXII and ISL, CDF has the largest silicon tracking system used at a particle collider so far. It allows stand-alone tracking in three dimensions. The for B physics critical track impact parameter resolution is expected to be better than 30 μm [63] for tracks with a transverse momentum > 1 GeV/c.
The contributions of the University of Karlsruhe to the tracking system upgrade comprise the mounting fixtures used to assemble ISL ladders and modules[4], the evaluation of prototype sensors, quality control of ISL sensors [64], development of offline track reconstruction and alignment software and the development of test stand software. The latter is explained in more detail in Appendix C.

The B physics capabilities of CDF are greatly enhanced by the upgraded tracking system. The proper decay length resolution for B hadrons decaying hadronically will be in the order of 15 μm. The extended coverage of SVXII enhances the statistics by a factor of ≈ 1.5 compared to Run I. The lower P_T threshold of 1.5 GeV/c in the muon trigger yields another factor of 2. With an integrated luminosity of 2 fb^{-1}, the goal for Run IIa, the estimated number of fully reconstructed B mesons is approximately 50 times the number achieved in Run I. A planned trigger on $J/\psi \rightarrow e^+ e^-$ would increase this number by another ≈ 50 %.

[2]Analog to Digital Converter.

[3]First In First Out: a shift register where the data entered at the input appear at the output in the same order.

[4] A 'ladder' consists of 3 silicon sensors glued to a carbon fiber support structure and a readout hybrid. Two ladders glued together are a 'module'.

With a factor of 50 increase in the signal events in the various B meson decay modes, the statistical uncertainties of the $B^{\pm}$ and B^0 lifetime measurements would be at the level of 0.5 %. Measurements of the B_S and Λ_B lifetimes in the exclusive decay modes $B_S \to J/\psi\ \phi$ and $\Lambda_B \to J/\psi\ \Lambda$ will be possible with statistical uncertainties below 3 %. In addition to lifetime measurements the B physics program of CDF will include other interesting topics:

- $B_s^0 - \bar{B}_s^0$ mixing will be measured using $B_s^0 \to D_S^-\ \pi^+$ decays. CDF will be sensitive up to $x_s \approx 65$.
- The measurement of $sin(2\beta)$ from $B^0/\bar{B}^0 \to J/\psi\ K_S^0$ decays will be possible with an error of $\pm$ 0.08, comparable to dedicated e^+e^- collider experiments.
- Measurement of CP asymmetry in $B_S^0/\bar{B}_s^0 \to J/\psi\ \phi$.
- Measurement of CP asymmetry related to $sin(2\alpha)$ in $B^0/\bar{B}^0 \to \pi^+\ \pi^-$ decays. Using a special trigger on $\pi^+\ \pi^-$, CDF will be able to collect several 1000 such decays. The estimated uncertainty for a $sin(2\alpha)$ measurement is ≈ 0.1.
- Observation of the rare decays $B^{\pm} \to \mu^+\mu^- K^{\pm}$, $B^0 \to \mu^+\mu^- K^{*0}$, $B_s^0 \to \mu^+\mu^-\ \phi$, $B_d^0(B_s^0) \to \mu^+\mu^-$. For the first two decay channels, visible signals of several 100 events are expected within the Standard Model.

More information on B physics prospects for Run II with the CDF detector can be found in [65] and [71].

Appendix A

Location of Datasets

In the following, the data samples used for this analysis are listed with their locations. Paths in capital letters denote locations in the FATMEN [47] system which allows to access tapes in the STK silo[1].

Run Ia:

Dimuons J/ψ mass region	`/data09/bottom/psix_5p/`
Inclusive electrons	`//FNAL/CDF/B615/PAD01/ELE/`

Run Ib:

Dimuons J/ψ mass region	`/data17/bottom/psia_7b/`
	`/data30/bottom/psia_7b/`
Dimuons $\psi(2S)$ mass region	`/data06/bottom/pspb_7b/`
	`/data30/bottom/pspb_7b/`
Inclusive electrons	`//FNAL/CDF/B/RUN1B/STRB/ELE/ECLB-5B/`

Run Ic:

Dimuons J/ψ mass region	`/data48/bottom/run1c_psia/`
Dimuons $\psi(2S)$ mass region	`//FNAL/CDF/B/RUN1C/STRB/DIMUON/PSPB-6B/`
Inclusive electrons	`//FNAL/CDF/B/RUN1C/STRB/ELE/ECLB-6B/`

[1] The STK silo is a robotic tape storage system.

Appendix B

Monte Carlo Programs

Two types of Monte Carlo (MC) simulations have been used within the CDF Run I Analysis Control [48] offline framework. Full event generators like the PYTHIA program [66] are employed for studies which depend on fragmentation particles resulting from the hadronization of the b-quarks or particles from "underlying" $p\bar{p}$ scattering events. Studies depending only on the production and decay of B hadrons use a Monte Carlo generator that simulates a single B hadron and its decay products. All MC studies done for this analysis use such a simple program, the BGENERATOR. The simulation of a single B meson begins with a model of b-quark production based on next-to-leading oder QCD calculations [67] that used the Martin-Roberts-Stirling MRSD0 parton distribution function [68]. The b-quarks are produced in the rapidity range $|\eta| < 1.3$ with a minimum transverse momentum of 5 GeV/c. (When B meson decays into $J/\psi \rightarrow e^+e^-$ final states are simulated, the minimum b-quark transverse momentum was set to 10 GeV/c.) The b-quarks are then fragmented into B mesons with no additional hadronization products. This is done according to a model using the Peterson fragmentation function [19] with a Peterson parameter of $\epsilon_b = 0.006$. The B mesons are decayed into the various final states using decay kinematics governed by the world average masses and lifetimes of the involved particles. The decay of the B mesons is accomplished using the QQ program [69] developed by the CLEO collaboration. Once Monte Carlo B mesons were generated and decayed into their daughter states, the standard fast simulation of the CDF detector, QFL [70], was invoked. QFL is based on parameterizations and simple models of the detector response determined from data or test beam measurements. A trigger simulation was not used. The MC data generated by QFL was then fed into the same reconstruction procedure as real data.

Appendix C

A Hybrid and Ladder test system for SVXII and ISL

The production and testing of ISL and SVXII devices for the CDF upgrade was performed in several steps at CDF member institutions in the United States, Europe and Japan. The series of events in the production of a SVXII or ISL ladder was as follows:
The silicon sensors were produced by two different companies, Micron Semiconductor in the U.K. and Hamamatsu Photonics in Japan. Some quality tests on the sensors were done directly at these companies. More sophisticated testing procedures were performed at several CDF institutions (see e.g. [64]). The SVX3 readout chips were produced by Honeywell in the United States on wafers which were then tested and diced at the Lawrence Berkely Laboratory (LBL). SVX3 chips which worked properly were then mounted on hybrids. The individual chips, mounted on the hybrids, were tested again for performance and had to pass a 72 hour burnin test. Hybrids passing all tests were then sent to Fermilab where they were tested again on arrival in case of damage caused by shipping. The next step was the assembly of SVXII and ISL ladders of sensors and hybrids. In the case of ISL, three silicon sensors and a readout hybrid were glued to a carbon fibre structure. The silicon strips were then wirebonded sensor to sensor and to the fanout on the hybrid. The complete ladders were checked for functionality and had to pass again a 72 hours burnin test.
The teststand system used at Fermilab to test the hybrids delivered by LBL and to perform the ladder burnin tests consists basically of two types of printed circuit boards and a Personal Computer (PC) running the Linux operating system (Figure C.1). A logic bitstream pattern is downloaded from the PC via a digital I/O[1] card to the MUX/FIFO board and stored in three 8-bit wide FIFO[2] shift registers ("pattern FIFOs") with all inputs receiving TTL compatible logic levels. The speed of the data transfer is limited by the I/O card to $\approx$ 1 MHz. Using an oscillator on the MUX/FIFO board, the FIFO contents is sent out in synchronous

[1]Input / Output
[2]First In First Out: the data read in first are also presented as first at the output.

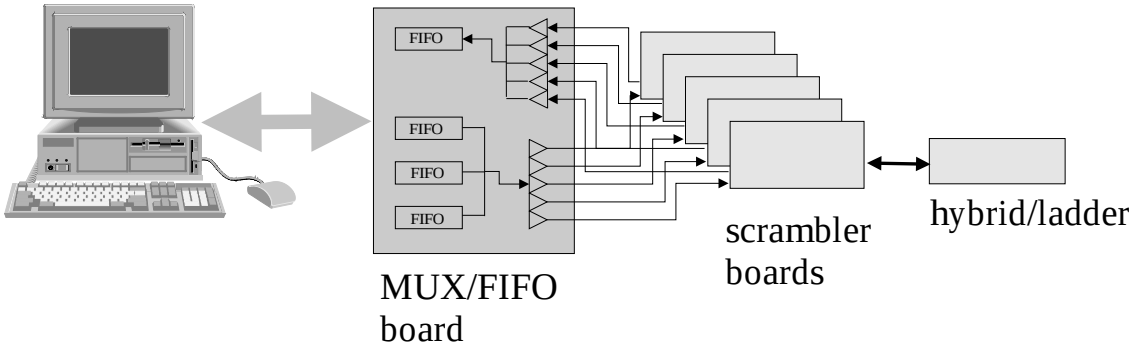

Figure C.1: An overview over the electrical components of the SVXII/ISL burnin test system.

mode to the SVX3 chips on the hybrids. This data transfer to the hybrid occurs at speeds up to 50 MHz. The Scrambler boards provide the necessary interface between the MUX/FIFO boards and the hybrid carrying the SVX3 chips. TTL signals from the MUX/FIFO boards are converted to low voltage differential (LVD) signals required at the inputs of the hybrids. The digital data delivered by the SVX3 chips is converted back to TTL logic levels and read into another FIFO chip (DAQ FIFO) on the MUX/FIFO board which is then read out by the PC. The PC has one or several digital I/O cards and eventually a DAC[3] card connected to the ISA[4] bus, depending on the test to be performed with the system. The burnin system PC has up to 8 I/O cards talking to 8 MUX/FIFO boards. Each MUX/FIFO board can control up to 5 devices (ladders or hybrids) using multiplexer and demultiplexer logic. Another configuration is used for the test of single hybrids and ladders. In this case, the PC has only one I/O card but also a DAC card which can be used to apply a certain calibration voltage to special test inputs of the SVX3 chips. This type of system turned out to be very useful during the hybrid prototyping phase. I proposed this PC-I/O-card solution as a replacement of the much more expensive system favored before. The data was transfered between the MUX/FIFO board and a SGI workstation via the SCSI interface connected to a CAMAC[5] crate carrying a digital I/O-card.

In the following the software written to operate this test system is described. A more detailed description of the printed circuit boards can be found in [72]. To download bitstream patterns and read back the data delivered by the SVX3 chips, I developed a special driver library. The library accesses the I/O and DAC cards directly and provides also functions to control the multiplexers and demultiplexers on the MUX/FIFO boards and the calibration voltage. This library is used for both setups, the burnin system and the second type of test system equipped with one

[3]Digital to Analog Converter
[4]Industry Standard Architecture
[5]Computer Aided Measurement and Control

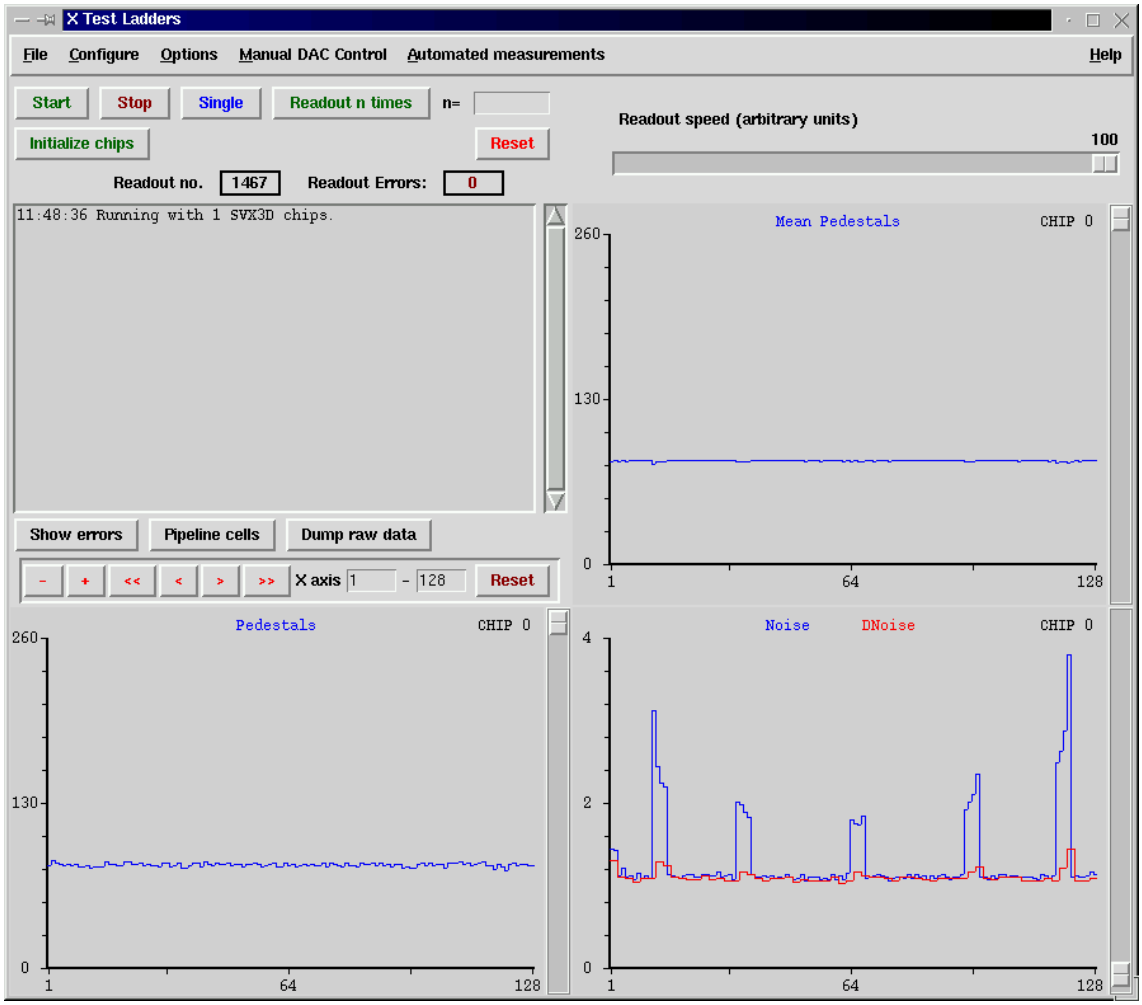

Figure C.2: The XTL main window. Here a test board with one SVX3 chip was connected to the system. Several groups of channels are connected to a capacitor simulating the capacitance load of silicon sensors. These groups of channels are clearly visible in the noise histogram on the bottom right.

I/O and a DAC card.

To perform various tests on single hybrids and ladders, I developed a program providing a graphical user interface (GUI). The XTL[6] program has a main window (Figure C.2) showing pedestals, mean pedestals, noise and differential noise of all readout channels of the SVX3 chips. This allows quick functional tests of hybrids as well as ladders.

Unusually high or low noise is mostly an indication for a problem concerning the silicon sensor. Noise is mainly caused by the capacitive load, dark current and the bias resistors. Channels with unconnected readout strips have therefore much lower noise than expected. A broken aluminium readout strip decreases the capacitance connected to the preamplifier and thus causes lower noise. A short between strips increases the capacitance load and therefore the noise. Another possible reason for

[6]X Test Ladders; the X denotes that the program is running on a X11 graphical system.

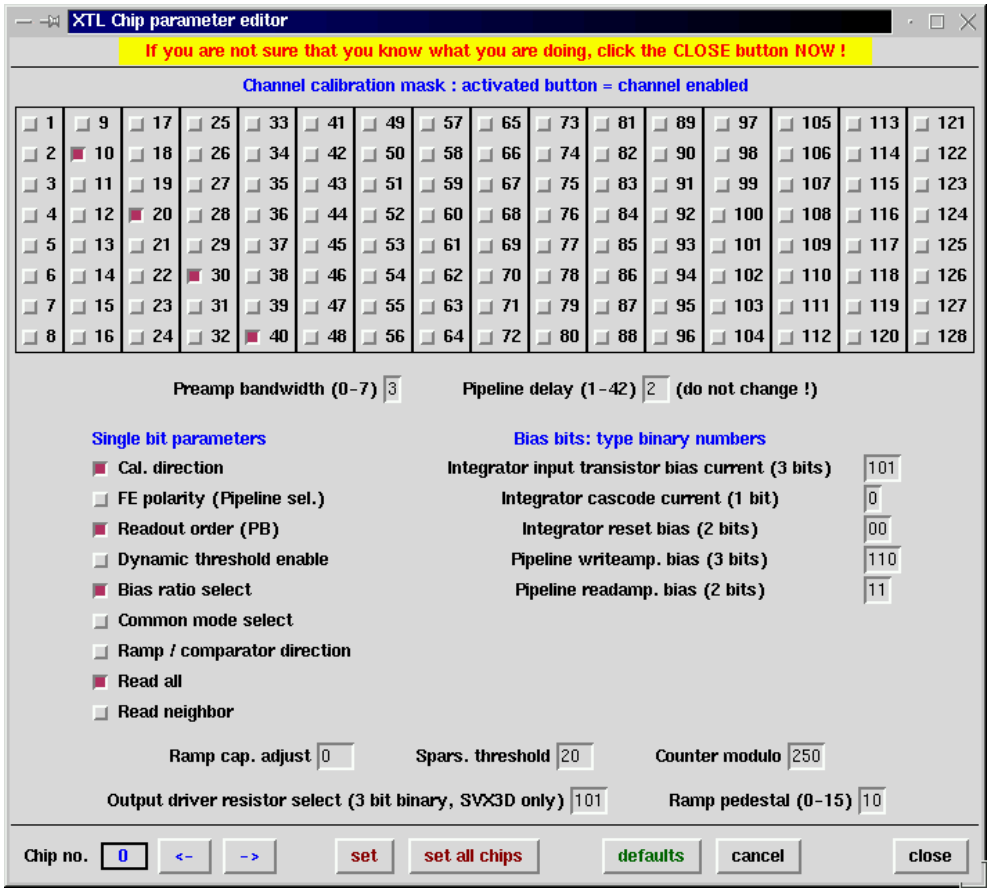

Figure C.3: The XTL chip parameter editor.

high noise is a high leakage current in the sensor. A severe problem is a so-called pinhole. It is a short through the coupling capacitor between the implanted strip and the aluminium readout strip of a silicon sensor. This results in a very high current flowing into the preamplifier of the readout chip which then saturates. The current is high enough to spread to adjacent channels, significantly increasing their noise. Channels with pinhole strips connected can be identified by anomalous pedestal and noise.
The main window of XTL also provides controls to start and stop the data acquisition manually. The readout frequency can be chosen from approximately 0.5 Hz up to 30 Hz.

As mentioned in Chapter 10, the SVX3 readout chips are programmable for different collider running conditions. Several parameters of the chip can be changed, e.g. the front-end polarity and the preamplifier bandwidth. Certain features of the SVX3 chip, such as the sparsification mode, can be switched on or off. XTL provides a chip parameter editor, shown in Figure C.3, to change these parameters individually for each chip of the hybrid or ladder attached to the system.

The SVX3 chips have a test input to inject charge for calibration purposes. This can

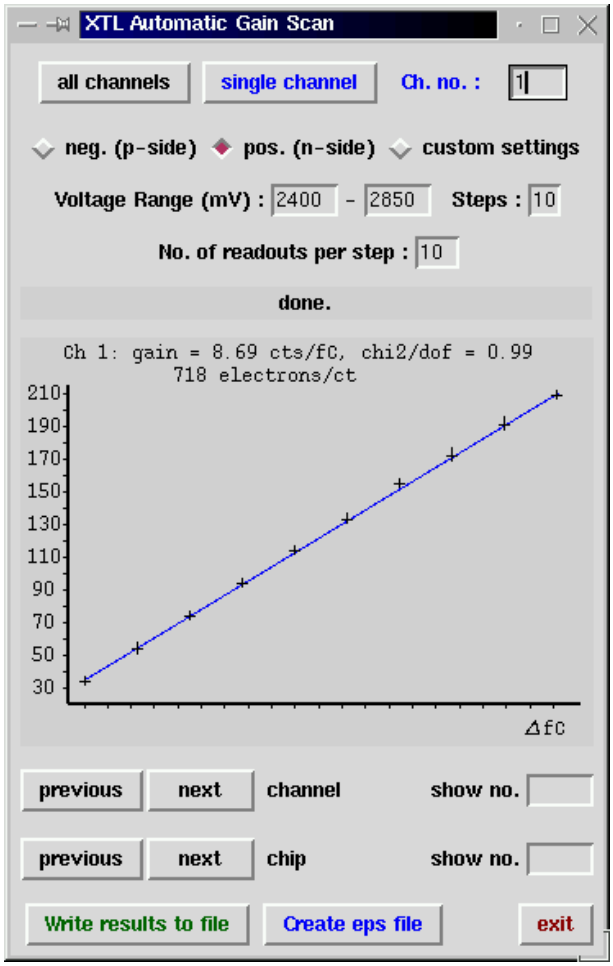

Figure C.4: The control window for automatic gain scans. The test result for one particular channel is displayed.

be done manually by applying a certain voltage to a capacitor on the chip using the DAC card in the PC. Fully automatic gain scans can also be performed with XTL. The control window for the gain measurements is shown in Figure C.4. The gain and the linearity of all channels of the chips on a hybrid are measured by increasing the amount of charge injected into the preamplifiers step by step.
In each particular step, the chips are readout several times. The number of "ADC counts" delivered by the chips is then plotted versus the amount of injected charge. A straight line is fitted to the data points to check the linearity of the channel gain (see Figure C.4). A bad linearity results in a large χ^2/dof of this fit. The result of such a measurement for a whole SVX3 chip is displayed in Figure C.5. Gain and fit χ^2/dof are displayed as a function of the channel number of the particular chip.
Another important quantity to be tested is the signal/noise (S/N) ratio. For this test, an electric charge corresponding to 22000 electrons is injected into the preamplifiers. This number is the expected average charge deposition of a minimum ionizing particle traversing the silicon sensor.
For SVXII and ISL devices, a S/N value between 10 and 15 is expected, depending

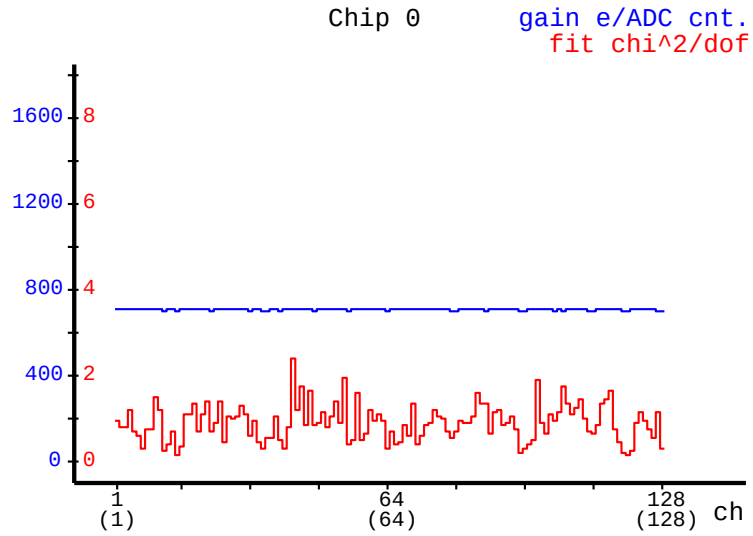

Figure C.5: Gain scan results for one whole chip. Gain and fit χ^2/dof are displayed as a function of the channel number.

on the preamplifier bandwidth setting. Deviations from this value are an indication for possible problems. Figure C.6 shows the control window for signal/noise measurements with the results for one particular chip displayed. Here a problem is indicated by a very low S/N value around channel 40. The average S/N ratio is shown in Figure C.7 for different settings of the preamplifier bandwidth.
Other features of the program include an automated test procedure with noise tests, gain tests and test of the sparsification mode of the chips. A test report is created automatically either in plain text format or HTML[7] to be published on the World Wide Web. This way, test information of hybrids and ladders can be accessed directly using a web browser. The results of noise measurements, gain scans and S/N measurements can also be written to disk in plain text format or as a set of HBOOK histograms to be analyzed offline.
More information on the testing procedure of ISL devices and the identification possible failures can be found in [73].

[7]Hypertext Markup Language

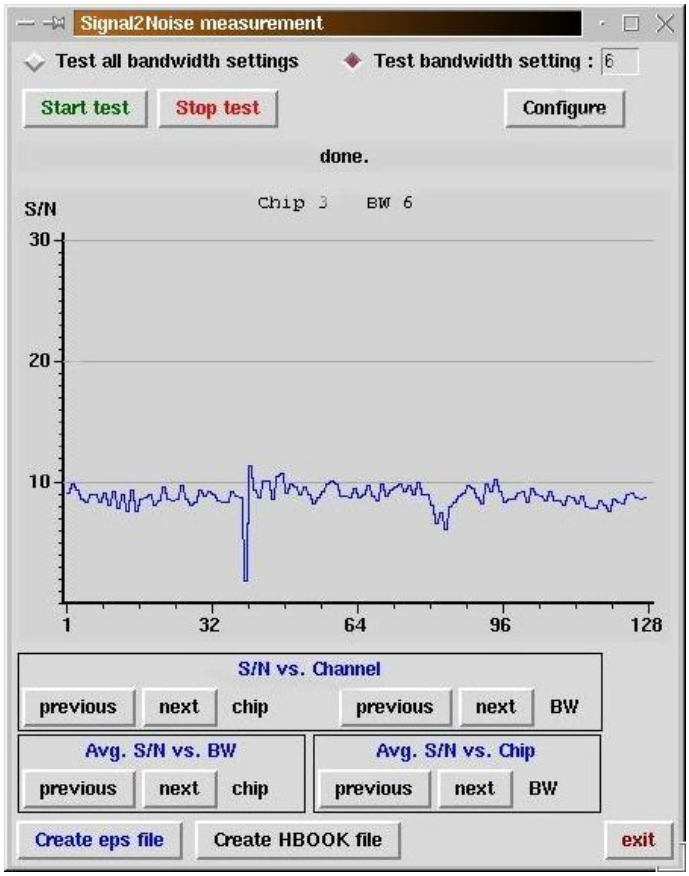

Figure C.6: The control window for signal to noise measurements. The test result for one particular chip is displayed.

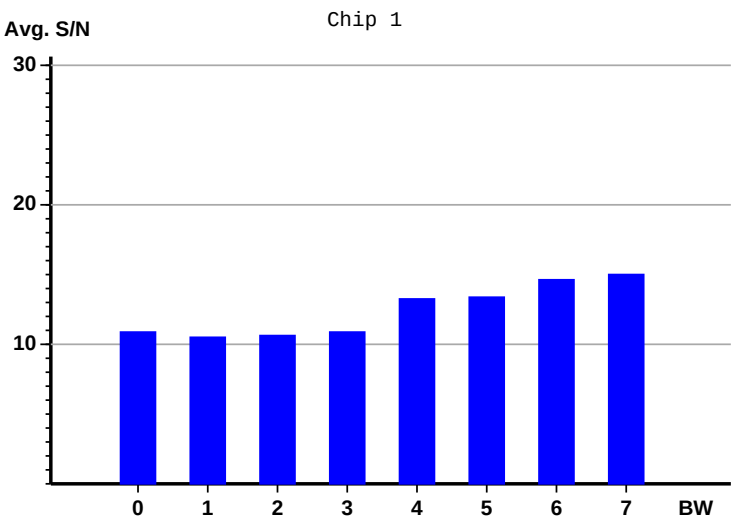

Figure C.7: S/N averaged over all channels of one particular SVX3 chip as a function of the preamplifier bandwidth.

Bibliography

[1] M. Gell-Mann, *The Eightfold Way: A Theory of Strong Interaction Symmetry*, CTSL-20 (1961); *Symmetries of Baryons and Mesons*, Phys. Rev. 125, 1067 (1962).

[2] E.D. Bloom *et. al.*, *High-Energy e^- p Scattering at* $6°$ *and* $10°$., Phys. Rev. Lett. 23, 930 (1969)
M. Breidenbach *et. al*, *Observed Behaviour of Highly Inelastic Electron-Proton Scattering*, Phys. Rev. Lett. 23, 935 (1969).

[3] J.J. Aubert *et. al.*, *Experimental Observation of a Heavy Particle J*, Phys. Rev. Lett. 33, 1404 (1974).

[4] J.E. Augustin *et. al.*, *Discovery of a Narrow Resonance in e^+e^- Annihilation*, Phys. Rev. Lett. 33, 1406 (1974).

[5] J.H. Christenson *et. al.*, *Evidence for the 2 pi Decay of the K_2^0 Meson*, Phys. Rev. Lett. 13, 138 (1964).

[6] S.W. Herb *et. al.*, *Observation of a Dimuon Resonance at 9.5 GeV in 400 GeV Proton-Nucleus Collisions*, Phys. Rev. Lett. 39, 252 (1977).

[7] PLUTO Collaboration, Ch. Berger *et. al.*, Phys. Lett. 76B, 243 (1978); C.W. Darden *et. al.*, Phys. Lett. 76B, 246 (1978).

[8] F. Abe *et. al.*, *Observation of Top Quark Production in $p-\bar{p}$ Collisions with the Collider Detector at Fermilab*, Phys. Rev. Lett. 74, 2626 (1995).

[9] S. Abachi *et. al.*, *Observation of the Top Quark*, Phys. Rev. Lett. 74, 2632 (1995).

[10] M. Kobayashi and T. Maskawa, *CP Violation in the Renormalizable Theory of Weak Interaction*, Prog. Theor. Phys. 49, 652 (1973).

[11] N. Cabibbo, *Unitary Symmetry and Leptonic Decays*, Phys. Rev. Lett. 10, 531 (1963).

[12] L. Wolfenstein, *Parametrization of the Kobayashi-Maskawa Matrix*, Phys. Rev. Lett. 51, 1945 (1983).

[13] H. Wenzel, *Measurement of the Inclusive B-Lifetime Using J/ψ'a at the CDF-Experiment*, Dissertation, RWTH Aachen (1993).

[14] J. Bartels *et al.*, *Review of Particle Physics*, European Physics Journal C15, 1 (2000).

[15] P. Nason, S. Dawson, R.K. Ellis, *The Total Cross Section for the Production of Heavy Quarks in Hadronic Collisions*, Nucl. Phys. B303. 607 (1988)
The One Particle Inclusive Differential Cross Section for Heavy Quark Production in Hadronic Collisions, B327, 49 (1989), *erratum* B335, 260 (1990).

[16] S. Frixione *et al.* in *Heavy Flavours II*, edited by A.J. Buras and M. Lindner, World Scientific, Singapore (1998). Also hep-ph/9702287.

[17] T. Sjöstrand, Int. J. Mod. Phys. A3, 715 (1988).

[18] B. Andersson *et al.*, Z. Phys. C 20, 317 (1983).

[19] C. Peterson, D. Schlatter, I. Schmitt and P. Zerwas *et al.*, *Scaling violations in inclusive e^+e^- annihilation spectra*, Phys. Rev. D27, 105 (1983).

[20] J. Chrin, *Upon the Determination of Heavy Quark Fragmentation Functions in e^+e^- Annihilation*, Z. Phys. C36, 163 (1987).

[21] N. Lockyer *et al.*, *Measurement of the Lifetime of Bottom Hadrons*, Phys. Rev. Lett. 51, 1316 (1983).

[22] E. Fernandez *et al.*, *Lifetime of Particles Containing b Quarks*, Phys. Rev. Lett. 51, 1022 (1983).

[23] C.S. Kim, A.D. Martin, Phys. Lett. B 225, 186 (1989).

[24] I. Bigi, *et al.*, *Non-Leptonic Decays of Beauty Hadrons – From Phenomenology to Theory*, CERN TH 7132/94; published in S. Stone, *B Decays*, 2nd revised edition, 1994, ISBN 981-02-1836-2.

[25] CDF II Collaboration, *Technical Design Report,*
FERMILAB-Pub-96/390-E (1996).

[26] J.D. Cockroft, E.T.S. Walton, *Artificial Production of Fast Protons*, Nature 129, 242 (1932).

[27] M.D. Church, J.P.Marriner, *The Antiproton Sources: Design and Operation*, Ann. Rev. Nucl. Part. Sci. 43, 253 (1993).

[28] A. Ruggiero, *The Fermilab Tevatron I Debuncher Ring*, IEEE Trans. Nucl. Sci. 30, 2478 (1983).

[29] D. Möhl, G. Petrucci, L. Thorndahl, S. van der Meer, *Physics and Techniques of Stochastic Cooling*, Phys. Rep. 58, 73 (1980).

[30] H. Edwards, *The Tevatron Energy Doubler: A Superconducting Accelerator*, Ann. Rev. Nucl. Part. Sci. 35, 605 (1985).

[31] R. Pallmer, A.V. Tollestrup, *Superconduction Magnet Technology for Accelerators*, Ann. Rev. Nucl. Part. Sci. 34, 247 (1984).

[32] CDF Collaboration, F. Abe *et al.*, *The CDF Detector: An Overview*, NIM A271, 387 (1988).

[33] The URL of the CDF Collaboration http://www-cdf.fnal.gov .

[34] H. Mibenura *et al.*, *Construction and Testing of a 3m Diameter × 5m Superconducting Solenoid for the Fermilab Collider Detector Facility (CDF)*, NIM A238, 18 (1985).

[35] D. Amidei *et al.*, *The CDF SVX: A Silicon Vertex Detector for a Hadron Collider*, NIM A289, 388 (1990).

[36] P. Azzi *el al.*, *SVX', The New CDF Silicon Vertex Detector*, NIM A360, 137 (1995).

[37] S. Tkaczyk, *Operational Experience with CDF Microvertex Detectors*, NIM A 368, 179 (1995).

[38] S. Kleinfelder *et al.*, *A Flexible 128 Channel Silicon Strip Detector Instrumentation Integrated Circuit with Sparse Data Readout*, IEEE Trans. Nucl. Sci. 25, 171 (1988).

[39] F. Bedeschi *et al.*, *Design and Construction of the CDF Central Tracking Chamber*, NIM A268, 50 (1988).

[40] Todd A. Keaffaber *et al.*, *CTC Track Reconstruction Efficiency Studies*, CDF internal note no. 4768.

[41] G. Ascoli *et al.*, *CDF Central Muon Detector*, NIM A268, 33 (1988).

[42] J.D. Lewis *et al.*, *The 1992 CDF Muon System Upgrade*, CDF public note no. 2858.

[43] G. Foster *et al.*, *The Fast Hardware Track–Finder for the CDF Central Tracking Chamber*, NIM A269, 93 (1988).

[44] J. Carroll *et al.*, *The CDF Level 3 Trigger*, NIM A300, 552 (1991)

[45] D. Cronin-Hennessy *et al.*, *Luminosity at CDF*, CDF internal note no. 4956.

[46] D. Quarrie & B. Troemel, *YBOS Programmer's Reference Manual*, CDF public note no. 156 (1987).

[47] CERN Application Software Group, *FATMEN – File and Tape Management System*, http://wwwinfo.cern.ch/asdoc/fatmen_html3/fatmain.html

[48] E. Sexton–Kennedy *et al.*, *A Beginners Guide To Analysis Control and Build Job*, CDF public note no. 384 (1996).

[49] J.P. Marriner, *Secondary vertex fit with (optional) Mass Constraints and (optional) Pointing Contraints*, CDF public note 1996 (1993).

[50] T. Affolder *et al.*, *Measurement of b-Quark Fragmentation Fractions in $p\bar{p}$ Collisions at $\sqrt{s}$ = 1.8 TeV*, Phys. Rev. Lett. 84, 1663 (2000).

[51] H. Wenzel *Fitting the beam position with the SVX*, CDF internal note no. 1924 (1993).

[52] H. Wenzel, *The Primary Interaction Vertex*, CDF internal note no. 4066 (1997).

[53] V. Blobel, E. Lohrmann, *Statistische und numerische Methoden der Datenanalyse*, Teubner Verlag 1998, ISBN 3-519-03243-0

[54] S. Brandt, *Datenanalyse*, BI Wissenschaftsverlag, ISBN 3-411-01591-8

[55] CERN program library
CERN program library short writeups, CERN 1996

[56] ROOT is a data analysis system developed by René Brun *et al.*.
Further information is available from http://root.cern.ch

[57] CERN Application software group,
MINUIT Function Minimization and Error Analysis, CERN, D506 (1998).

[58] William C. Wester, *A Measurement of the Mass of the B_s^0 Meson in Proton–Antiproton Collisions at $\sqrt{s} = 1.8$ TeV*, PhD thesis, Department of Physics, University of California, Berkeley, 1994.

[59] F. Abe *et al.*, *Measurement of B Hadron Lifetimes Using J/ψ Final States at CDF*, Phys. Rev. D57, 5382 (1998).

[60] The URL of the CERN B lifetimes working group http://claires.home.cern.ch/claires/lepblife.html .

[61] F. Hartmann *et al.*, *The CDF Intermediate Silicon Layers Detector*, CDF public note no. 4796 (1998).

[62] Maurice Garcia-Sciveres, *The SVX3D Integrated Circuit*, NIM A435.

[63] The CDFII collaboration, *Proposal for the Enhancement of the CDF II Detector: An Inner Silicon Layer and a Time of Flight Detector*, FERMILAB-Proposal 909 (1998).

[64] F. Hartmann, *Entwicklungsarbeit am Spurdetektor für das CDF Experiment am Tevatron*, Dissertation, Universität Karlsruhe (2000).

[65] The CDF Collaboration, *Summary of B Physics Prospects with the CDF II Detector*, CDF internal note no. 5045 (1999).

[66] H.-U. Bengtsson, T. Sjöstrand, *PYTHIA 5.7 and JETSET 7.4: Physics and Manual*, Computer Physics Commun. 46, 43 (1987).

[67] P. Nason, S. Dawson and R.K. Ellis, *The Total Cross Section for the Production of Heavy Quarks in Hadronic Collisions*, Nucl. Phys B303, 607 (1988). *The One Particle Inclusive Differential Cross Section for Heavy Quark Production in Hadronic Collisions*, B335, 260 (1990).

[68] A.D. Martin, W.J. Stirling and R.G. Roberts, *New Information on Parton Distributions*, Phys. Rev. D47, 867 (1993).

[69] P. Avery *et al.*, Cornell internal note CSN-212 (1985, unpublished).

[70] M. Shapiro *et al.*, *A user's guide to QFL*, CDF punlic note no. 1810 (1992).

[71] R. Blair *et al.* (CDF Collaboration), *The CDF II Detector: Technical Design Report*, Fermilab-Pub-96/390-E (1996).

[72] E. Bartz, R. Cropp, A. Heiss, T. Munar and J. Valls, *Operation of a Burn-in Setup for SVXII/ISL Ladders*, CDF public note no. 4586 (1999).

[73] Anthony Affolder *et al.*, *Production Testing of ISL modules at FNAL*, CDF public note no. 5180 (2000).

Acknowledgments

I thank Prof. Dr. Thomas Müller for giving me the opportunity to stay in the U.S. for 1 1/2 years and to work at Fermilab with the ISL hardware group for the CDF detector upgrade. I also thank him for giving me the freedom to choose the topic of my thesis and for his support for presenting the results of this work.

I thank Prof. Dr. Michael Feindt for useful discussions and for being "Korreferent".

I thank Dr. Hans Wenzel for introducing me to Fermilab, the CDF experiment and B physics as well as for many useful hints and for reading the manuscript.

I thank Dr. Frank Hartmann for introducing me to silicon detector technology as well as for reading the manuscript.

I thank the members of the CDF-II ISL and SVXII hardware groups for the good working atmosphere at "Lab D".

I thank Dr. Andrew Scott, Chris Hill, Dr. Robert Cropp and Dr. James P. Done for interesting discussions about physics, sports and other important topics.

I thank all members of the IEKP groups at the University and the "Forschungszentrum" for the friendly and relaxed working atmosphere. Special thanks go to Dr. Armin Köngeter, Dr. Ulrich Schwickerath, Patrick Schemitz and Thomas Allmendinger for managing the computer cluster.

During the time of my graduate studies, I was financially supported by the Graduiertenkolleg "Elementarteilchenphysik an Beschleunigern" of the faculty of physics and by the Institut für Experimentelle Teilchenphysik.

Finally, I thank my parents for their support during my studies. I thank especially my mother for her support and her trust in me during the time it took to finish this work.